Characterization of Electrostatic Potential and Trapped Charge in Semiconductor Nanostructures using Off-Axis Electron Holography

by

Zhaofeng Gan

A Dissertation Presented in Partial Fulfillment
of the Requirements for the Degree
Doctor of Philosophy

Approved April 2015 by the
Graduate Supervisory Committee:

Martha R. McCartney, Co-Chair
David J. Smith, Co-Chair
Jeffery Drucker
Peter A. Bennett

ARIZONA STATE UNIVERSITY

May 2015

ABSTRACT

Off-axis electron holography (EH) has been used to characterize electrostatic potential, active dopant concentrations and charge distribution in semiconductor nanostructures, including ZnO nanowires (NWs) and thin films, ZnTe thin films, Si NWs with axial *p*-*n* junctions, Si-Ge axial heterojunction NWs, and Ge/Li_xGe core/shell NW.

The mean inner potential (MIP) and inelastic mean free path (IMFP) of ZnO NWs have been measured to be 15.3V±0.2V and 55±3nm, respectively, for 200keV electrons. These values were then used to characterize the thickness of a ZnO nano-sheet and gave consistent values. The MIP and IMFP for ZnTe thin films were measured to be 13.7±0.6V and 46±2nm, respectively, for 200keV electrons. A thin film expected to have a *p*-*n* junction was studied, but no signal due to the junction was observed. The importance of dynamical effects was systematically studied using Bloch wave simulations.

The built-in potentials in Si NWs across the doped *p*-*n* junction and the Schottky junction due to Au catalyst were measured to be 1.0±0.3V and 0.5±0.3V, respectively. Simulations indicated that the dopant concentrations were ~$10^{19}cm^{-3}$ for donors and ~10^{17} cm^{-3} for acceptors. The effects of positively charged Au catalyst, a possible n^+-n^--*p* junction transition region and possible surface charge, were also systematically studied using simulations.

Si-Ge heterojunction NWs were studied. Dopant concentrations were extracted by atom probe tomography. The built-in potential offset was measured to be 0.4±0.2V, with the Ge side lower. Comparisons with simulations indicated that Ga present in the Si region was only partially activated. *In situ* EH biasing experiments combined with simulations

indicated the B dopant in Ge was mostly activated but not the P dopant in Si. *I-V* characteristic curves were measured and explained using simulations.

The Ge/Li_xGe core/shell structure was studied during lithiation. The MIP for Li_xGe decreased with time due to increased Li content. A model was proposed to explain the lower measured Ge potential, and the trapped electron density in Ge core was calculated to be 3×10^{18} electrons/cm^3. The Li amount during lithiation was also calculated using MIP and volume ratio, indicating that it was lower than the fully lithiated phase.

DEDICATION

To my parents

ACKNOWLEDGMENTS

First of all, I would like to express my deepest gratitude to my supervisors, Professor Martha R. McCartney and Regents' Professor David J. Smith, for their support, guidance and encouragement that made everything I achieved possible during my PhD study. Their enthusiasm, meticulous attitudes, precise insight and great patience in doing research and teaching students have deeply impressed me and educated me as good characteristics for my future career.

I would like to thank Professors Jeff Drucker and Peter Bennett for helpful suggestions and for serving on my dissertation committee. I am grateful for the use of facilities in the John M. Cowley Center for High Resolution Electron Microscopy. Special thanks to Karl Weiss, Dr. Zhenquan Liu and Dr. Toshihiro Aoki for their technical support and assistance throughout my research. The financial support from US Department of Energy (Grand No. DE-FG02-04ER46168) is gratefully acknowledged.

I also would like to express my deep appreciation to Dr. S. Tom Picraux, Dr. Jinkyoung Yoo of Los Alamos National Lab, Dr. Daniel E. Perea, Dr. Chongmin Wang of Pacific Northwest National Lab, and Professor Hongbin Yu, Yonghang Zhang of Arizona State University for their collaboration and for providing the samples characterized in this dissertation.

Particular thanks to our research group members- Dr. Lin Zhou, Dr. Kai He, Dr. Luying Li, Dr. Wenfeng Zhao, Dr. Lu Ouyang, Dr. Jaejin Kim, Dr. Michael Johnson, Dr. Dinghao Tang, Dr. Sahar Farjami, Sahar Hihath, Allison Boley, Ajit Dhamdhere, Jing Lu, Sirong Lu, Thomas McConkie, Xiaomeng Shen, Brian Tracy, Majid Vaghayenegar, HsinWei Wu, Desai Zhang, and *et al*, for their friendship and support.

Last but not least, I am most grateful to my family for their love and support.

TABLE OF CONTENTS

Page

LIST OF TABLES ix

LIST OF FIGURES x

CHAPTER

1 INTRODUCTION 1

1.1 Background 1

1.2 Charge Distribution and Band Alignment in Semiconductors 5

1.2.1 *p-n* Junction 5

1.2.2 Metal Semiconductor Contact 9

1.2.3 Heterojunction 13

1.3 Growth of Semiconductor Nanostructures 16

1.3.1 Epitaxial Growth Techniques 16

1.3.2 Nanowire Growth 17

1.4 Outline of Dissertation 19

References 22

2 EXPERIMENTAL DETAILS 25

2.1 Off-Axis Electron Holography 25

2.1.1 Introduction 25

2.1.2 Theory and Hologram Reconstruction 26

2.1.3 Mean Inner Potential 33

2.1.4 Experimental Setup 35

2.2 Scanning Transmission Electron Microscopy 39

CHAPTER Page

2.3 Electron-Energy-Loss Spectroscopy 41

2.4 Sample Preparation 42

References 45

3 MEAN INNER POTENTIAL AND INELASTIC MEAN FREE PATH OF ZnO AND ZnTe 47

3.1 MIP and IMFP of ZnO NWs 47

3.1.1 Introduction 47

3.1.2 Experimental Details and Results 49

3.1.3 Conclusions 56

3.2 MIP and IMFP measurement of ZnTe 57

3.2.1 Introduction 57

3.2.2 Experimental Details and Results 58

3.2.3 Simulation of Dynamical Effects 65

3.2.4 Conclusions 69

References 71

4 MAPPING ELECTROSTATIC PROFILES ACROSS AXIAL *p-n* JUNCTIONS IN Si NANOWIRES USING OFF-AXIS ELECTRON HOLOGRAPHY 74

4.1 Introduction 74

4.2 Experimental Details 76

4.3 Results and Discussions 78

4.4 Conclusions 88

References 89

CHAPTER Page

5 MEASUREMENT OF ACTIVE DOPANTS IN AXIAL Si-Ge NANOWIRE HETEROJUNCTIONS USING OFF-AXIS ELECTRON HOLOGRAPHY AND ATOM-PROBE TOMOGRAPHY 91

5.1 Introduction 91

5.2 Experimental Details 92

5.3 Results and Discussions 95

5.4 Conclusions 115

References 117

6 CHARACTERIZATION OF TRAPPED CHARGES IN Ge/Li_xGe CORE/SHELL STRUCTURE DURING LITHIATION USING OFF-AXIS ELECTRON HOLOGRAPHY 119

6.1 Introduction 119

6.2 Experimental Details 121

6.3 Results and Discussions 122

6.4 Conclusions 130

References 131

7 SUMMARY AND FUTURE WORK 133

7.1 Summary 133

7.2 Remarks on Possible Future Work 136

References 139

LIST OF REFERENCES 140

LIST OF TABLES

Table Page

1.1 Properties of Si and Ge [2]..... 3

1.2 Work Functions of Common Metal Contacts 10

3.1 Measurement of Mean Inner Potential and Inelastic Mean Free Path of ZnO NWs..... 53

3.2 Linear Fitting Results from Figure 3.10 61

3.3 Dynamical Effects for ZnTe near [001] Zone Axis with Different Thicknesses 66

3.4 Measurement of Dynamical Effects for Different Materials at [011] Zone Axis 69

6.1 Measured Potential of the Li_xGe Shell 126

6.2 Measured Radius for NW Core and Whole NW..... 129

LIST OF FIGURES

Figure Page

1.1 Schematic of Electron Energy Band Structure for Intrinsic Semiconductor 1

1.2 Schematic Diagram of Si Bonding: (a) Intrinsic Si with No Dopant. (b) *n*-type Doped Si (with Phosphorus). (c) *p*-type Doped Si (with Boron) [2] 2

1.3 Schematic Diagram of a *p*-*n* Junction: (a) Energy Band Diagrams of *p*-type and *n*-type Semiconductors. (b) Energy Band Diagram of a *p*-*n* Junction in Thermal Equilibrium. (c) Depletion Region of a *p*-*n* Junction [26] 7

1.4 Schematic Diagram of a *p*-*n* Junction under Different Bias Conditions: (a) Energy Band Diagram of the *p*-*n* Junction with No Bias. (b) Energy Band Diagram of the *p*-*n* Junction with Forward Bias. (c) Energy Band Diagram of the *p*-*n* Junction with Reverse Bias [26] 7

1.5 Schematic Diagram of a Schottky Contact: (a) Energy Band Diagram of Metal and *p*-type Semiconductor Before Contact. (b) Energy Band Diagram of Schottky Contact. ϕ_m is Work Function for Metal, ϕ_s and χ are Work Function and Electron Affinity, Respectively, for Semiconductor [26] 10

1.6 Schematic Diagram of a Metal-Semiconductor Ohmic Contact: (a) Band Structure of Metal and Semiconductor Before Contact. (b) Band Structure of Metal-Semiconductor Ohmic Contact at Thermal Equilibrium. (c) Band Structure of Metal-Semiconductor Ohmic Contact with Positive Bias on Metal. (d) Band Structure of Metal-Semiconductor Ohmic Contact with Negative Bias on Metal [25] 12

Figure Page

1.7 Schematic Energy Band Structure Diagram of Metal and Heavy Doped *n*-type Semiconductor [25] 13

1.8 Energy Band Gaps and Lattice Constants for Si, Ge and Several III-V Compound Semiconductors [2] 14

1.9 Schematic Energy Band Diagrams for Different Types of Heterojunctions [25] ... .14

1.10 Schematic Energy Band Diagram for Heterojunction Before and After Contact [26] 16

1.11 Schematic Diagram of VLS NW Growth [39] 19

2.1 Schematic Diagram Showing the TEM Components Essential for the Technique of Off-Axis Electron Holography [9] 27

2.2 Schematic Diagram Illustrating the Procedure for Hologram Reconstruction: (a) A Hanning Window Is Applied to the Hologram to Smoothen the Edges; (b) Fourier Transform of the Hologram; (c) Extract One of the Side Bands; (d) Inverse Fourier Transform of Side Band Allows Extraction of Amplitude and Phase Images 29

2.3 Schematic Illustration of the Off-Axis Electron Holography Setup Using the Philips-FEI CM200 [7] 36

2.4 Schematic Diagram Showing the Round Beam (Left) and Stigmated Beam (Right). The Orange Part Is the Most Coherent Region of the Beam 36

Figure Page

2.5 Contrast Measurements in HRTEM Mode (Left), and Lorentz Mode (Right), with Different Magnifications and Biprism Voltages. The Electron-Beam Energy Was 200keV and the Hologram Exposure Time Was 1 Second 38

2.6 Schematic Diagram Showing the Microscope Geometry, Signals and Detectors for Scanning Transmission Electron Microscopy [28] 39

2.7. Schematic Diagrams Showing the Orientation of the Sample Relative to the Polishing Glass Stub (Left), and the Desired Geometry of the Sample (Right) 43

3.1 Schematic Diagram of ZnO Wurtzite Structure, where the Arrow Indicates the [0001] Direction [1] 47

3.2 Schematic Diagram of Typical ZnO Nanostructures [1] 48

3.3 TEM Images of ZnO NWs: (a) Low-Magnification TEM Image of ZnO NW, where a Transition in NW Diameter Is Arrowed; (b) Enlargement Showing the Transition Region; (c) TEM Image Showing the End of a ZnO NW; (d) TEM Image of ZnO NW Showing the Effects of Radiation Damage Due to the Incident Electron Beam 50

3.4 Holography Study of ZnO NW: (a) Hologram of ZnO NW; (b) Reconstructed Phase Image of ZnO NW; (c) Reconstructed Thickness Image of ZnO NW, Using IMFP of 85nm (for Si); (d) Line Profile of Phase along the Blue Arrow in (b) (Black Dots) and Fitting Result Using Cylindrical Model (Red Line); (e) Thickness Profile along the Blue Arrow in (c) 51

3.5 (a) MIP vs. Thickness, and (b) IMFP vs. Thickness, for ZnO NWs 53

Figure Page

3.6 Holography of ZnO Nano-Sheet: (a) TEM Image; (b) Hologram of ZnO Nano-Sheet; (c) Reconstructed Phase Image of ZnO Nano-Sheet; (d) Thickness Profile with Error Bars Measured Using MIP (Blue), and IMFP (Red), Respectively, along the Blue Arrow in (c) 54

3.7 Schematic Diagram of Zincblende Structure ZnTe 57

3.8 Holography of Intrinsic ZnTe Thin Film: (a) Hologram of ZnTe Thin Film; (b) Reconstructed Phase Image of ZnTe Thin Film, with Blue Arrow Showing the Position Used for Recording CBED Pattern; (c) Phase Profile Extracted along the White Arrow in (b); (d) Thickness Profile Extracted from Processed Thickness Image at the Same Positions as the White Arrow in (b), Calculated Here Using the IMFP of 85nm for Si 59

3.9 CBED Patterns for ZnTe: (a) Experimental CBED Pattern; (b) Simulated CBED Pattern for Thickness of 110nm; (c) Simulated CBED Pattern for Thickness of 120nm; (d) Simulated CBED Pattern for Thickness of 100nm 60

3.10 Phase at CBED Positions as a Function of the ZnTe Thickness as Estimated from the CBED Pattern 61

3.11 IMFP of ZnTe: (a) IMFP Shown as a Function of CBED Thickness; (b) Frequency Count of Measured IMFPs 63

3.12 Holography of Al-Doped ZnTe Thin Film with Supposed *pn* Junction: (a) TEM Image of ZnTe Thin Film on GaSb Substrate; (b) Hologram of ZnTe Thin Film; (c) Reconstructed Phase Image of ZnTe; (d) and (e) Phase and Thickness Profiles, Respectively, along Blue Arrow in (c) 64

Figure Page

3.13 Simulation of Dynamical Effects at Different ZnTe Thicknesses. The Electron Beam Energy Is 200keV, the Zone Axis Is [001], the Tilting Direction Is Shown by the Red Arrow, and the Phase Scale Bar in the Unit of Radian Is Shown on the Right. (a) 50nm; (b) 100nm; (c) 150nm 66

3.14 Simulation of Dynamical Effects for ZnTe at Different Zone Axes. The Electron Beam Energy Is 200keV, the Thickness Is 100nm, the Tilting Directions Are Shown by Red Arrows and the Color Scale Bar in the Unit of Radian Is Shown on the Right. (a) [001]; (b) [011]; (c) [111] 68

3.15 Simulation of Dynamical Effects in Different Materials. The Electron Beam Energy Is 200keV, the Thickness Is 100nm, the Zone Axis Is [011], the Tilting Direction Is Shown by the Red Arrow and the Color Scale Bar in the Units of Radians Is Shown on the Right. (a) Si; (b) GaAs; (c) ZnTe 68

4.1 Schematic Diagram of the Si NW Growth Procedure: (a) Au Particles Were Deposited on Si Substrate as Catalysts; (b) *n*-type Si Segment Was Grown using P as Dopant; (c) P Source Was Switched Off and a *p*-type Si Segment was Grown Due to Unintentional Dopant 76

4.2 Electron Micrographs Showing the Morphology of a Typical Si NW, with *p*-*n* Junction Location Estimated to Be ~300nm from Top End of the NW 78

4.3 (a) Hologram of Doped Si NW Supported on Holey Carbon Film; (b) Reconstructed Phase Image Visualized with Pseudo-color; (c) Phase Profile along Blue Arrow in (b); (d) Phase Profile Across Width of NW along the Red Arrow in (b) and Fitting Result (Red Line) Using Cylindrical NW Model 79

Figure Page

4.4 Thickness Profile along White Arrow in Figure 4.3b Showing the NW Has a Constant Projected Thickness of ~60nm 80

4.5 (a) Vacuum-subtracted Phase Line Profile along White Arrow in Figure 4.3b; (b) Built-in Potential Before and After Application of Gaussian Filter 81

4.6 (a) Schematic Showing Cross Section of Model Used for Simulations Consisting of Si NW with *p*-*n* Junction, Grounded on the *n*-side and Biased on the Au Particle at the End of the *p*-doped Region; (b) Experimental Built-in Potential Profile and Simulated Profiles for Different Dopant Concentrations at *p*-*n* Junction, Work Function ϕ =4.6 V; (c) Simulated Built-in Potential Profiles with Different Gradient Widths, Dopant Concentrations $N_A=10^{17}$ cm^{-3}, $N_D=10^{19}$ cm^{-3}, and Work Function ϕ =4.6 V. Two Layers in the Dopant Concentrations of $N_D=10^{18}$ cm^{-3} and $N_D=10^{17}$ cm^{-3}, Respectively, Are Added after *n*-type Region with Layer Widths as Shown in the Legend 83

4.7 (a) Simulated Built-in Potential Profiles with Different Surface Charges and Experimental Potential Profile, Dopant Concentrations $N_A=10^{17}$ cm^{-3}, $N_D=10^{19}$ cm^{-3}, Work Function ϕ =4.6V; (b) Simulated Built-in Potential Profiles with Different Bias on a Single Schottky Diode, Dopant Concentrations $N_A=10^{17}$ cm^{-3}, Work Function ϕ =5V 86

Figure Page

5.1 Schematic Diagram of the Axial Si-Ge NW Growth Procedure: (a) Au Particles Were Deposited on Si Substrate as Catalysts; (b) *p*-type Ge Segment Was Grown Using B as Dopant; (c) Ga Was Added to Catalyst, Forming AuGa Alloy, and *i*-type Ge Segment Was Grown; (d) *n*-type Si Segment Was Grown Using P as Dopant 93

5.2 STEM HAADF Images of Axial Si-Ge NW (a) and (c), and EDX Profiles Across Si-Ge Heterojunction (b) and Si-catalyst Interface (d) 96

5.3 (a) TEM Image Showing the Morphology of a Typical Si-Ge Heterojunction NW; (b) STEM HAADF Image Showing the Morphology of a Different Si-Ge Heterojunction NW Grown from the Same Growth Substrate 97

5.4 EELS Mapping of Axial Si-Ge NW: (a) and (b) STEM HAADF Images; (c) EELS Mapping of Si (Red) and Ge (Green) at Si-Ge Interface 98

5.5 Geometric Phase Analysis of Axial Si-Ge NW: (a) STEM HAADF Image, with the Diffraction Spots Chosen for Analysis Arrowed in the Inserted Diffractogram; (b) Calculated Out-of-plane Strain E_{xx} Mapping; (c) E_{xx} Strain Profile Extracted along White Arrow in (b) 99

5.6 (a) and (b) Typical Holograms of Si-Ge NW Heterojunction; (c) and (d) Reconstructed Phase Images from Holograms in (a) and (b), Respectively 100

5.7 (a) Phase and Width Line Profiles Extracted from along White Arrows in Figure 5.6c and 5.6d and Combining Results; (b) Potential Profile Calculated Using Phase Line Profile and Width Line Profile after Fitting (Blue) in (a) 102

Figure Page

5.8 (a) TEM Image Showing the Si-Ge Heterojunction NW after *In Situ* Mounting to Biasing Holder. (b) Typical Hologram of the Si-Ge Heterojunction NW with +4V Bias on Si Side. (c) Reconstructed Phase Image from (b) 104

5.9 (a) Phase Line Profiles Extracted from along White Arrow in Figure 5.8c under Different Biasing Conditions and Potential Profiles Calculated from Phase Line Profiles Using a Constant Width of 61nm. (b) *IV* Characteristic Curve from Measurement 106

5.10 B, P and Ga Dopant Profiles, and Si, Ge Compositions of a Typical Si-Ge Heterojunction NW Measured Using APT 107

5.11 (a) Simulated Built-in Potential Line Profiles Using Different Fractions of Active Ga, Fully Activated B and P from Figure 5.10, Where Legend Shows the Amount of Active Ga; (b) Simulated Built-in Potential Line Profiles Using Different Fractions of Active B and P, but Without Ga from Figure 5.10, Where Legend Shows the Amount of Active B and P 108

5.12 Simulated Band Structure Using 100% Activated B and 10% P, but Without Ga from Figure 5.10 112

5.13 (a) Simulated Built-in Potential Line Profiles under Different Bias Conditions, Using 10% Activated B and 100% P, but Without Ga from Figure 5.10; (b) Simulated Built-in Potential Line Profiles under Different Bias Conditions, Using 100% Activated B and 10% P, but Without Ga from Figure 5.10 114

6.1 Schematic Diagram of Setup Used for *In Situ* Observations of the Ge NW Lithiation Process 121

Figure Page

6.2 TEM Images of Ge NW During Lithiation Process: (a) Before Lithiation; (b) Formation of Ge/Li_xGe Core/Shell Structure; (c) the Shell Part Grew While the Core Part Shrank; (d) At the End of Lithiation, Where Polycrystalline Li_xGe Has Been Formed 122

6.3 EELS Mapping of Ge/Li_xGe Core/Shell Structure: (a) STEM HAADF Image; (b) EELS Spectrum Showing the Presence of Li; (c) Li Mapping of Core/Shell Structure 123

6.4 Electron Holography Observations of Ge/Li_xGe Core/Shell NW During Lithiation: (a), (d) and (g) Holograms of NW; (b), (e) and (h) Corresponding Reconstructed Phase Images, Shown in Pseudo-color (Scale Bar Shown at Top Right in Units of Radian); (c), (f) and (i) Phase Profiles along the White Arrows in (b), (e) and (h), Respectively 124

6.5 Model for Trapped Charges in Ge/Li_xGe Core/Shell Structure: (a) Schematic Diagram of the Model; (b) Experimental Data (Black) and Best Fitted Results (Red) 127

6.6 Simulation of Potential Distribution in Ge/Li_xGe Core/Shell NW: (a) Potential Distribution in NW Cross Section, Shown in Pseudo-color with Scale Bar on the Right in Units of V; (b) Potential Profile along Y=0 in (a) 128

7.1 Tomography of Si-Ge NWs: (a) HAADF Image at 0˚ Tilt; (b) Tomography Reconstruction Result Shown in Pseudo-color; (c) Cross Section of NW 138

CHAPTER 1

INTRODUCTION

1.1 Background

Materials in the solid state can be classified into three types, namely insulator, semiconductor and conductor, based on their electrical conductivity. Materials with conductivity in the range of 10^{-8} siemens per centimeter to 10^{3} siemens per centimeter are usually defined as semiconductors, and their conductivity is sensitive to temperature, photon luminance, magnetic field and dopant atoms. Semiconductor materials are often crystalline and due to their periodic potential field, the electron energy band structure becomes discontinuous and forms forbidden bands. A schematic for the energy band structure of a semiconductor is shown in Figure 1.1, where the valence band is filled with electrons, the conduction band is empty and the electron Fermi level is at the middle of the forbidden band. The band-gap gap (E_g) is defined as the energy difference between the highest point of the valence band and the lowest point of the conduction band, which is usually less than ~2eV [1].

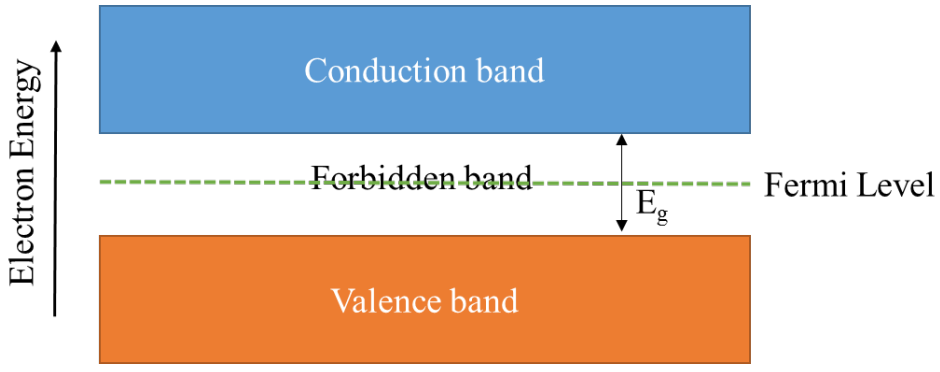

Figure 1.1 Schematic of electron energy band structure for intrinsic semiconductor.

When the temperature is higher than 0K or there is photon luminance, some of the electrons are excited from the valence band to the conduction band. Thus, electrons in the conduction band or empty states in the valence band (holes) can move under the influence of an external electric field and the material becomes conductive. However, the number of excited electrons is usually relatively small at room temperature and the conductivity is still low compared to conductors such as metals.

The conductivity of a semiconductor can be changed by doping with different types and concentrations of impurities, which are called dopants. For *n*-type doping, electrons are not fully bonded and the ionized atom is positively charged. For *p*-type doping, electrons are missing and the ionized atom is negatively charged. Figure 1.2 shows the schematic bonding diagram for intrinsic silicon, *n*-type doped silicon and *p*-type doped silicon. These dopants shift the position of the Fermi level in the band structure and thus the conductivity. Doping can also result in an electric field where the charge carriers are depleted and only ionized impurity atoms are left behind and act as charge barriers. These properties are discussed in more detail in later sections [2].

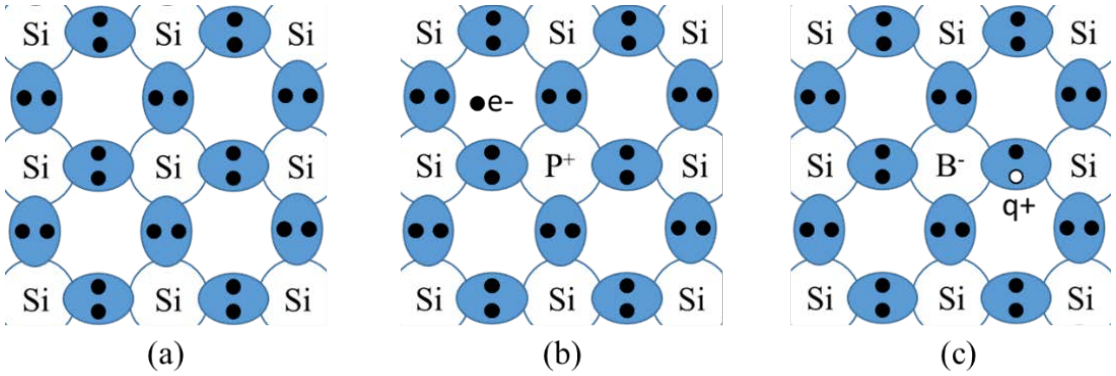

Figure 1.2 Schematic diagram of Si bonding: (a) Intrinsic Si with no dopant. (b) *n*-type doped Si (with phosphorus). (c) *p*-type doped Si (with boron) [2].

Si and Ge are two of the most important semiconductor materials and they have been widely investigated because of their abundance. The most important properties for Si and Ge are summarized in the following table:

Table 1.1 Properties of Si and Ge [2].

Properties	Ge	Si
Crystal Structure	Diamond Cubic	Diamond Cubic
Lattice constant (Å)	5.6575	5.4310
Indirect energy gap (eV) at 300K	0.66	1.12
Direct Energy Gap (eV)	0.7	3.4
Electron affinity (eV)	4.0	4.05
Dielectric constant	16	11.9
Intrinsic carrier concentration (cm^{-3})	2.4×10^{13}	1.45×10^{10}
Effective density of states in conduction band N_c (cm^{-3})	1.04×10^{19}	2.8×10^{19}
Effective density of states in valence band N_v (cm^{-3})	6.0×10^{18}	1.04×10^{19}

Since the first recorded semiconductor effect in 1833, different types of semiconductor devices have been developed, based on *p-n* junctions, Schottky junctions, heterojunctions and other device structures [3]. The reduction in transistor dimensions continues to increase the speed and density of transistors in an integrated circuit, as

predicted by Moore's law [4]. The traditional Si-based top-down approach has scaled down to 18nm (Logic Half-Pitch) in 2013 [5]. However, this approach becomes more and more challenging as photolithography reaches the diffraction limit and alternative device geometries are needed [6]. Nanowires (NWs) are one of the most promising nanoscale device structures for future applications. Instead of top-down fabrication, NW growth utilizes a bottom-up self-assembly approach and thus provides better size control, for example, by controlling the size of the metal catalyst particles used for NW growth in the vapor-liquid-solid growth method [7]. Reproducible electronic properties with high yield can be easily achieved using this type of synthesis for large-scale integrated systems [8]. Moreover, by changing the components during growth, different compositions, dopant types and concentrations, as well as radial and axial heterostructures can be produced, making it possible to achieve different band alignments and device geometries for different applications as well as 3D device integration [9,10]. The NW geometry can also reduce the density of dislocations caused by lattice mismatch between materials, thus forming crystalline structures that reduce interface scattering and result in higher mobility [11-13]. Due to the one-dimensional geometry, the NW structure is also an ideal platform for quantum physics experiments [14]. The large surface-to-volume ratio significantly changes the transistor properties due to surface effects so that they can also be used as novel chemical environment sensors [15].

Control of dopant profiles in Si NWs has enabled promising applications for nanoscale electronic devices, such as sensors [16] and field-effect transistors [12]. The growth of radial heterostructures has been achieved in Ge/Si, Si/Ge [9,13,17] and *p*-Si/*n*-CdS [18] core/shell NWs, Si/Ge/Si [17] and *n*-GaN/InGaN/*p*-GaN [19] core/multishell

NWs. Axial Si/Ge heterojunctions NW have also been realized using vapor-liquid-solid (VLS) [20] and vapor-solid-solid (VSS) methods [10]. The Ge/Si core/shell NW structure has been reported to form a high-mobility hole gas due to its type-II band alignment [21] and can be integrated to operate as a field-effect transistor (FET) [13]. Different electronic transport properties have been achieved by growing Ge NWs on Si pillars using substrate etching and by changing dopant profiles [22].

In order to understand the electronic transport properties and to improve the performance of semiconductor devices, it is important to determine the electrostatic potential distribution and the concentration of electrically active dopant across the device structure. These properties become even more important as device dimensions approach the nanometer scale since quantum effects and surface area play more important roles. Although theoretical calculation and simulations enable prediction of these device properties, experimental measurements play a determining role, which imposes a challenge on the measurement method. The research of this dissertation involves the use of off-axis electron holography to characterize the electrostatic field profile across NW devices with nanoscale spatial resolution, as well as comparisons with simulations to determine the active dopants and trapped charges in the nanostructures.

1.2 Charge Distribution and Band Alignment in Semiconductors

1.2.1 *p-n* Junction

A *p-n* junction is formed by making contact between a *p*-type semiconductor and an *n*-type semiconductor. If the *p*-type and *n*-type regions are made of the same material, the junction is called homojunction. When the semiconductor materials are different, the

junction is called heterojunction. The heterojunction is discussed later. The *p*-*n* junction has unique electrical characteristics which can be used for rectifiers, light emitter diodes, solar cells and tunnel effect transistors [23-25]. Most semiconductor devices include at least one *p*-*n* junction and thus their characteristics are directly linked to the *p*-*n* junction properties.

A schematic diagram of a *p*-*n* junction is shown in Figure 1.3. The *p*-type region and *n*-type region are each uniformly doped with constant concentrations. As shown in figure 1.3(a), the Fermi level for a *p*-type semiconductor is close to the valence band, while the Fermi level is close to the conduction band for an *n*-type semiconductor. In thermal equilibrium, the intrinsic carrier concentration n_i, the electron concentrations in the conduction band n_0 and the hole concentrations in the valence band p_0 can be described by:

$$n_i^2 = N_c N_v e^{-\frac{E_g}{kT}};\ n_0 = N_c e^{-\frac{E_c - E_f}{kT}};\ p_0 = N_v e^{\frac{E_v - E_f}{kT}} \tag{1.1}$$

where N_c and N_v are the effective density of states in the conduction band and the valence band, respectively, at temperature T [25].

When *p*-type and *n*-type semiconductors make physical contact, the Fermi levels line up. The hole charge carriers in the *p*-type region diffuse into the *n*-type region, while the electron charge carriers in the *n*-type region diffuse into the *p*-type region. These diffused holes and electrons recombine and form a charge depletion region with only positive donor ions in the *n*-type region and negative ions in the *p*-type region. As the carriers diffuse across the *p*-*n* junction interface, an internal electric field is built up due to the ions, which balances the diffusion. Thus, there will be a built-in potential difference and energy band-bending across the *p*-*n* junction in thermal equilibrium. Assuming all the dopants are

ionized and that there are no free carriers in the depletion region, then the built-in potential V_{bi} and the depletion region length W can be calculated using the following equations:

$$V_{bi} = \frac{kT}{e}\ln\left(\frac{N_a N_d}{n_i^2}\right); W = \left(\frac{2\varepsilon_s V_{bi}}{e}\left(\frac{N_a+N_d}{N_a N_d}\right)\right)^{1/2} \quad (1.2)$$

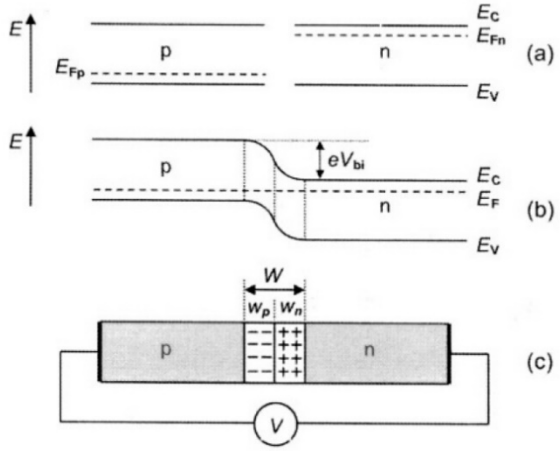

Figure 1.3 Schematic diagram of a *p*-*n* junction: (a) Energy band diagrams of *p*-type and *n*-type semiconductors. (b) Energy band diagram of a *p*-*n* junction in thermal equilibrium. (c) Depletion region of a *p*-*n* junction [26].

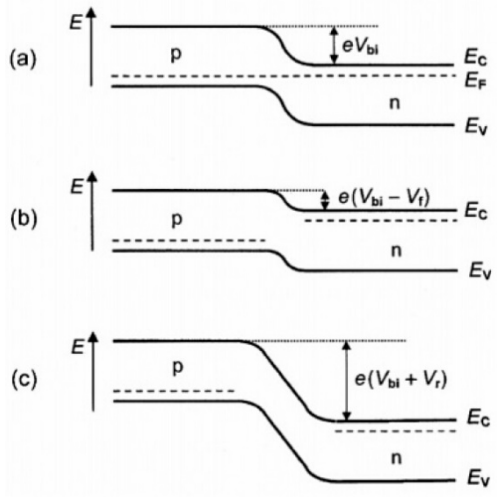

Figure 1.4 Schematic diagram of a *p*-*n* junction under different bias conditions: (a) Energy band diagram of the *p*-*n* junction with no bias. (b) Energy band diagram of the *p*-*n* junction with forward bias. (c) Energy band diagram of the *p*-*n* junction with reverse bias [26].

where ε_s is the dielectric permittivity, and N_d and N_a are the dopant concentration for donor and acceptor, respectively [25].

The band diagram of a *p*-*n* junction under different bias conditions is shown in Figure 1.4. At zero bias, if there is thermal emission or photon luminance with energy higher than E_g, electrons transfer from the valence band to the conduction band in the depletion region and form electron-hole pairs. Before recombination, these electron-hole pairs can be accelerated by the internal electric field, become separated and form current across the junction, which is the basic operating principle of the solar cell. At forward bias, the built-in potential or barrier across the *p*-*n* junction is lowered. The applied electric field is opposite to the internal electric field due to diffusion, and thus electrons (holes) in the *n*-type (*p*-type) region diffuse across the depletion region into the *p*-type (*n*-type) region and increase the minority carrier density, again forming current across the *p*-*n* junction. If the injected minority carriers recombine with majority carriers in the depletion region or in the neutral region, a photon with energy of E_g might be emitted because the electron in the conduction band transfers to the valence band and releases energy. This effect is used as the basis for light-emitting diodes. At reverse bias, the built-in potential or barrier across the *p*-*n* junction is higher. The applied electric field is in the same direction as the internal electric field due to diffusion. The depletion region becomes larger because of the stronger electric field and the higher barrier stops carriers from moving. Therefore, there will be no current through the *p*-*n* junction until the junction breaks down due to the Zener effect or an avalanche effect. The combined I-V curve characteristics for forward or reverse bias conditions are useful for rectifiers or current multipliers. The Zener effect happens when the *p*-*n* junction is heavily doped. Under reverse-bias conditions, the valence band in the

p-type region is close to the conduction band in the *n*-type region. The *p*-*n* junction depletion region is short and thus electrons can tunnel through the *p*-*n* junction from the *p*-type valence band to the *n*-type conduction band and induce current. This effect is also used as the basis for the tunneling effect transistor. The avalanche effect occurs when the electron-hole pairs generated from thermal emission in the depletion region are accelerated across the electric field in the depletion region, they hit other electrons and form more electron-hole pairs, and thus induce current [2,23-25].

1.2.2 Metal Semiconductor Contact

There are two type of contacts formed between a metal and a semiconductor: ohmic contacts and Schottky contacts. The ohmic contact shows a characteristic linear I-V curve, while the Schottky contact shows a characteristic rectifying-effect I-V curve. Both contact types have important applications in semiconductor devices and it is useful to summarize here their transport properties because of their presence in the NWs that have been studied in this dissertation research.

1.2.2.1 Schottky Contact

Figure 1.5 shows the schematic diagram of a metal and *n*-type semiconductor contact, which forms a Schottky junction. The metal and *p*-type semiconductor contact is similar and will not be described here. Before contacting the metal to the semiconductor, the Fermi level on the semiconductor side is higher compared to the metal. When they make contact, electrons flow from the semiconductor to the metal and leave positive ionized dopant atoms in the semiconductor, forming a depletion region. The built-in potential or barrier V_{bi} and the depletion region width W can then be calculated using the equations :

$$V_{bi} = \phi_m - \phi_s;\ W = \left(\frac{2\varepsilon_s(V_{bi}+V_R)}{eN_d}\right)^{1/2} \quad (1.3)$$

where V_R is the reverse bias, N_d is the semiconductor dopant concentration, and ε_s is dielectric permittivity [27]. Some typical metal work functions are shown in table 1.2.

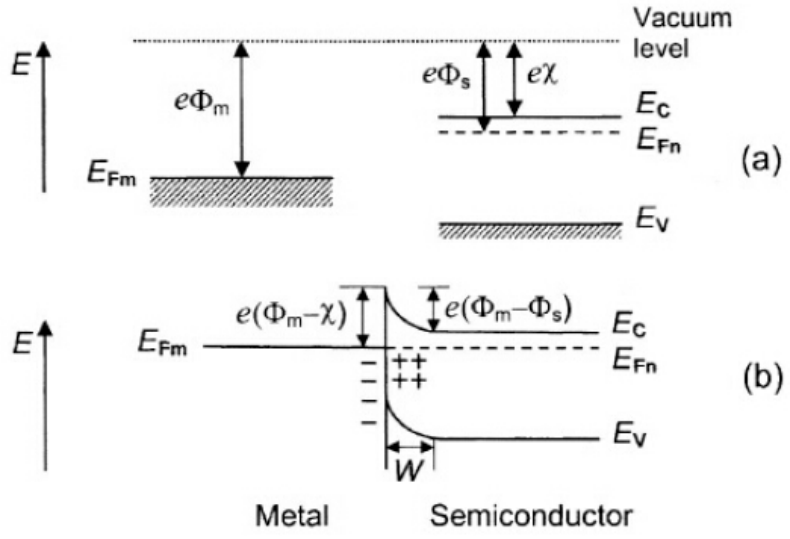

Figure 1.5 Schematic diagram of a Schottky contact: (a) Energy band diagram of metal and *p*-type semiconductor before contact. (b) Energy band diagram of Schottky contact. ϕ_m is work function for metal, ϕ_s and χ are work function and electron affinity, respectively, for semiconductor [26].

Table 1.2 Work functions of common metal contacts.

Metal	Work function(V)
Au	5.1
W	4.55
Pt	5.65

When forward bias is applied, the Fermi level on the metal side will be lower and the barrier height is reduced. Electrons can flow easily from semiconductor to metal and form current through thermal emission. When reverse bias is applied, the Fermi level on the

metal side will be higher and the barrier height as well as the depletion region width are increased. There is no current through the Schottky contact under this condition. Therefore, the Schottky contact shows similar rectifying effect as the *p*-*n* junction, although the current across the Schottky contact is mainly due to majority carriers [25].

1.2.2.2 Ohmic Contact

Figure 1.6 shows the schematic diagram of an ohmic contact between a metal and an *n*-type semiconductor. The metal and *p*-type ohmic contact is similar and is not described here. In this case, the Fermi level on the metal side is higher than for the semiconductor and electrons flow from metal to semiconductor. Because of these extra electrons, the semiconductor becomes more *n*-type and there are extra surface electrons at the metal-semiconductor interface. As positive bias is applied to the metal, electrons flow easily to the metal from the semiconductor. When negative bias is applied, electrons can also go easily through the barrier and flow to the semiconductor. Therefore, the current through the contact is proportional to the voltage [25].

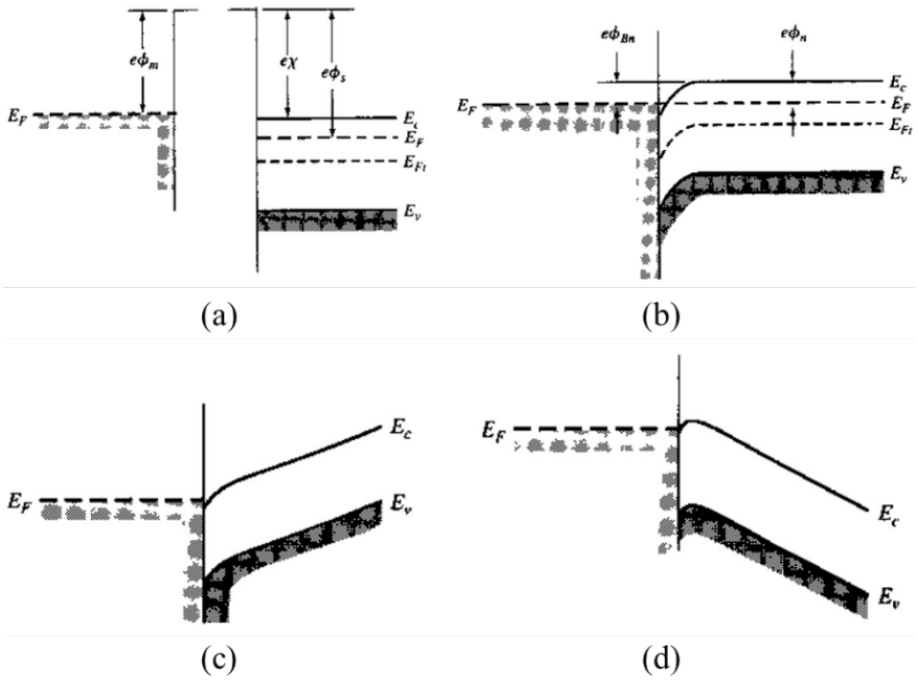

Figure 1.6 Schematic diagram of a metal-semiconductor ohmic contact: (a) Band structure of metal and semiconductor before contact. (b) Band structure of metal-semiconductor ohmic contact at thermal equilibrium. (c) Band structure of metal-semiconductor ohmic contact with positive bias on metal. (d) Band structure of metal-semiconductor ohmic contact with negative bias on metal [25].

Another type of metal-semiconductor contact is based on a tunneling effect. As shown in Figure 1.7, due to heavy dopant concentrations in the *n*-type semiconductor, the depletion region near the semiconductor surface is very narrow and electrons can easily tunnel through the barrier, forming an ohmic contact [25].

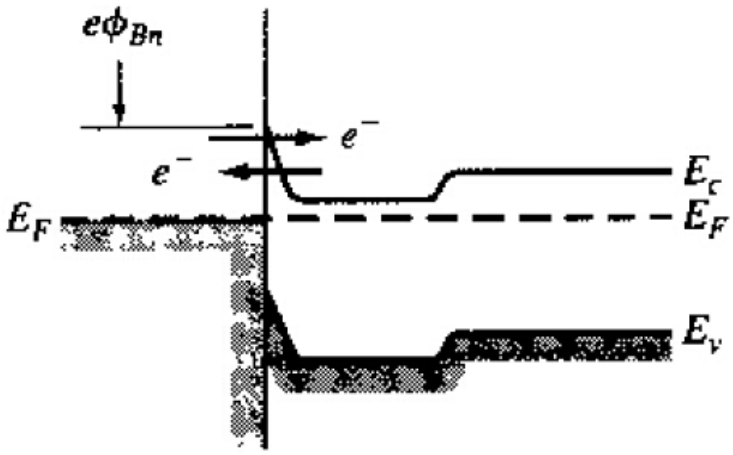

Figure 1.7 Schematic energy band structure diagram of metal and heavily doped *n*-type semiconductor [25].

1.2.3 Heterojunction

The heterojunction is formed by connecting two semiconductors of different energy band gaps. The energy band alignment (both of conduction and valence band) is usually not continuous across the heterojunction interface, due to the differences in energy band gap, electron affinity and Fermi level. Moreover, the lattice mismatch between the two materials must be small to avoid interface strain, defects and trap states. The heterojunction can also be realized by using pseudomorphic (strain layer) structures. The lattice constants and energy band gaps for common semiconductors are shown in figure 1.8. The main advantages of heterojunctions are controlling the energy barriers and potential variations at the interface in order to control the charge carrier transport, and to confine the optical radiation, which is important for optoelectronic devices [25,26].

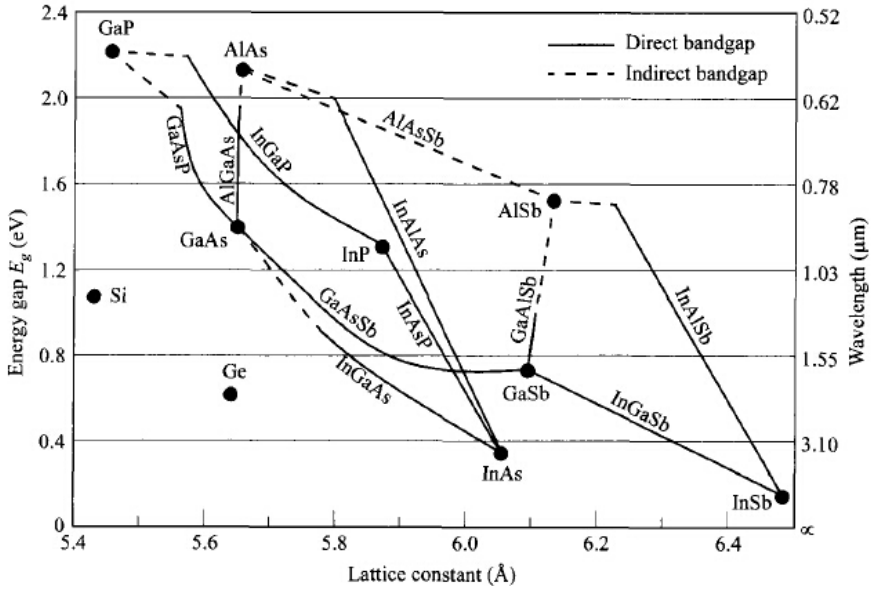

Figure 1.8 Energy band gaps and lattice constants for Si, Ge and several III-V compound semiconductors [2].

There are three different types of energy band alignment at heterojunctions, as shown in Figure 1.9. Figure 1.9a is usually referred to as type I or straddling band alignment, where one of the materials has lower E_c and higher E_v, compared to the other material, so that electrons and holes are confined in the same material. Figure 1.9b is usually referred to as type II or staggered band alignment, where the locations of lower E_c and higher E_v are displaced so that the electrons and holes are confined in different materials. Figure 1.9c is usually referred to as type III or broken-gap band alignment. Its conduction band overlaps with the valence band at the interface. Si-Ge has type II band alignment [25].

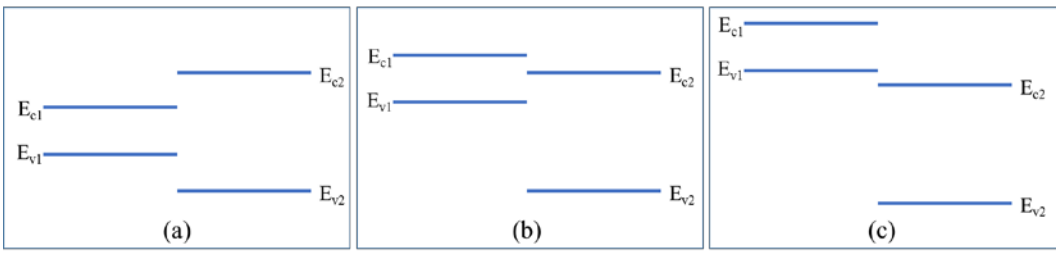

Figure 1.9 Schematic energy band diagrams for different types of heterojunctions [25].

Figure 1.10 shows a schematic energy band diagram for alignment at the heterojunction. There are several theories of band alignment for heterojunctions and the major issue is whether the band-gap discontinuities are determined by the bulk properties or by the interface properties. The electron-affinity model suggests that by using the vacuum level as the reference, the conduction-band discontinuity ΔE_c at the interface can be calculated from the difference in electron affinities of the two materials.

$$\Delta E_c = e(\chi_1 - \chi_2) \tag{1.4}$$

The discontinuity at the valence band ΔE_v can be calculated by [2,25]:

$$\Delta E_v = \left(e\chi_2 + E_{g2}\right) - (e\chi_1 + E_{g1}) \tag{1.5}$$

Moreover, when the two different materials are in contact, the Fermi levels line up to restore thermal equilibrium. In this case, the electrons (holes) in *n*-type (*p*-type) material diffuse into the other side, forming a depletion region at the interface. The resultant electric field will bend the band structure in *n*-type (*p*-type) material upward (downward), forming the discontinuity at the interface. The built-in potential V_{bi} can then be described by [26]:

$$eV_{bi} = E_{g1} + \Delta E_c - \Delta E_{F1} - \Delta E_{F2} \tag{1.6}$$

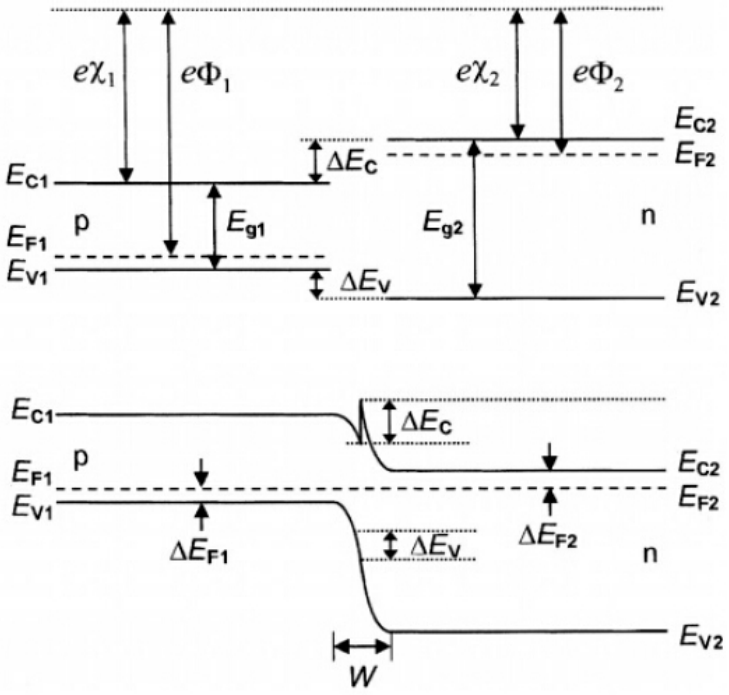

Figure 1.10 Schematic energy band diagram for heterojunctions before and after contact [26].

1.3 Growth of Semiconductor Nanostructures

1.3.1 Epitaxial Growth Techniques

Semiconductor nanowires can be grown by a wide variety of epitaxial growth techniques, which include chemical-vapor deposition (CVD) and molecular-beam expitaxy (MBE).

CVD is a technique that enables thin film growth on a suitable substrate material using chemical reaction of vapor-phase precursors to form the desired deposit. The substrate is usually used as the seed crystal, and because it uses a chemical reaction as the deposit-forming mechanism, the growth temperature can be much lower relative to the thin film melting point. The conventional CVD process can be described as follows: (a) the

precursors are evaporated and transported from the bulk gas region into the reactor chamber, using carrier gas; (b) reactive intermediates and gaseous by-products are produced from gas-phase precursor reactions; (c) reactants are transported and adsorbed by the substrate surface; (d) reactants diffuse to the growth site, and the thin film is grown by surface nucleation and chemical reactions; (e) the remaining decomposition materials are desorbed and transported out of the chamber [1,28]. The Si, Ge, Si/Ge heterojunction NWs characterized in Chapters 4, 5 and 6 were gown using a cold-wall CVD reactor using the VLS growth mechanism described below.

MBE is an epitaxial growth technique that uses the interaction of molecular or atomic beams on a heated crystal substrate surface under ultrahigh-vacuum condition. The growth rate in MBE is usually low (~1 monolayer per second) and this technique thus enables precise control of film thicknesses, compositions, dopants, and morphology. The absence of carrier gas and ultrahigh-vacuum can help to reduce the level of impurities during growth. Moreover, reflection-high-energy electron diffraction can be used for monitoring the crystal layer growth for better structure and thickness control. The MBE growth process can be described as follows: (a) solid-source atoms or homo-atomic molecules of the growth material in separate quasi-Knudsen diffusion cells are evaporated, transported and condensed on the heated crystal substrate surface. (b) atoms diffuse on the surface and react with other atoms to form the epitaxial layer [29,30]. The ZnTe thin film characterized in Chapter 3 was grown using the MBE method.

1.3.2 Nanowire Growth

Three different methods are most commonly used for growing freestanding NWs originating from the substrate surface: these are vapor-liquid-solid (VLS) [20,31-33],

vapor-solid-solid (VSS) [10,34] and solution-liquid-solid (SLS) [35-37] growth. The VLS growth has been extensively studied and it is widely used due to its simplicity and versatility. The method was firstly suggested by Wagner and Ellis to deposit micrometer-sized Si whiskers with gold impurities [31]. Figure 1.11 shows the schematic diagram of the VLS growth procedure. For the growth of Si NWs on Si substrates, gold particles are deposited on the Si substrate surface as catalysts. The substrate is heated up and precursor vapor of the growth species (SiH_4) is transported to the CVD chamber by H_2 carrier gas. SiH_4 vapor decomposes at the Au particle surface and eutectic liquid-alloy droplets of AuSi are formed after adsorbing Si atoms. The eutectic temperature of the AuSi alloy is usually much lower than the melting point of Au. The residual hydrogen by-product is taken away with the carrier gas, while Si atoms in the catalyst diffuse from the catalyst surface to the Au/Si substrate liquid/solid interface driven by the concentration gradient. When more and more Si is adsorbed into the catalyst, the eutectic alloy eventually becomes supersaturated. In order to restore equilibrium concentration, the Si component in AuSi alloy starts to precipitate at the liquid-solid interface, crystallize and form the NW structure. The AuSi alloy is pushed upwards as extra NW structure grows between the catalyst and the substrate. As the growth process continues, more Si atoms diffuse from the AuSi catalyst surface to the catalyst-NW liquid-solid interface and crystallize, making the NW longer. Therefore, the size of the Au seed controls the NW diameter, while growth time controls the NW length [35]. VSS growth can also occur along the NW surface, depending on the growth temperature, and changes the NW into a tapered shape [32,33]. During VLS growth, the Au particles act as catalyst as well as reservoir. In order to grow axial heterojunction NW, the precursor vapor has to be changed from one growth species to another. Because of the

residue of previous species in the catalyst, there is a transition region at the heterojunction interface until the residue has all precipitated. The transition length is typically about the same size as the NW diameter, as the volume of catalyst is proportional to R^3 and the diffusion interface area between liquid catalyst and solid NW is proportional to R^2, where R is the NW radius. Different metal catalysts together with the VSS method can thus be used to lower solubility in the catalyst to reduce the width of transition region [10,20,38].

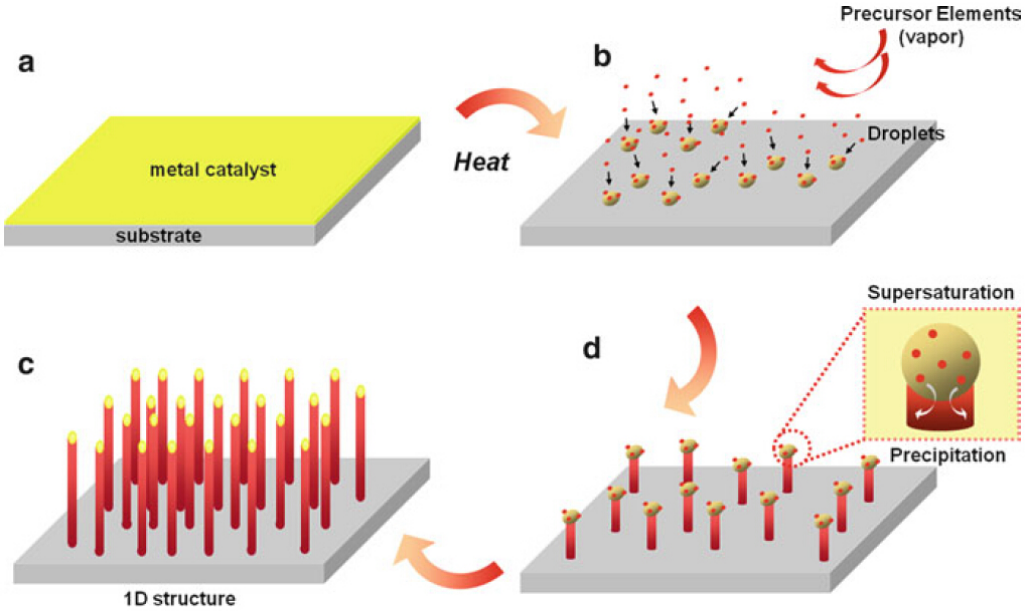

Figure 1.11 Schematic diagram of VLS NW growth [39].

1.4 Outline of Dissertation

In this dissertation research, the technique of off-axis electron holography has been used to study a range of common semiconductors, including NW homojunctions and heterojunctions. The technique was first used to measure the mean inner potentials (MIPs) and inelastic mean free paths (IMFPs) for ZnO NW and ZnTe thin films. Characterization of the electrostatic potential across Si NW with *p-n* junction, Au-Si Schottky junction in Si

NW, Si-Ge axial heterojunction NW, as well as Ge/Li_xGe core/shell NW structure were also performed using this technique and compared with Silvaco^{TM} device simulation and/or Poisson equation calculation to determine the active dopant concentrations and trapped charges in the nanostructures. Transmission electron microscopy (TEM), scanning transmission electron microscopy (STEM) and electron-energy-loss spectrum (EELS) technique were also used to characterize the morphology and structure of the nanostructures, while atom probe tomography (APT) was used to determine the total dopant concentrations and distributions in Si-Ge axial heterojunction NWs.

In Chapter 2, the background, theory and experiment setup for off-axis electron holography are briefly described. An outline procedure for electron hologram reconstruction is discussed, followed by reconstructed phase and thickness images interpretation, definition and calculation of MIPs. The basis of EELS and high-angle annular-dark-field imaging (HAADF) are also briefly discussed. Finally, the sample preparation methods used in this thesis are described.

In Chapter 3, the morphology of ZnO NWs characterized using TEM is described. The MIP and IMFP are measured using off-axis electron holography and applied to ZnO thin films for the measurement of thickness. MIP and IMFP of ZnTe thin films are also measured by combining off-axis electron holography and CBED thickness measurements. The dynamic effects due to tilting and thickness are systematically studied for ZnTe thin film by using simulations. Electrostatic potential across *p*-*n* junction in ZnTe thin film is then measured using electron holography.

In Chapter 4, measurement of electrostatic potential across *p*-*n* junction and Schottky junction in Si NW is performed using off axis electron holography. The built-in potential

is then extracted and compared with Silvaco^{TM} simulations to determine the active dopant concentrations. The influence of surface charge, transition region length and charging in the Au catalyst particle are systematically studied by comparing experiment with simulation results.

In Chapter 5, TEM and STEM HAADF are used to characterize the Si-Ge axial heterojunction NW interface, and geometry phase analysis is performed based on HAADF images. Characterization of electrostatic potential across Si-Ge axial heterojunction NWs with/without *in situ* biasing using off-axis electron holography is presented. APT is also performed to measure the total dopant concentrations and distributions. The Silvaco^{TM} simulations with/without biasing are compared with holography and APT results to determine the active dopant amounts in Si-Ge NW.

In Chapter 6, the lithiation of Ge NWs to form Ge/Li_xGe core/shell structure is outlined. The core/shell structure was characterized using TEM, STEM and EELS. Electron holography experiments were then performed on the core/shell structure during the lithiation process to measure the electrostatic potential. The measured potential was compared with Poisson equation calculation to determine the amount of trapped charge in the core/shell structure.

In Chapter 7, the important results and conclusions in the thesis are summarized, and possible topics for further investigation are briefly described.

References

[1] S. M. Sze, Semiconductor devices, physics and technology, 2nd ed. Wiley, New York, (2002).

[2] S. M. Sze, Physics of semiconductor devices, 2nd ed. Wiley, New York, (1981).

[3] M. Faraday, Experimental researches in electricity. R. and J.E. Taylor, London, (1839).

[4] G. E. Moore, Proceedings of the IEEE **86** 82 (1998).

[5] International Technology Roadmap for Semiconductors 2013, available online at http://www.itrs.net.

[6] R. Agarwal, Small **4** 1872 (2008).

[7] Y. Wu, Y. Cui, L. Huynh, C. J. Barrelet, D. C. Bell, and C. M. Lieber, Nano letters **4** 433 (2004).

[8] W. Lu, P. Xie, and C. M. Lieber, IEEE Transactions on Electron Devices **55** 2859 (2008).

[9] W. Lu, J. Xiang, B. P. Timko, Y. Wu, and C. M. Lieber, Proc. Nat. Acad. Sci. **102** 10046 (2005).

[10] C. Y. Wen, M. C. Reuter, J. Bruley, J. Tersoff, S. Kodambaka, E. A. Stach, and F. M. Ross, Science **326** 1247 (2009).

[11] V. Schmidt, H. Riel, S. Senz, S. Karg, W. Riess, and U. Gosele, Small **2** 85 (2006).

[12] J. Goldberger, A. I. Hochbaum, R. Fan, and P. Yang, Nano letters **6** 973 (2006).

[13] J. Xiang, W. Lu, Y. Hu, Y. Wu, H. Yan, and C. M. Lieber, Nature **441** 489 (2006).

[14] Y. Hu, H. O. Churchill, D. J. Reilly, J. Xiang, C. M. Lieber, and C. M. Marcus, Nature nanotechnology **2** 622 (2007).

[15] I. Kimukin, M. S. Islam, and R. S. Williams, Nanotechnology **17** S240 (2006).

[16] Y. Cui, Q. Wei, H. Park, and C. M. Lieber, Science **293** 1289 (2001).

[17] L. J. Lauhon, M. S. Gudiksen, C. L. Wang, and C. M. Lieber, Nature **420** 57 (2002).

[18] O. Hayden, A. B. Greytak, and D. C. Bell, Advanced Materials **17** 701 (2005).

[19] F. Qian, Y. Li, S. Gradecak, D. L. Wang, C. J. Barrelet, and C. M. Lieber, Nano letters **4** 1975 (2004).

[20] D. E. Perea, N. Li, R. M. Dickerson, A. Misra, and S. T. Picraux, Nano letters **11** 3117 (2011).

[21] L. Li, D. J. Smith, E. Dailey, P. Madras, J. Drucker, and M. R. McCartney, Nano letters **11** 493 (2011).

[22] L. Chen, W. Y. Fung, and W. Lu, Nano letters **13** 5521 (2013).

[23] U. K. Mishra, J. Singh, Semiconductor device physics and design. Springer, Dordrecht, The Netherlands, (2008).

[24] S. Dimitrijev, Understanding semiconductor devices. Oxford University Press, New York, (2000).

[25] D. A. Neamen, Semiconductor physics and devices : basic principles, 2nd ed. Irwin, Chicago, (1997).

[26] B. G. Yacobi, Semiconductor materials : an introduction to basic principles. Kluwer Academic/Plenum Publishers, New York, (2003).

[27] D. A. Neamen, Semiconductor physics and devices : basic principles, 3rd ed. McGraw-Hill Higher Education, London, (2003).

[28] A. C. Jones, M. L. Hitchman, and Knovel (Firm), Chemical vapour deposition precursors, processes and applications. Royal Society of Chemistry, Cambridge, UK, (2009).

[29] J. Y. Tsao, Materials fundamentals of molecular beam epitaxy. Academic Press, Boston, (1993).

[30] M. A. Herman and H. Sitter, Molecular beam epitaxy : fundamentals and current status, 2nd, rev. and updated ed. Springer, New York, (1996).

[31] R. S. Wagner and W. C. Ellis, Applied Physics Letters **4** 89 (1964).

[32] J. W. Dailey, J. Taraci, T. Clement, D. J. Smith, J. Drucker, and S. T. Picraux, J Appl Phys **96** 7556 (2004).

[33] S. A. Dayeh, J. Wang, N. Li, J. Y. Huang, A. V. Gin, and S. T. Picraux, Nano letters **11** 4200 (2011).

[34] Y.-C. Chou, C.-Y. Wen, M. C. Reuter, D. Su, E. A. Stach, and F. M. Ross, ACS Nano **6** 6407 (2012).

[35] V. Schmidt, J. V. Wittemann, S. Senz, and U. Gösele, Advanced Materials **21** 2681 (2009).

[36] M.-S. Kim and Y.-M. Sung, Chem Mater **25** 4156 (2013).

[37] A. T. Heitsch, D. D. Fanfair, H.-Y. Tuan, and B. A. Korgel, J Am Chem Soc **130** 5436 (2008).

[38] N. Li, T. Y. Tan, and U. Gösele, Applied Physics A **90** 591 (2008).

[39] G.-C. Yi, Semiconductor Nanostructures for Optoelectronic Devices Processing, Characterization and Applications, Springer, Heidelberg, (2012).

CHAPTER 2

EXPERIMENTAL DETAILS

This chapter begins by providing some background and basic theory of off-axis electron holography. The procedures used for hologram reconstruction are then described, followed by details of reconstructed phase and thickness image interpretation, definition and calculation of mean inner potential (MIP), and the experimental setup used for recording electron holograms. The basis of electron-energy-loss spectroscopy (EELS) and high-angle annular-dark-field (HAADF) imaging are also briefly discussed. Finally, the sample preparation methods used for the research of this dissertation are illustrated.

2.1 Off-Axis Electron Holography

2.1.1 Introduction

Transmission electron microscopy (TEM) has been widely used to characterize nanostructured materials. However, conventional TEM only provides spatial intensity information about the sample, while the phase and amplitude of the specimen exit-surface electron wavefunction are unavailable. The phase and amplitude information are directly related to the electrostatic and magnetic fields of the sample, which are very important for characterization of semiconducting and magnetic materials.

Electron holography is an electron-interference technique that can provide amplitude and phase information about the sample with nanoscale spatial resolution [1]. By overlapping the exit-surface electron wave with a reference wave, an interference pattern (hologram) is formed, which allows retrieval of phase and amplitude information. The

technique of in-line holography was first proposed by Gabor as a method for correcting the spherical aberration of the objective lens, thus overcoming the interpretable resolution limit [2]. Leith and Upatnieks proposed the off-axis electron holography geometry as a way to solve the twin-image problem of in-line holography, by overlapping the sample wave with the vacuum (reference) wave using an electrostatic biprism [3]. However, the approach was not effectively realized experimentally until the development of the field emission gun (FEG). The FEG provides a high brightness and highly coherent electron beam, which is critical for hologram interference [4,5]. The holograms were originally recorded on photographic plates with non-linear response and the hologram reconstruction was done using a light optical system [6]. The emergence of digital recording devices, such as the slow-scan charge-coupled-device (CCD), which provides linear response over a wide dynamical range of electron counts, has enabled quantitative reconstruction of electron hologram using computer processing [7].

Since the initial realization of electron holography, the technique has been extensively developed and over twenty different approaches for the realization of electron holography have been identified [8]. Among these approaches, off-axis electron holography with operation in the TEM imaging mode is the most widely used and most successful technique for obtaining sample phase and amplitude information [9]. This setup has been exclusively used for the holography experiments described in this dissertation research.

2.1.2 Theory and Hologram Reconstruction

A schematic diagram for off-axis electron holography with operation in the TEM imaging mode is shown in Figure 2.1. Parallel (coherent) electron illumination from the

field emission gun (FEG) electron source is provided using the condenser lens system. When the electron wave passes the specimen plane, it can be considered as being split into two different parts. Part of the electron wave passes through the specimen, and will contain phase and amplitude information that can be related to the sample. This object wave can be described by the following equation:

$$\Psi(\vec{r}) = A(\vec{r})\exp(i\varphi(\vec{r})) \tag{2.1}$$

where $A(\vec{r})$ and $\varphi(\vec{r})$ are the amplitude and phase, respectively, at the two-dimensional exit-surface of the sample. Part of the electron wave passes only through vacuum and serves as the reference wave $\Psi_r(\vec{r})$.

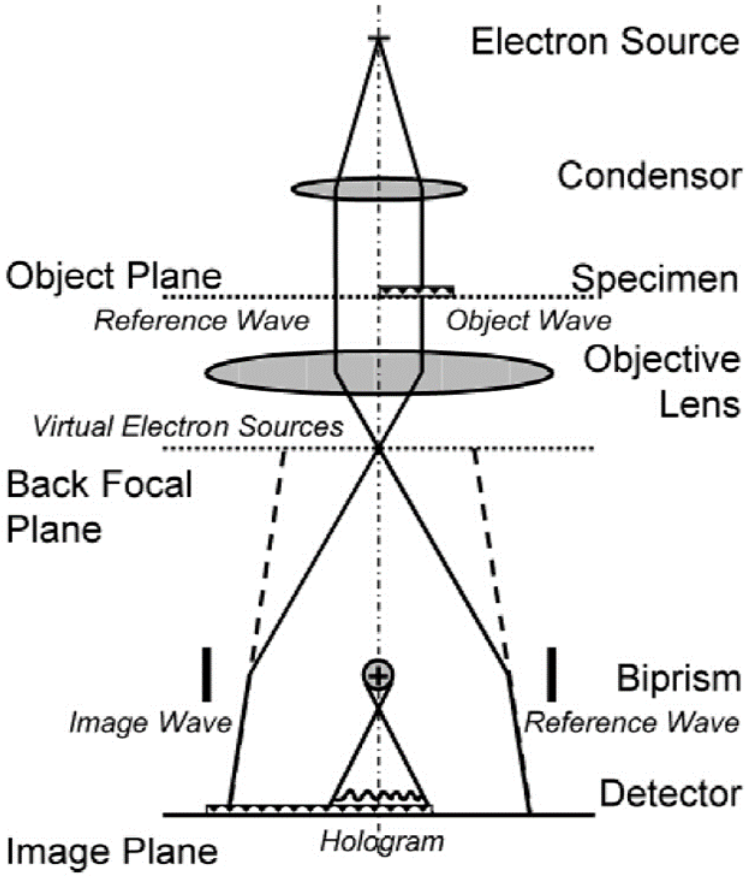

Figure 2.1 Schematic diagram showing the TEM components essential for the technique of off-axis electron holography [9].

When the electrostatic biprism below the specimen is positively charged, the object and reference waves are deflected towards each other and overlap, eventually forming an interference hologram in the final image plane where the CCD is located.

The hologram intensity $I_{hol}(\vec{r})$ recorded by the CCD can be described by the following equation [9]:

$$I_{hol}(\vec{r}) = |\Psi(\vec{r}) + \Psi_r(\vec{r})|^2 = 1 + A^2(\vec{r}) + 2\mu A(\vec{r})\cos(2\pi\vec{q}_c \cdot \vec{r} + \varphi(\vec{r})) \qquad (2.2)$$

where $|\vec{q}_c| = \alpha_c/\lambda$ is the carrier frequency of the interference fringes. α_c is the deflection angle between the reference wave and the object wave, which depends on the biprism voltage, and λ is the electron wavelength [10]. The first two terms represent the central auto-correlation function, and the desired phase information is encoded in the third term. μ is defined as the contrast, which is given by the equation [9]:

$$\mu = |\mu_{sc}\mu_{tc}||\mu_{inel}||\mu_{inst}|MTF \qquad (2.3)$$

where μ_{sc} is due to limited spatial coherence from the finite FEG source size, μ_{tc} is due to the finite temporal coherence caused by beam energy spread, μ_{inel} is due to any inelastic interactions in the specimen, μ_{inst} is due to any instabilities of the imaging system, and MTF is the modulation transfer function of the final detector. The combination of these effects reduces the effective beam coherence and hence the contrast of the interference fringes. The amplitude $A(\vec{r})$ and phase $\varphi(\vec{r})$ information about the sample are included in the recorded hologram according to equation (2.2).

In order to extract the amplitude and phase information from the recorded hologram, procedures for electron hologram reconstruction are needed, as illustrated in Figure 2.2. Fourier transformation of the hologram $I_{hol}(\vec{r})$ gives the following result [10]:

$$FT\{I_{hol}(\vec{r})\} = \delta(\vec{q}) + FT\{A^2(\vec{r})\} \qquad \text{center band}$$

$$+\mu FT\{A(\vec{r})\exp(i\varphi(\vec{r}))\} \otimes \delta(\vec{q} - \vec{q}_c) \qquad +(\text{sideband})$$

$$+\mu FT\{A(\vec{r})\exp(-i\varphi(\vec{r}))\} \otimes \delta(\vec{q} + \vec{q}_c) \qquad -(\text{sideband}) \quad (2.4)$$

The center band corresponds to the Fourier transform of the conventional image intensity, while amplitude and phase information are contained in the two sidebands. The two sidebands are at a distance $|\vec{q}_c|$ away from the image center and they are conjugate to each other.

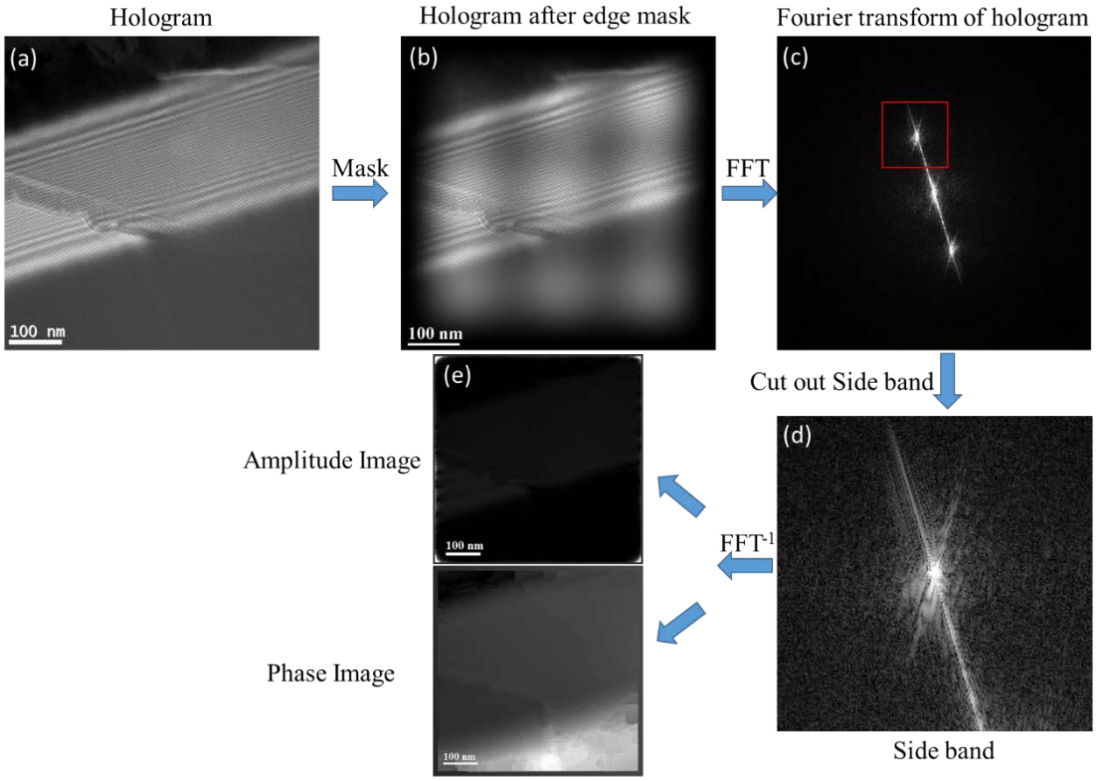

Figure 2.2 Schematic diagram illustrating the procedure for hologram reconstruction: (a) Original hologram; (b) A Hanning window is applied to the hologram to smoothen the edges; (c) Fourier transform of the hologram; (d) Extract one of the side bands; (e) Inverse Fourier transform of side band allows extraction of amplitude and phase images.

One of the sidebands is extracted, while the other parts are masked. The center of the sideband is shifted to $\vec{q} = \vec{q}_c$, to cancel the effect of the $\delta(\vec{q} - \vec{q}_c)$ term. An inverse Fourier transform is then performed, which gives the complex exit-surface wavefunction:

$$\Psi_{obj}(\vec{r}) = \mu A(\vec{r})\exp(i\varphi(\vec{r})) \tag{2.5}$$

The phase and amplitude of the image can then be calculated by extracting the real part $\Psi_{obj}(\vec{r})_{re}$ and the imaginary part $\Psi_{obj}(\vec{r})_{im}$ of equation 2.5, as given by the following equations:

$$phase = \varphi(\vec{r}) = \arctan\left(\Psi_{obj}(\vec{r})_{im} \Big/ \Psi_{obj}(\vec{r})_{re}\right) \tag{2.6}$$

$$amplitude = \mu A(\vec{r}) = sqrt\left(\Psi_{obj}(\vec{r})_{re}{}^2 + \Psi_{obj}(\vec{r})_{im}{}^2\right) \tag{2.7}$$

The procedure described above can provide phase and amplitude information using the object hologram only, but several practical details need attention during hologram reconstruction before quantitative information can be obtained. A reference hologram as well as the object hologram needs to be recorded. The hologram containing the sample region of interest is termed the object hologram, while the hologram taken with vacuum only but without the sample present is termed the reference hologram. The reference hologram serves three purposes: (a) Define the center of side band $\vec{q}_c$; (b) Cancel out any distortions of the projector lenses and the CCD; and (c) Reduce the effect of Fresnel fringes recorded in the hologram, which can cause continuous frequencies between the image center and the sidebands in the Fourier transform.

After reconstruction of the reference hologram, the end result is:

$$\Psi_{ref}(\vec{r}) = \mu A_{ref}(\vec{r})\exp(i\varphi_{ref}(\vec{r})) \tag{2.8}$$

The exit-surface wavefunction $\Psi_{sample}(\vec{r})$ can then be calculated using:

$$\Psi_{sample}(\vec{r}) = \frac{\Psi_{obj}(\vec{r})}{\Psi_{ref}(\vec{r})} = \frac{A_{obj}(\vec{r})}{A_{ref}(\vec{r})} \exp(i((\varphi_{obj}(\vec{r}) - \varphi_{ref}(\vec{r}))) \quad (2.9)$$

Thus, the phase and amplitude of the sample are relative to the nearby vacuum. The amplitude should be 1 in vacuum and the phase shift should be 0, assuming that there are no external electric or magnetic fields.

A mask must be applied to the hologram before carrying out the Fourier transform, in order to smooth out the sharp hologram edges which cause a continuous strip that crosses the Fourier transform. Moreover, because the arctan function is used to recover the phase information, there will be a phase-wrapping problem when the phase change exceeds the range of (0,2π). A phase-unwrapping algorithm is thus needed in order to obtain a continuous phase change in the reconstructed phase image. Those developed by Goldstein and Flynn are suitable for this purpose [11]. It is sometimes also necessary to avoid areas where phase unwrapping is not successful during the hologram processing.

When the electron beam passes through regions with electric and/or magnetic fields, the phase of the electron beam will be changed. The phase shift of the electron wave that passes through the sample, relative to the reference electron wave that passes only through vacuum, is given by the following equation [7]:

$$\varphi(x,y) = C_E \int V(x,y,z)dz - \frac{e}{\hbar} \int \vec{B}(x,y,z)d\vec{A} \quad (2.10)$$

where z is along the incident electron beam direction, x and y are the sample in-plane directions, V(x, y, z) is the electrostatic potential, $\vec{B}(x,y,z)$ is the magnetic field and $\vec{A}$ is the area parallel to the beam direction. The electron-beam energy-dependent interaction constant C_E is given by [7,12]:

$$C_E = \frac{2\pi e}{\lambda E}\frac{E+E_0}{E+2E_0} \tag{2.11}$$

where E and E_0 are the kinetic and rest-mass electron energies, respectively, and λ is the incident beam wavelength. For 200keV and 300keV electrons, C_E is equal to 0.00728 rad/(V·nm) and 0.00653 rad/(V·nm), respectively.

For semiconductors, there are usually no magnetic fields present and the phase shift due to any electrostatic fields in the semiconductor can be calculated using [7,13]:

$$\varphi(x,y) = C_E \int V(x,y,z)dz = C_E \int (V_0(x,y,z) + V_{bi}(x,y,z))dz \tag{2.12}$$

where V_{bi} is the built-in potential in the semiconductor due to charge distribution and V_0 is the mean inner potential (MIP), which is discussed in more detail later. The integration is taken through the thickness of the sample along the electron-beam direction.

The sample thickness can be calculated using the amplitude image [14]. In electron-energy-loss spectroscopy, the sample thickness t can be determined by relating the zero-loss intensity I_0 to the total electron intensity I_{total}, as given by [15]:

$$I_0 = I_{total}\exp(-\frac{t}{\lambda_i}) \tag{2.13}$$

where λ_i is the electron inelastic mean free path (IMFP).

In electron holography, only the coherent elastically scattered electrons contribute to the sidebands, since the sideband is formed by electron interference. Thus, the amplitude of the sample A_{sample} and the vacuum A_{vacuum} can be directly related to the zero-loss electron intensity I_0 and the total electron intensity I_{total}, and used for calculation of the sample thickness, as given by the following equation [14]:

$$t = -\lambda_i \ln\left(\frac{I_0}{I_{total}}\right) = -\lambda_i \ln\left(\frac{A_{sample}}{A_{vacuum}}\right)^2 = -2\lambda_i \ln(\frac{A_{sample}}{A_{vacuum}}) \tag{2.14}$$

2.1.3 Mean Inner Potential

The Mean Inner Potential (MIP) is an important parameter in electron holography experiments. It is usually defined as the volume average of the scalar potential in the solid due to incomplete electron-shell screening of atomic cores [16]. Its value is negative and usually in the range of -5V to -30V, depending on the sample composition and structure. Because of this non-zero crystal potential, electrons in the crystal are accelerated relative to the beam that goes through the vacuum. Thus, their phases are ahead of the electron beam in vacuum. The MIP can be calculated by the zero-order Fourier coefficient of the crystal potential and taken as an *ad hoc* zero in infinitely large perfect crystals [16,17]. The crystal MIP depends on the sum of dipole and quadrupole moments in the unit cell and thus it is sensitive to the redistribution of outer valence electrons caused by bonding [18]. It is also proportional to the second moment of the charge density for an atom, and depends on the effective atomic sizes in the crystal [19,20].

Based on the definition, the MIP can be calculated using the following equation [12]:

$$V_0 = \frac{1}{\Omega}\int_{\Omega} V(\vec{r})d\vec{r} \tag{2.15}$$

where Ω is the volume of a unit cell in the crystal or the volume of the material in a disordered solid. This calculation requires knowledge of the potential distribution in the crystal unit cell, which is usually non-trivial.

The non-binding approximation can be used as a simple approach to calculate the MIP value, by assuming that the solid is composed of an array of free neutral atoms. This is described by the following equation [12,17,21]:

$$V_0 = \frac{h^2}{2\pi m_0 e\Omega}\sum_j f_j(0) \tag{2.16}$$

where $f_j(0)$ are the atomic scattering amplitudes for the forward scattered electrons and the equation averages the $f_j(0)$ of all atoms in the unit cell over the unit-cell volume. This model depends on the incident electron-beam energy because of the atomic scattering amplitudes used [22], and usually overestimates the MIP value because it does not include the effect of valence electron redistribution due to bonding. Thus, it can serve an upper limit for the value of the MIP [12].

The lower limit of the MIP value can be calculated using a binding model where atoms at the lattice sites are ionized and the valence electrons are distributed uniformly [23]. Thus, the MIP would be equal to the contributions from all of the ionized free atoms plus contributions from free valence electrons in the unit cell. The latter result is given by the following equation [24]:

$$V_0 = -\frac{3}{10}\frac{ep}{4\pi\epsilon_0 r_0} \tag{2.17}$$

where p is the number of free valence electrons of the atom and r_0 is the radius of a sphere that has the same volume as the atom.

Ross and Stobbs proposed an empirical rule to compromise between the non-binding and binding models, which is given as follows [25]:

$$\frac{V_0(Radi)}{V_0(Doyle\ and\ Turner)} = \frac{0.0325Z}{\Omega} + 0.6775 \tag{2.18}$$

where $V_0(Radi)$ is the MIP obtained by averaging the upper and lower limit values calculated by Radi with atomic scattering amplitudes from Herman and Skillman, and $V_0(Doyle\ and\ Turner)$ is the MIP calculated using the non-binding model (upper limit) with Doyle and Turner scattering amplitudes for neutral atoms. Thus, the MIP can be calculated first using the non-binding model, and the bonding effects can then be included

by using equation (2.18). However, this equation can only serve as a guide and the exact value should preferably be determined by experiment [12].

Density functional theory (DFT) can be used to calculate the MIP value. A crystal slab of finite thickness, but infinite and periodic in lateral dimensions, is assumed for DFT calculations, and Full Potential Linearized Augmented Plane-Wave (FLAPW) Local Density Approximation (LDA) method is used to calculate the crystal ground-state charge density [26]. The MIP can then be calculated either by using Poisson's equation, averaged over the unit cell, or by using the following equation:

$$V_0 = -\frac{1}{\Omega}\iint \frac{\rho(\vec{r})}{\left|\vec{r}-\overrightarrow{r'}\right|} d\vec{r}\,d\overrightarrow{r'} = \frac{2\pi}{3\Omega}\int r'^2 \rho(\overrightarrow{r'})\, d\overrightarrow{r'} \tag{2.19}$$

where $\rho(\overrightarrow{r'})$ is the charge density distribution in the unit cell and the integration is taken over the whole unit cell.

2.1.4 Experimental Setup

The off-axis electron holography experiments described in this dissertation have been performed using a Philips-FEI CM200 and an FEI Titan 80-300. The geometry is illustrated in Figure 2.3. The Schottky FEG provides the high-brightness coherent electron beam that is essential for interference experiments. The electron beam is stigmated into a long elliptical strip using the condenser lens stigmators such that only the central, most coherent, part of the focused beam is used to illuminate the sample, as shown in Figure 2.4 [7]. The electron beam along the longer axis is almost parallel, while there may be several milliradian beam convergence across the shorter illumination axis [27].

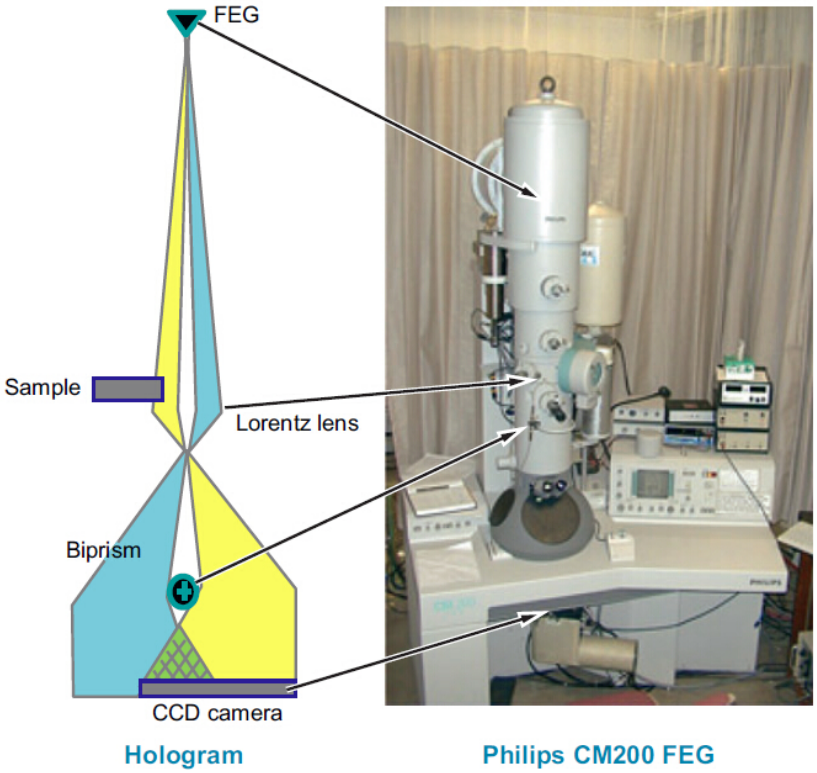

Figure 2.3 Schematic illustration of the off-axis electron holography setup using the Philips-FEI CM200 [7].

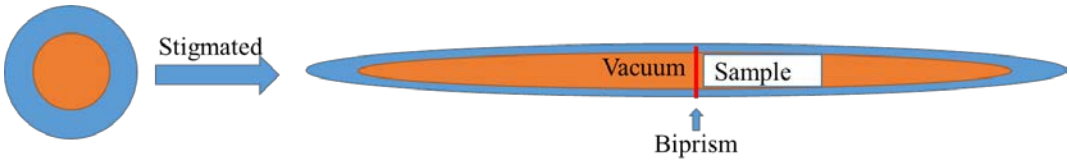

Figure 2.4 Schematic diagram showing the round beam (left) and stigmated beam (right). The orange part is the most coherent region of the beam.

There are three distinct operating modes for forming off-axis holograms, using three different imaging lenses. The first one uses the objective lens, and is the same TEM geometry as the normal high-resolution imaging mode. This mode can give high spatial

resolution (up to atomic resolution), but the field of view is limited (<100nm). The second geometry uses the diffraction mode, obtained by turning off the diffraction lens. This mode gives medium spatial resolution (1~5nm) and moderate field of view (~150nm). The last geometry uses a weak mini-lens, often referred to as a Lorentz lens, which is located below the objective lens, often within the bore of the lower pole-piece. In this operating mode, the objective lens is turned off. Because of the weak excitation of the mini-lens and its lower position, there should be no residual magnetic field at the position of the sample, which is ideal for imaging magnetic materials. This operating mode also gives lower spatial resolution (nanometer scale), but provides larger fields of view (~1micron). In this dissertation research, a Lorentz lens has been used for studying most samples in order to take advantage of the larger field of view.

The (rotatable) biprism is located at the plane of the selected-area electron diffraction (SAED) aperture. It is usually made of quartz and coated with platinum, and the diameter is usually ~400-750 nm. A positive voltage is applied to the biprism such that the object wave and the reference wave are attracted toward each other to form an interference pattern. In our experimental setup, the interference holograms are formed just below the SAED aperture and a positive voltage in the range of ~100V-150V must be applied. As the biprim voltage is increased, the fringe spacing and the fringe contrast decrease, while the field of view and spatial resolution after reconstruction increase. Thus, the voltage chosen is a compromise. The most stable position for the biprism in the CM200 is parallel to the viewing window in front of the user. The stigmated electron beam is then rotated perpendicular to the orientation of the biprism such that the most coherent electrons are distributed on both sides of the biprism, as shown in Figure 2.4.

The interference fringe contrast is commonly used to evaluate the quality of the holography setup. Higher contrast provides better signal-to-noise ratio and thus greater phase accuracy can be obtained. The fringe contrast μ is usually defined by the following equation:

$$\mu = \frac{I_{max} - I_{min}}{I_{max} + I_{min}} \tag{2.20}$$

where I_{max} and I_{min} are the highest and lowest intensities, respectively, in the hologram.

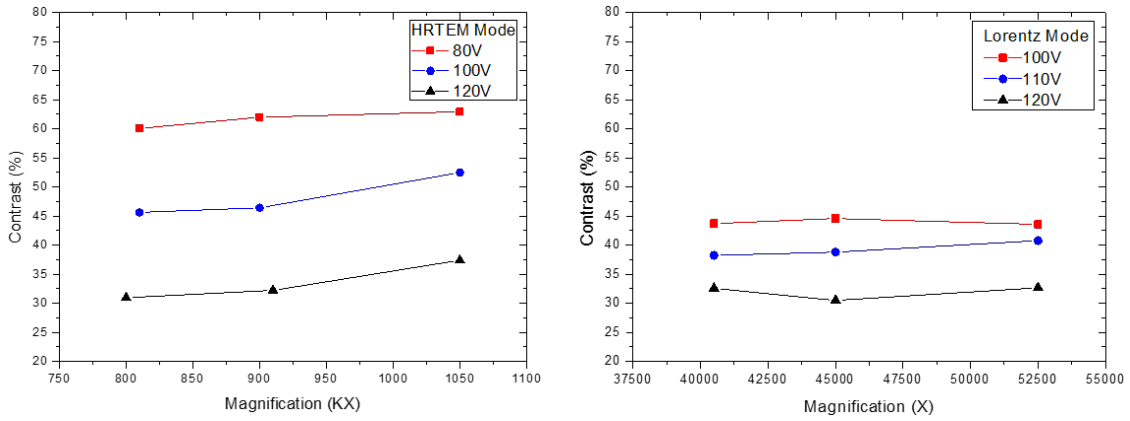

Figure 2.5 Contrast measurements in HRTEM mode (left), and Lorentz mode (right), with different magnifications and biprism voltages. The electron-beam energy was 200keV and the hologram exposure time was 1 second.

Measurements of fringe contrast for the CM200 are shown in Figure 2.5. As the biprism voltage was increased, the contrast of the fringes decreased and the fringe contrast increased when the magnification was increased. Thus, it should be apparent that the biprism voltage and the magnification need to be carefully considered, in order to reach the highest possible fringe contrast for the desired field of view as well as spatial resolution.

The fringe contrast for experimental holography should usually be at least 20% to ensure sufficient accuracy in the phase measurements.

2.2 Scanning Transmission Electron Microscopy

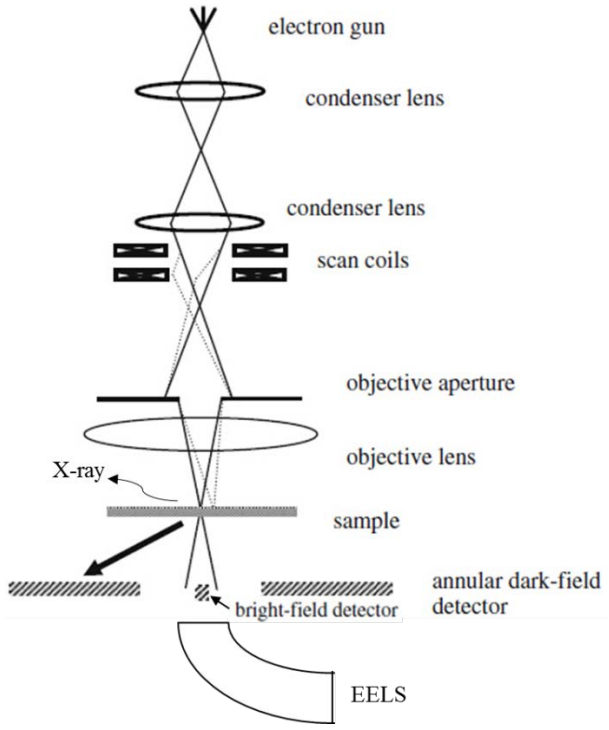

Figure 2.6 Schematic diagram showing the microscope geometry, signals and detectors for scanning transmission electron microscopy [28].

A schematic diagram of the experimental setup for scanning transmission electron microscopy (STEM) is shown in Figure 2.6. The FEG provides a coherent electron source, and the condenser lens system and the objective lens focus the electron beam into a sub-nanometer-size probe (0.1~1nm) incident on the sample. Deflector coils below the condenser lens system scan the electron probe across the sample. An objective aperture before the sample is used to exclude higher-angle contributions to the focused probe, which

will otherwise lead to probe-blurring because of aberrations of the objective lens [28]. The electron probe passes through the sample and electrons are scattered at different angles. The STEM image is formed by successfully collecting electrons scattered at different probe positions, and the magnification is determined by the area scanned on the sample relative to the final monitor.

Four different types of signals can be collected after the electron-sample interactions have taken place [28]: (a) Transmitted electrons that are scattered at low angles (smaller than the incident-beam convergence angle). This signal represents the bright-field image. (b) Electrons scattered at high angles (usually several times the incident beam convergence angle). Annular-dark-field images are formed by collecting this signal. High-angle annular-dark field (HAADF) imaging usually refers to collection angles of greater than ~50mrad, and the signal intensity then depends on the sample atomic number Z^{α} ($\alpha \sim 1.5$-2.0, depending on the inner collection angle) [29]. (c) Transmitted electrons which have lost energy due to electron-sample interactions, can be collected by an electron spectrometer. This operation mode is referred to as electron-energy-loss spectroscopy (EELS). By measuring the electron distribution as a function of energy loss, the elements in the sample, bonding conditions and electron-sample interactions can be determined [15]. (d) X-rays generated by electron excitations in the sample when atoms return to their ground state after energy is absorbed from incident electrons. This mode is referred to as Energy-dispersive X-ray spectroscopy (EDX) [30]. The EDX technique can be used to determine elemental composition and distribution in the sample but no local bonding information is available. In the research of this dissertation, HAADF, EDX and EELS have been used to determine the structure and local composition in semiconductor nanowires (NWs).

2.3 Electron-Energy-Loss Spectroscopy

When the incident electron beam passes through the sample, coulombic interactions between the electron beam and atoms in the sample cause inelastic scattering so that some of the incident beam energy is lost to the sample. By analyzing the electron distribution in the EELS spectrum as a function of energy, the excitation spectrum of the sample can be extracted.

The EELS spectrum can be divided into three regions: zero-loss peak, low-loss region and core-loss region. The zero-loss peak is caused primarily by the transmitted electrons without any energy loss. For thin specimens, this peak is the most intense signal in the EELS spectrum. The spatial resolution and contrast of images can be enhanced by using this peak to filter out the inelastically scattered electrons [30]. The low-loss region is usually in the range of ~5eV-50eV. This region is related to plasmon excitations, dielectric properties, band gap, interband transitions and surface boundary effects, and is caused by interactions of the fast electron beam with outer shell electrons near the Fermi level of the material [28,30]. The combination of the zero-loss peak and the low-loss region can be also used to estimate the local thickness of the sample t, as given by the following equation [31]:

$$\frac{I_0}{I_{total}} = e^{-\frac{t}{\lambda_i}} \tag{2. 21}$$

where I_0 is the intensity of the zero loss peak, I_{total} is the total intensity including zero-loss peak and low-loss region, and λ_i is the inelastic mean free path. The core-loss region is usually in the energy range above 100eV, and is caused by inelastic interactions between the electron beam and inner/core shell electrons of the material. When the inner-shell electrons get enough energy from the electron beam, electrons transfer from the inner shells

to empty states and the atom is ionized. Therefore, the core-loss region is related to the inner-shell electron orbits and can be used for elemental identification and quantification. Moreover, the energy-loss near-edge structure (ELNES) within ~50eV of the ionization energy is sensitive to local bonding and can often be used for identifying atom bonding conditions in the material [28,30,31].

In general, EELS has higher energy resolution and better spatial resolution, compared to EDX, which is a secondary effect of electron excitation caused by x ray emission when electrons return to the ground state. The EELS technique is preferred for light elements, while EDX is restricted by the fluorescence yield and absorption. However, EELS cross-sections decrease rapidly for heavier elements, and the signal-to-noise ratio is low, whereas EDX has strong signal-to-noise ratio. Therefore, EDX and EELS can be considered as complementary [30]. The core-loss part of the EELS spectrum has been used in this research to determine NW elemental distributions.

2.4 Sample Preparation

Proper sample preparation is essential for electron holography experiments because of its impact on the phase measurements. In addition to electron transparency, large areas of nearby vacuum are needed for the reference wave.

The NW samples have been prepared for observation using the following procedure: (a) A small piece of substrate with upright NWs is cut off and put into isopropyl alcohol (IPA). (b) The IPA with substrate is sonicated for 30s. The NWs are removed from the substrate and float in the IPA solution. (c) The IPA solution with NWs is transferred to a TEM grid with lacey carbon film or solid carbon thin film (thickness of several nanometers)

using a pipette. (d) The TEM grids with NWs are air-dried or else heated at slightly elevated temperature by using a heating lamp. The lacey carbon films have non-uniform holes, and it is sometimes difficult to find features of interest in the vacuum with another large area nearby for interference purposes. Solid carbon thin films are thus often preferred and they still provide uniform background, which can serve as the reference wave.

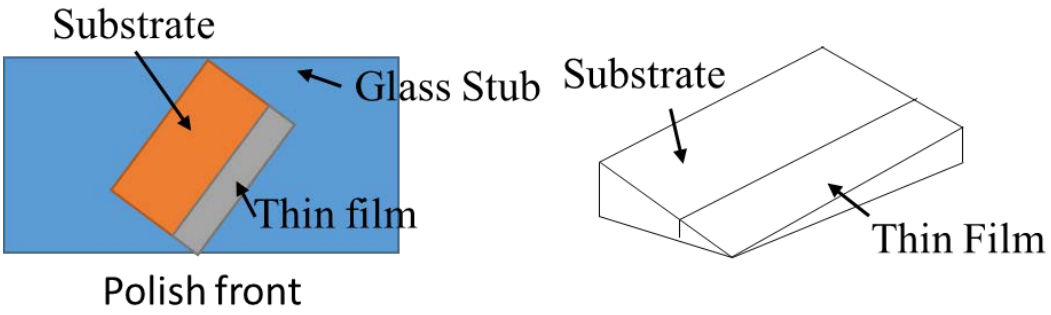

Figure 2.7 Schematic diagrams showing: the orientation of the sample relative to the polishing glass stub (left), and the desired geometry of the sample (right).

For thin-film samples grown epitaxially on substrates, it is usually necessary to prepare the samples with specific shapes (usually wedge shape). The Multiprep^{TM} wedge-polishing apparatus manufactured by Allied High Tech Products was utilized for sample preparation. Diamond lapping films with grain sizes of 30 µm, 9 µm, 3 µm, 1 µm, 0.5 µm and 0.1 µm, followed by cloth polishing, were sequentially used to polish the sample and to reduce any artifacts due to polishing. The first side of the sample was usually polished to obtain a smooth surface. A small angle (1˚-2˚) was introduced when polishing the second side in order to achieve a wedge-shaped sample [32]. The sample geometry and the orientation of the sample relative to the glass stub are shown in Figure 2.7. After wedge

polishing, the sample was typically ion-milled at 2keV for ~10 minutes to clean up any debris remaining on the sample surface.

References

[1] M. R. McCartney, N. Agarwal, S. Chung, D. A. Cullen, M.-G. Han, K. He, L. Li, H. Wang, L. Zhou, and D. J. Smith, Ultramicroscopy **110** 375 (2010).

[2] D. Gabor, Proceedings of the Royal Society of London. Series A. Mathematical and Physical Sciences **197** 454 (1949).

[3] E. N. Leith and J. Upatnieks, J. Opt. Soc. Am. **52** 1123 (1962).

[4] G. Möllenstedt and H. Wahl, Naturwissenschaften **55** 340 (1968).

[5] A. V. Crewe and J. Wall, Journal of Molecular Biology **48** 375 (1970).

[6] A. Tonomura, Reviews of Modern Physics **59** 639 (1987).

[7] M. R. McCartney and D. J. Smith, Annual Review of Materials Research **37** 729 (2007).

[8] J. M. Cowley, Ultramicroscopy **41** 335 (1992).

[9] M. Lehmann and H. Lichte, Microscopy and Microanalysis **8** 447 (2004).

[10] H. Lichte, P. Formanek, A. Lenk, M. Linck, C. Matzeck, M. Lehmann, and P. Simon, Annual Review of Materials Research **37** 539 (2007).

[11] D. C. Ghiglia and M. D. Pritt, Two-dimensional phase unwrapping : theory, algorithms, and software. Wiley, New York, (1998).

[12] M. Gajdardziska-Josifovska and A. H. Carim, Chapter 12, Introduction to electron holography, Kluwer Academic/Plenum Publishers, New York, (1999).

[13] M. I. den Hertog, H. Schmid, D. Cooper, J. L. Rouviere, M. T. Bjork, H. Riel, P. Rivallin, S. Karg, and W. Riess, Nano letters **9** 3837 (2009).

[14] M. R. McCartney and M. Gajdardziska-Josifovska, Ultramicroscopy **53** 283 (1994).

[15] R. F. Egerton, Electron energy-loss spectroscopy in the electron microscope, 2nd ed. Plenum Press, New York, (1996).

[16] J. Spence, Acta Crystallographica Section A **49** 231 (1993).

[17] J. C. H. Spence and J. M. Zuo, Electron microdiffraction. Plenum Press, New York, (1992).

[18] P. Becker and P. Coppens, Acta Crystallographica Section A **46** 254 (1990).

[19] S. Miyake, Proc. Phys. Math. Soc. Japan **22** 666 (1940).

[20] J. Ibers, Acta Crystallographica **11** 178 (1958).

[21] L. Reimer, Transmission electron microscopy : physics of image formation and microanalysis, 4th ed. Springer, New York, (1997).

[22] P. A. Doyle and P. S. Turner, Acta Crystallographica Section A **24** 390 (1968).

[23] G. Radi, Acta Crystallographica Section A **26** 41 (1970).

[24] H. Bethe, Ann. Phys. **87** 55 (1928).

[25] F. M. Ross and W. M. Stobbs, Philosophical Magazine A **63** 37 (1991).

[26] M. Y. Kim, J. M. Zuo, and J. C. H. Spence, physica status solidi (a) **166** 445 (1998).

[27] M. Lehmann, Ultramicroscopy **100** 9 (2004).

[28] S. J. Pennycook, P. D. Nellist, Scanning Transmission Electron Microscopy Imaging and Analysis. Springer, New York, NY, (2011).

[29] P. Hartel, H. Rose, and C. Dinges, Ultramicroscopy **63** 93 (1996).

[30] D. B. Williams and C. B. Carter, Transmission electron microscopy : a textbook for materials science, 2nd ed. Springer, New York, (2009).

[31] C. C. Ahn, Transmission electron energy loss spectrometry in materials science and the EELS atlas, 2nd ed. Wiley, Weinheim, Germany, (2004).

[32] MultiPrep^{TM} operating manual of Allied High Tech Products, Inc.

CHAPTER 3

MEAN INNER POTENTIAL AND INELASTIC MEAN FREE PATH OF ZnO AND ZnTe

This chapter describes measurements of mean inner potential (MIP) and inelastic mean free path (IMFP) of ZnO nanowires (NWs) and ZnTe thin films. The ZnO NWs were grown using chemical vapor deposition (CVD) and were provided by Professor Hongbin Yu and his students at Arizona State University. The ZnTe thin films were grown by molecular beam epitaxy (MBE) and were provided by Professor Yong-Hang Zhang and his students at Arizona State University. My role in this work has included preparation of TEM samples, characterization of the material microstructure and measurement of the MIPs and IMFPs using off-axis electron holography.

3.1 MIP and IMFP of ZnO NWs.

3.1.1 Introduction

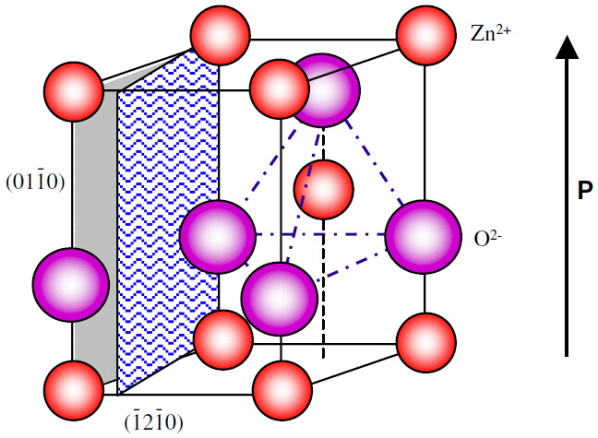

Figure 3.1 Schematic diagram of ZnO wurtzite structure, where the arrow indicates the [0001] direction [1].

ZnO is a II-VI semiconductor material, which has a direct band-gap energy of 3.37 eV and exciton binding energy of 60meV [1]. It has many possible applications due to its wide band gap, such as short wavelength (blue and ultraviolet) optoelectronic devices, while the high exciton binding energy ensures high efficiency in excitonic emission at room temperature [2]. Because it is transparent to visible light, ZnO can also be used as a transparent conductive oxide when it is heavily doped [1]. Moreover, ZnO has other potentially important applications such as solar cells, photocatalysts, piezoelectric devices, decontamination agents, surface acoustic wave devices and gas sensors [3-8].

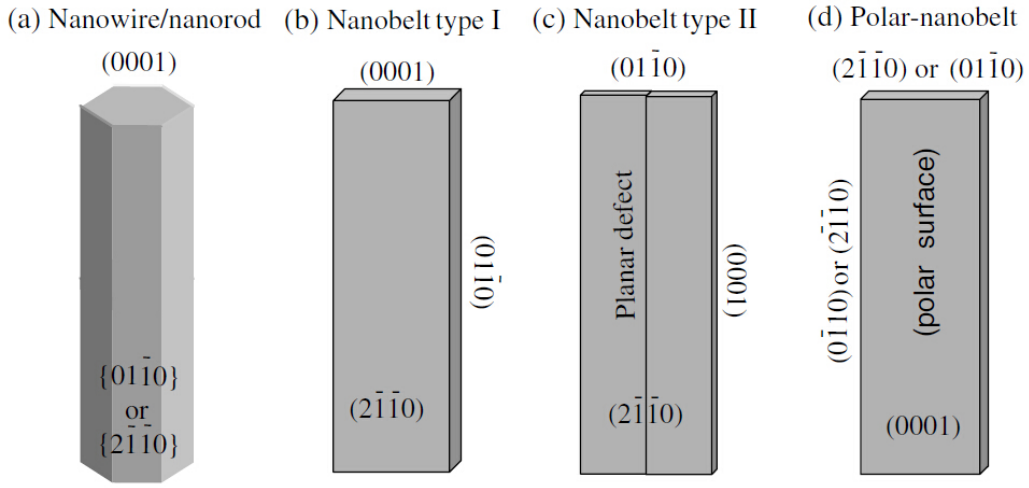

Figure 3.2 Schematic diagram of typical ZnO nanostructures [1].

ZnO usually has the wurtzite structure. It is hexagonal with a space group of C6mc and its lattice parameters are a=0.3296 nm and c=0.5207 nm [9]. A schematic diagram of the wurtzite ZnO structure is shown in Figure 3.1. Polarized surfaces will occur due to oppositely charged ions of Zn^{2+} and O^{2-} in the termination planes. Moreover, the tetrahedral structure will result in spontaneous polarization along the [0001]/c-axis as well as

piezoelectricity and pyroelectricity because of non-centrosymmetry [1]. The common directions for fast growth of ZnO include [2$\bar{1}\bar{1}$0], [01$\bar{1}$0] and ±[0001].

Typical ZnO nanostructures are illustrated in Figure 3.2 [1]. Different ZnO nanostructures have been achieved, such as nanowires (NWs), nanorods, nanotubes, nanobelts, nano-sheets, and nanostars [2,10-19]. Among these, the ZnO NWs and nano-sheets have received much interest because they have one/two dimensional structures, large surface-to-volume ratio and quantum confinement effects, which enable novel physical properties and applications [1,20]. Understanding the MIP and IMFP of ZnO is very important for further thickness and built-in potential measurements of ZnO nanostructures and semiconductors using off-axis electron holography [21]. In this research, conventional TEM was used to study the morphology of the ZnO NWs. Off-axis electron holography was then used to determine the MIP and IMFP of ZnO using ZnO NWs. Thickness measurements of ZnO thin sheets were performed using the measured MIP and IMFP values.

3.1.2 Experimental Details and Results

Samples for TEM characterization were prepared by sonicating the substrate with vertical ZnO NWs in isopropyl alcohol solution to dislodge NWs, followed by transferring the solution to TEM grids with lacey carbon supports using pipettes and then air-dried. Off-axis electron holography observations were done using the Philips-FEI CM200 operated at 200kV. In order to obtain larger fields of view, the normal objective lens was turned off, and the Lorentz mini-lens was used for imaging. The typical biprism voltage was 120V giving interference-fringe spacings of ~5 nm and the exposure time for hologram recording was normally 1 second.

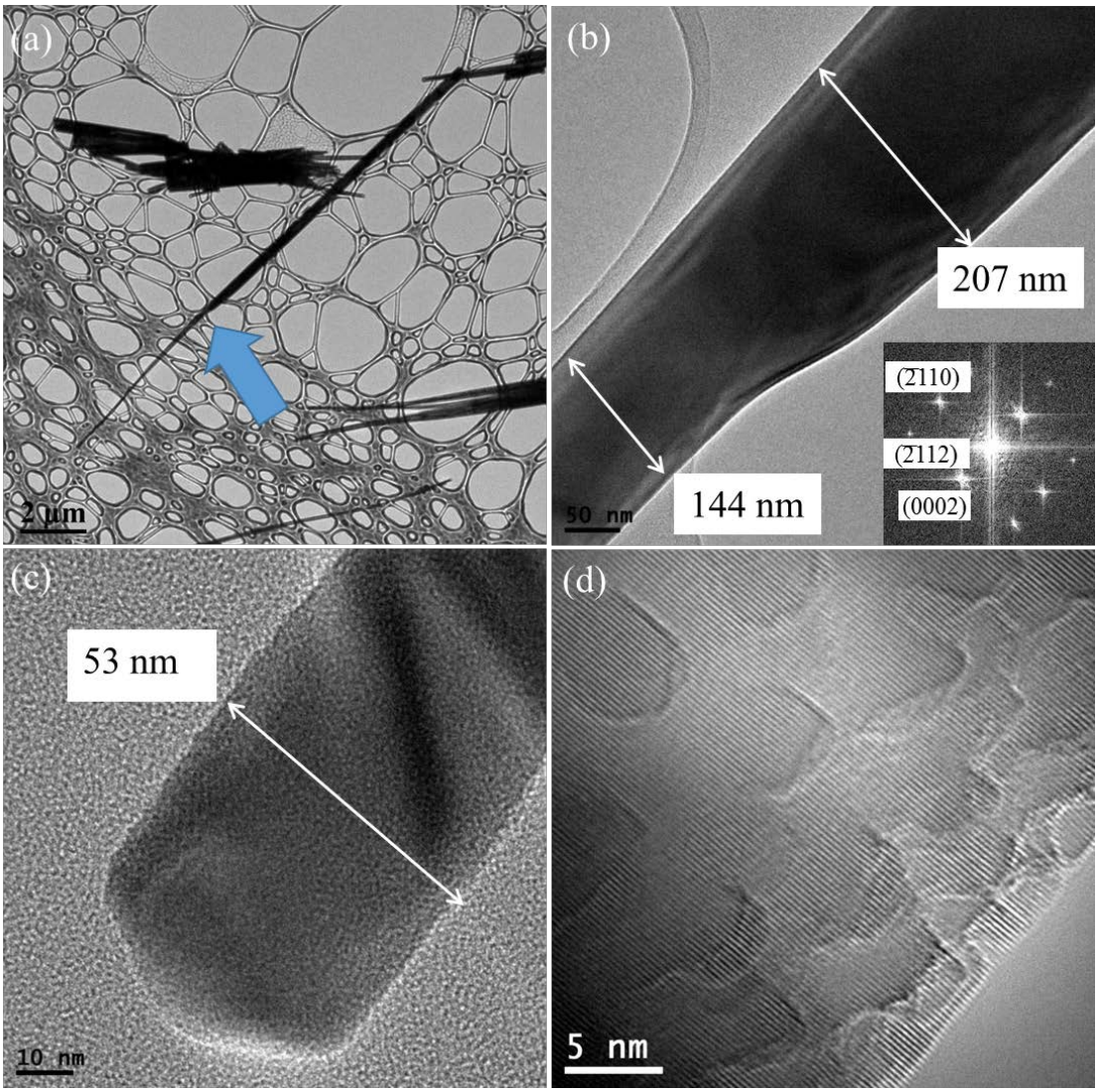

Figuare 3.3 TEM images of ZnO NWs: (a) Low-magnification TEM image of ZnO NW, where a transition in NW diameter is arrowed; (b) Enlargement showing the transition region; (c) TEM image showing the end of a ZnO NW; (d) TEM image of ZnO NW showing the effects of radiation damage due to the incident electron beam.

TEM images of a typical ZnO NW are shown in Figure 3.3. This NW is ~16.3 μm long and it has a tapered shape with a larger end of ~300 nm in diameter and a small end of ~53 nm in diameter. At ~5.5 μm from the end of the NW, the diameter changes quickly

from 207 nm to 144 nm, as shown in Figures 3.3a and 3.3b. The diffractogram in the insert of Figure 3.3b, taken from a high-resolution image (not shown) at the [01T0] zone axis, confirms that the ZnO NW has the wurtzite structure and that the growth direction is [0001]. Radiation damage during TEM observation due to the high-energy electron beam is observed at the thin region of the NW, as visible in Figure 3.3d.

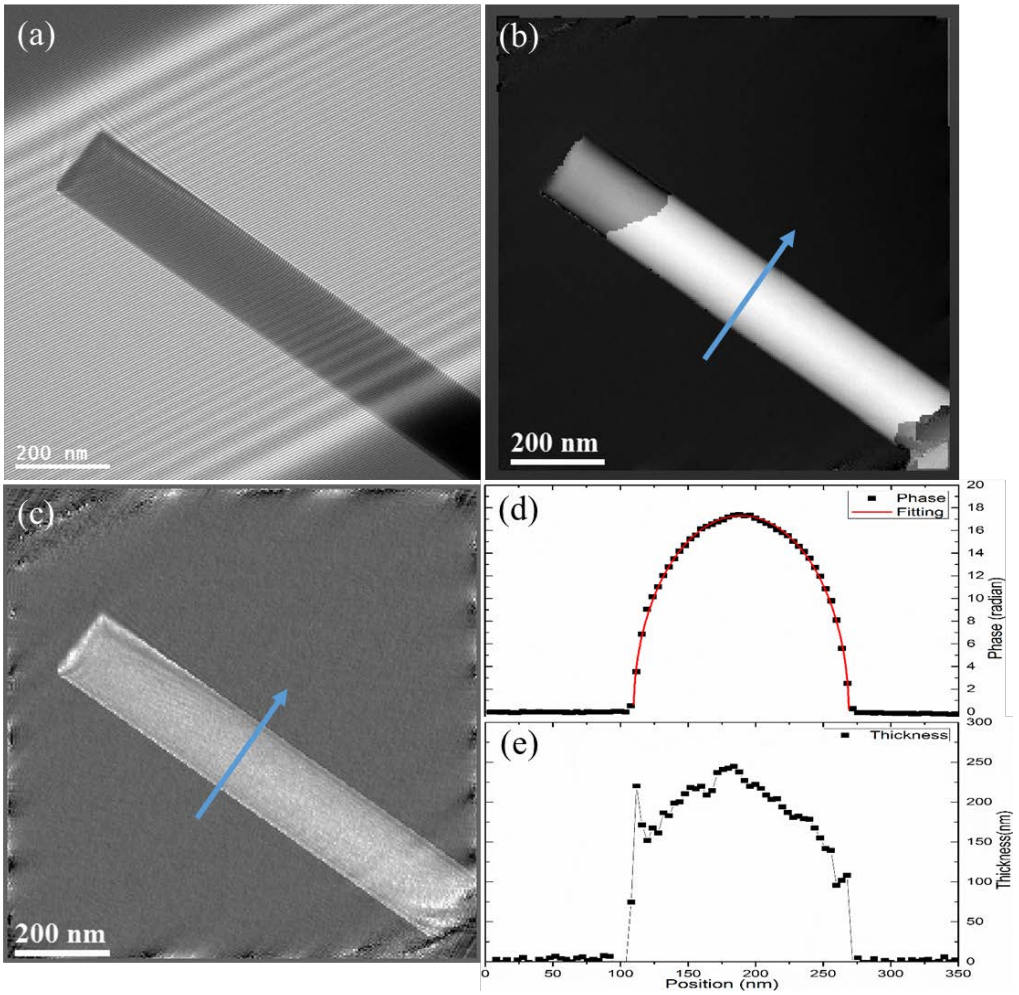

Figure 3.4 Holography study of ZnO NW: (a) Hologram of ZnO NW; (b) Reconstructed phase image of ZnO NW; (c) Reconstructed thickness image of ZnO NW, using IMFP of 85nm (for Si); (d) Line profile of phase along the blue arrow in (b) (black dots) and fitting result using cylindrical model (red line); (e) Thickness profile along the blue arrow in (c).

In order to extract information about the MIP and IMFP of ZnO, and to use these values to characterize the thicknesses of ZnO thin films, the ZnO NWs were used for measurement of the MIPs and IMFPs. A typical hologram of a ZnO NW is shown in Figure 3.4a. This NW has a diameter of ~157 nm and the tapered shape is not apparent here. The corresponding reconstructed phase and thickness images (initially using the IMFP of 85nm for Si) are shown in Figures 3.4b and 3.4c. Figure 3.4b indicates that there is a phase-unwrapping problem near the end of the NW, as shown by the grey contrast, compared to white contrast in the middle of NW, which is due to the abrupt change of thickness at the NW edge. Thus, the middle part of the phase image is used for MIP and IMFP measurement, since the phase from vacuum to the center of the NW is continuous and without any abrupt changes.

Phase and thickness profiles were extracted along the blue arrows indicated in Figures 3.4b and 3.4c, and these are shown in Figures 3.4d and 3.4e, respectively. From the phase profile, it appears that the NW has a projected cylindrical shape so that the NW width can be used as the projected thickness in Figure 3.4d, by comparing the experimental result with the fitting result using a cylindrical model. The peak values of phase (φ) and thickness (t) were measured from the line profiles in Figures 3.4d and 3.4e. The MIP V_0 and IMFP λ_i can then be calculated using the following equations:

$$V_0 = \frac{\varphi}{C_E * d} \tag{3.1}$$

$$\lambda_i = \frac{d * 85}{t} \tag{3.2}$$

where C_E=0.00728 rad/(V·nm) for 200 keV electrons and d is the diameter of the ZnO NW which is used as the projected thickness assuming a cylindrical shape.

The results from measurements of several ZnO NWs of different thicknesses are summarized in Table 3.1. The MIP and IMFP values for different thicknesses are also plotted in Figure 3.5, which indicates that the MIP and IMFP measurements are consistent as the thickness changes. Thus, the MIP for ZnO is determined to be 15.3±0.2 V and the IMFP is measured to be 55±3 nm, using the standard deviation as the error. Kruse *et al* have reported the MIP of 15.9±1.5V for ZnO measured using off-axis electron holography, which agrees with the results measured here [22].

Table 3.1 Measurement of Mean Inner Potential and Inelastic Mean Free Path of ZnO NWs.

	1	2	3	4	Average	Std. Dev.
V_0 (V)	15.5	15.2	15.1	15.2	15.3	0.2
λ_i (nm)	54	60	53	54	55	3

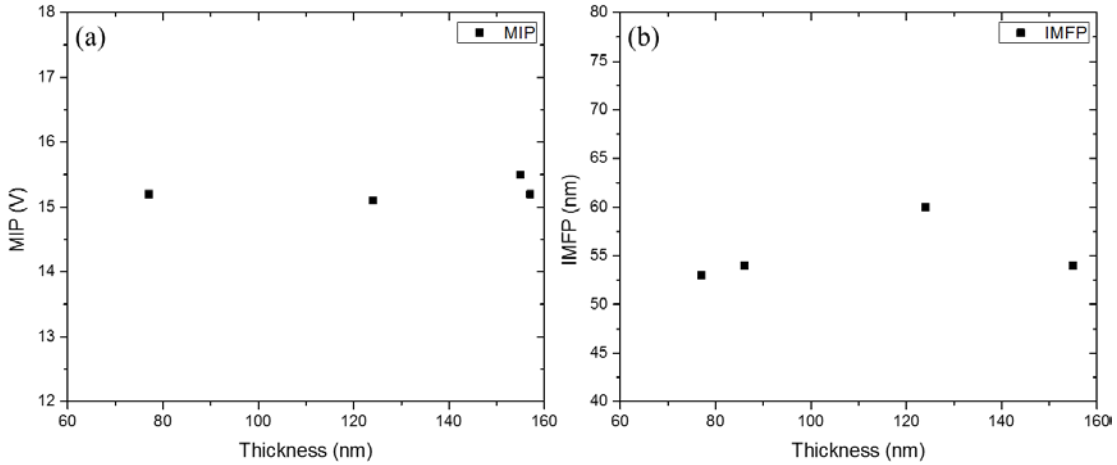

Figure 3.5 (a) MIP vs. thickness, and (b) IMFP vs. thickness, for ZnO NWs.

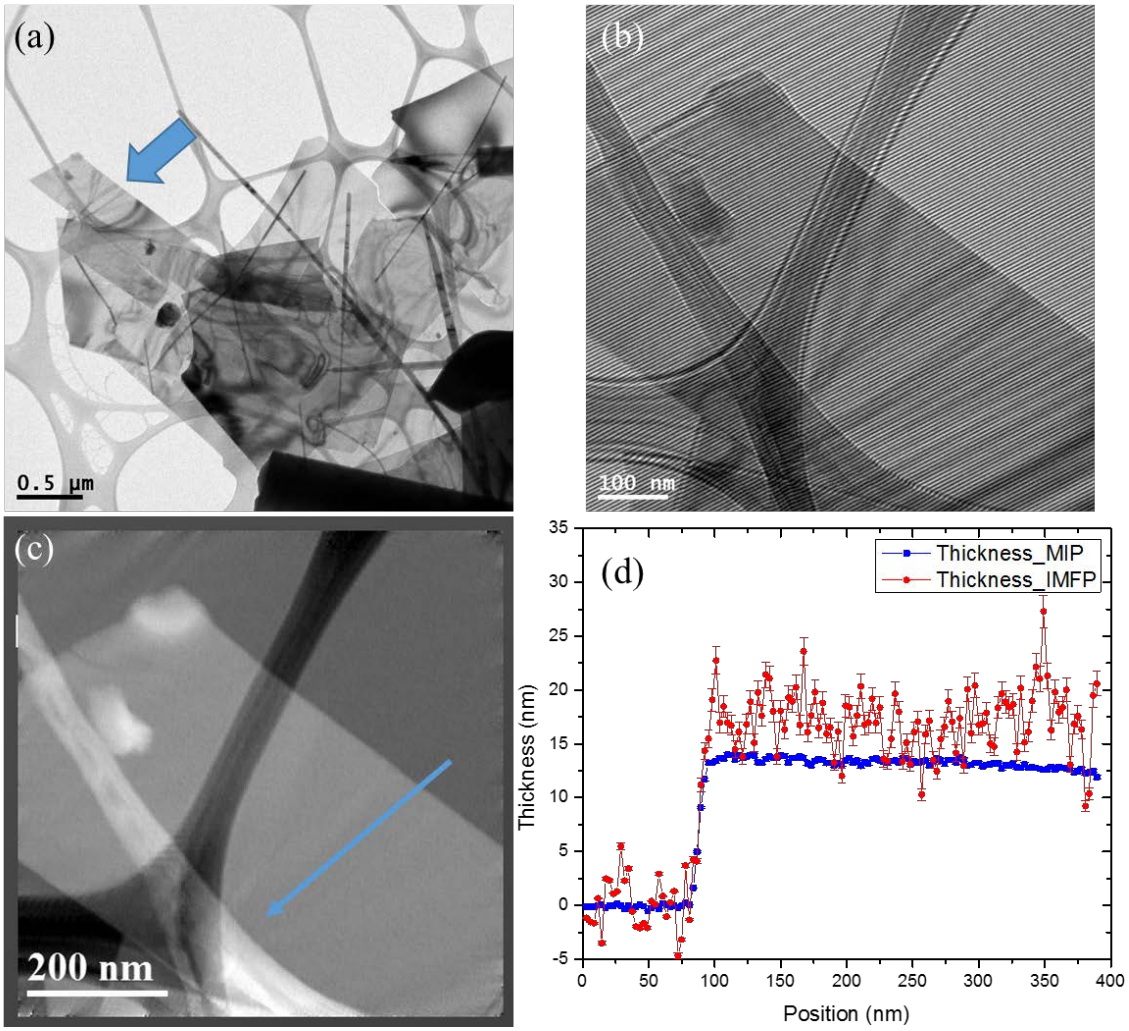

Figure 3.6 Holography of ZnO nano-sheet: (a) TEM image; (b) Hologram of ZnO nano-sheet; (c) Reconstructed phase image of ZnO nano-sheet; (d) Thickness profile with error bars measured using MIP (blue), and IMFP (red), respectively, along the blue arrow in (c).

TEM images of thin ZnO nano-sheets are shown in Figure 3.6a. These sheets are small and overlapping with each other, and bend contours are often visible (example arrowed). The transparency of the sheets indicates that these ZnO sheets are likely to be very thin. Because of the sheet overlap and bending, it was difficult to tilt the sample to a specific desired orientation for high-resolution imaging and CBED thickness measurement.

The sample was tilted to avoid diffraction contrast, and off-axis electron holography was instead used to measure the sheet thickness. The blue arrow in Figure 3.6a indicates the thin sheet used for the holography experiment.

The hologram of the ZnO nano-sheet and its reconstructed phase image are shown in Figures 3.6b and 3.6c, respectively. The thickness image (not shown) was calculated from the reconstructed amplitude image (not shown), using the IMFP of 55 nm obtained from the ZnO NW measurements. The bend contours near the blue arrow in Figure 3.6a are visible in the hologram (black contrast) as well as the phase image (white contrast), and could introduce some diffraction contribution to the reconstructed phase and thickness images. Thus, the phase and thickness profiles were extracted from the phase image and thickness images, respectively, along the blue arrow in Figure 3.6c, where the bend contrast is minimal. The thickness profiles of the ZnO nano-sheet along the blue arrow in Figure 3.6c, as calculated from the phase profile (blue line), and from the thickness profile (red line), respectively, are shown in Figure 3.6d. The thickness profile calculated using the IMFP tends to be noisier, compared to the one calculated using the MIP, because the thickness image is measured from the image intensity, whereas the phase image is measured from the shift of interference fringes and the intensity might be influenced by other effects, such as Fresnel fringes as well as uniformity and stability of beam intensity.

The thickness profile extracted from the thickness image gives a thickness of ~18±3nm, as measured from the region of 125nm-175nm in Figure 3.6d, and using the combination of the standard deviation (2nm) in this region and the 6% error in λ_i measurement (1nm) as the thickness measurement error.

An alternative approach for thickness measurement is to use the phase profile extracted from the reconstructed phase image and the MIP value of 15.3 V obtained from the ZnO NW measurement, using the equation:

$$t = \frac{\varphi}{C_E * V_0} \tag{3.3}$$

where C_E=0.00728 rad/(V·nm) for 200keV electrons, φ is the phase and V_0 is the MIP.

Using the MIP approach gives the ZnO sheet thickness of ~14±1nm, as measured over the range of 125nm-175nm in Figure 3.6d and using the combination of the standard deviation (0.3nm) in this region and 2% error in V_0 measurement (0.3nm) as the thickness measurement error. In contrast, the IMFP method gave a value of ~18±3nm. Thus, the two methods give consistent results. The 4nm difference between the MIP and IMFP measurements reflect some of the inherent inaccuracies in the MIP and IMFP measurements using ZnO NWs, which includes an assumption of cylindrical shape NWs, limited MIP and IMFP measurement points, possible diffraction contrast and limited spatial resolution in the reconstructed image (~4nm). More MIP and IMFP measurements could reduce this inaccuracy. It is also possible that diffraction contrast is affecting the thickness measurement because the nano-sheet orientation was changing during observation.

3.1.3 Conclusions

Using off-axis electron holography and ZnO NWs, the MIP of ZnO was measured to be 15.3±0.2 V, and the IMFP at 200keV was measured to be 55±3 nm. The MIP and IMFP values were then used to characterize the thickness of a ZnO nano-sheet and gave consistent results for thickness measurement in the range of 14nm-18nm. With knowledge of the MIP and IMFP, it should become possible to extract the built-in potential in doped ZnO

semiconductor devices. However, this task is beyond the immediate scope of this dissertation research.

3.2 MIP and IMFP Measurement of ZnTe

3.2.1 Introduction

ZnTe is a II-VI semiconductor, which has the zincblende structure, as shown in Figure 3.7, with a lattice parameter of 6.103 Å. ZnTe has important applications for optoelectronic devices such as light-emitting devices, detectors and solar cells [23]. It has a direct band gap of 2.26eV at room temperature, which is in the energy range of visible light [24]. However, it is difficult to achieve *n*-type ZnTe because of compensation effects in thermal equilibrium, and native defects of opposite type will tend to form to compensate the dopant impurity [25-27]. Various techniques have been tried to achieve *n*-type ZnTe, such as molecular beam epitaxy and metal-organic chemical vapor deposition under non-equilibrium conditions, with thermal diffusion and annealing treatment [24,28-30].

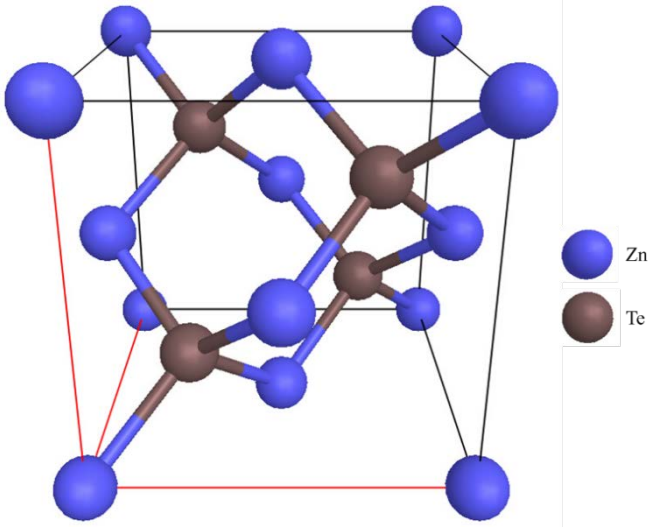

Figure 3.7 Schematic diagram of zincblende structure ZnTe.

In order to improve device performance, it is desirable to understand the electrostatic properties, such as the built-in potential and active dopant concentrations. However, it is first necessary to determine the MIP and IMFP of ZnTe in order to extract the built-in potential information using electron holography. In this research, off-axis electron holography was used to determine the MIP and IMFP of ZnTe thin films.

3.2.2 Experiment Details and Results

Samples for TEM characterization were prepared using the Multi Prep^{TM} wedge polisher. A wedge-shaped sample was achieved by mechanical polishing, followed by a brief period of argon-ion-milling to clean residue from the sample surface. Off-axis electron holography observations were done using the Philips-FEI CM200 operated at 200kV. In order to obtain a larger field of view, the normal objective lens was turned off, and the Lorentz mini-lens was used for imaging. The typical biprism voltage was 120V and the exposure time for hologram recording was 1 second. The technique of convergent beam electron diffraction (CBED) was used to determine the local sample thickness using comparison with image simulations. The Bloch wave method was used to simulate dynamic effects that could impact the phase measurements [31].

The intrinsic ZnTe sample was tilted to the [100] zone axis and CBED patterns were recorded at different positions in the normal imaging mode. Beam damage as well as beam-induced carbon contamination were caused by the high-energy electrons. These beam-damaged regions with carbon contamination were later used was position markers for the holography experiments. After the CBED observations, the sample was tilted slightly off the zone axis to minimize diffraction contrast. The objective lens was then switched off and the Lorentz mini-lens was used to obtain larger fields of view. Holograms were taken

close to the different position markers to extract phase and amplitude information at these locations for the MIP and IMFP measurements.

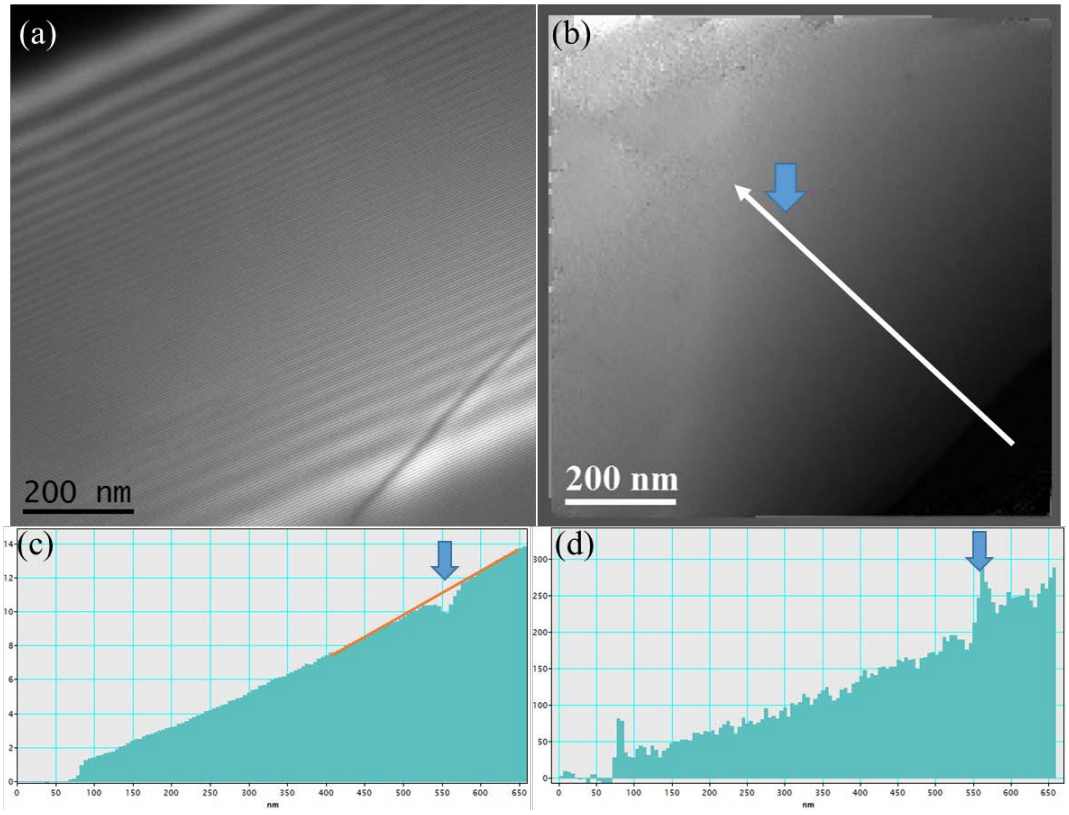

Figure 3.8 Holography of intrinsic ZnTe thin film: (a) Hologram of ZnTe thin film; (b) Reconstructed phase image of ZnTe thin film, with blue arrow showing the position used for recording CBED pattern; (c) Phase profile extracted along the white arrow in (b); (d) Thickness profile extracted from processed thickness image at the same positions as the white arrow in (b), calculated here using the IMFP of 85nm for Si.

Figures 3.8a and 3.8b show the original hologram and the reconstructed phase image, respectively, at a typical marker position (indicated by blue arrow), where the CBED pattern was previously taken. Phase and thickness profiles (using IMFP of 85nm for Si)

were extracted along the white arrow in Figure 3.8b, and are shown in Figures 3.8c and 3.8d, respectively. In Figure 3.8c, the position of the CBED probe can be identified by the small dip at the position of the blue arrow. Linear fit from the surrounding area was used to compensate for the effect of beam damage, and the phase φ was extracted from the fitting result at the position of the center of the dip, as shown by the orange line in Figure 3.8c. The marker position of the CBED can also be identified in the thickness profile in Figure 3.8d, where the thickness suddenly reduced at 550nm, and then increased at the blue arrow position, which is most likely due to carbon contamination.

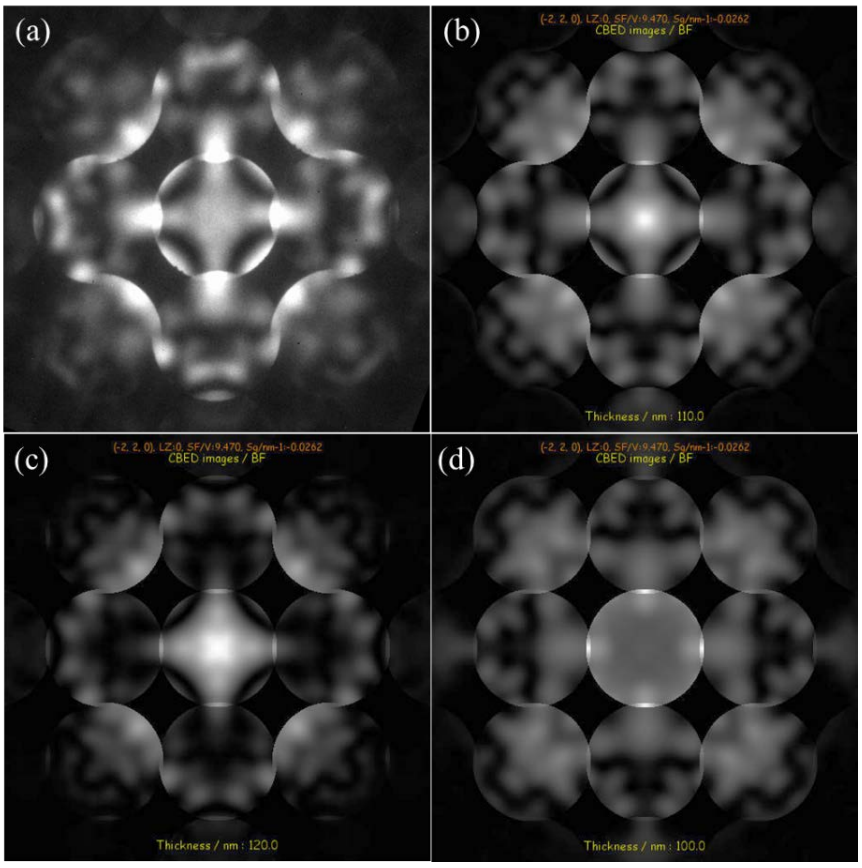

Figure 3.9 CBED patterns for ZnTe: (a) Experimental CBED pattern; (b) Simulated CBED pattern for thickness of 110nm; (c) Simulated CBED pattern for thickness of 120nm; (d) Simulated CBED pattern for thickness of 100nm.

The CBED pattern taken at this position is shown in Figure 3.9a. CBED patterns for different crystal thicknesses were simulated using the Bloch wave method and the JEMS simulation program, as shown in Figures 3.9b to 3.9d. Careful comparison between the experimental CBED pattern and the simulated CBED patterns shows that the sample thickness t_C at the dip position is ~110nm. The thickness t_h in the holography experiment can then be calculated to compensate for sample tilting.

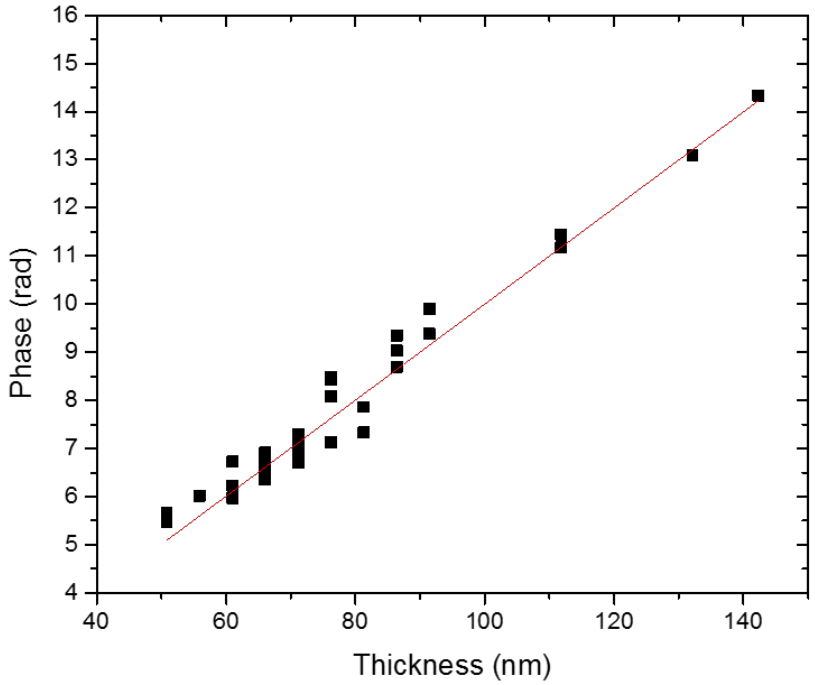

Figure 3.10 Phase at CBED positions as a function of the ZnTe thickness as estimated from the CBED pattern.

Table 3.2 Linear fitting results from Figure 3.10.

	Value	Std. Dev.
Slope (rad/nm)	0.09981	0.00403
Intercept (rad)	0.01945	0.45093

This procedure was repeated for different CBED marker positions. The overall measured phase φ at the dips as a function of thickness t_h is shown in Figure 3.10. A linear fit is applied to the data and the fitting results are shown in table 3.2. The values of V_0 and ΔV_0 can be calculated from the slope and the standard deviation. Thus, the MIP for ZnTe is measured to be 13.7±0.6V.

To check this experimental result, MIP calculations were performed using Equations 2.16 and 2.18. The atomic scattering amplitudes for forward scattering, according to Doyle and Turner, are given by $f_{Zn}(0) = 6.605\text{Å}, f_{Sb}(0) = 10.974\text{Å}, f_I(0) = 10.905\text{Å}$ [32]. The scattering amplitude for Te is calculated as the average of Sb and I: $f_{Te}(0) = \frac{f_{Sb}(0)+f_I(0)}{2} = 10.939$ Å. The lattice parameter for ZnTe is 6.104Å. Therefore, the MIP calculated using Equation 2.17 and the non-binding model is V_{DT}=14.3V. The binding effect can be included using Equation 2.18 and the MIP is calculated to be V_{Radi}=10.4V. The non-binding model serves as the upper limit, while the Radi model serves as the lower limit. The experimental measurement of 13.7V is within the upper and lower limits. Moreover, Schowalter *et al* have previously calculated the MIP of ZnTe by first-principles' methods with local density approximation (LDA) and generalized gradient approximation (GGA) for exchange and correlation part of potential. They obtained V_0 values for ZnTe of 13.77V using LDA and 13.82V using GGA [33]. Thus, the MIP measured using CBED and off-axis electron holography matches well with these calculations.

Once the V_0 of ZnTe was determined to be 13.7±0.6V, this value was used to estimate the IMFP of ZnTe. In the previous V_0 measurements, both phase and thickness profiles (using IMFP of 85nm for Si) were extracted at the same positions. The actual thickness profile t_{MIP} can be calculated using V_0 and Equation 3.3. To determine the IMFP λ_i for

ZnTe, the thickness profile t_{IMFP} measured by using λ_i was compared with the actual one calculated using MIP and Equation 3.3. The λ_i was changed systematically until $(t_{MIP}-t_{IMFP})^2$ reached the minimum for the part of the profile away from the CBED position. This λ_i is then the actual IMFP for ZnTe. All of the measured λ_i are summarized in Figure 3.11. The average for λ_i is 46nm and the standard deviation is 2nm. Therefore, the IMFP for ZnTe is determined to be λ_i=46±2nm for 200keV electrons.

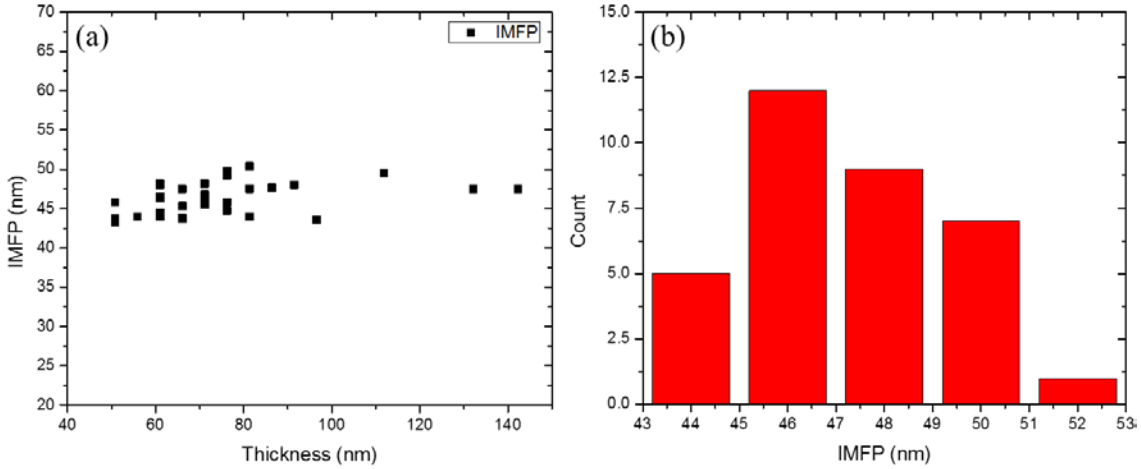

Figure 3.11 IMFP of ZnTe: (a) IMFP shown as a function of CBED thickness; (b) Frequency count of measured IMFPs.

Figure 3.12a shows a TEM cross section image of an Al-doped ZnTe thin film grown on GaSb substrate, which is prepared by using the Multi Prep™ wedge polisher. The 1.5-µm ZnTe thin film was *p*-type doped (using nitrogen) with the nominal concentration of ~10^{18} cm^{-3}. An Al layer was deposited on the surface of ZnTe, and Al was then diffused into ZnTe as *n*-type dopant by heating up to 420˚C in order to form a *pn* junction in the ZnTe layer. Many dislocations were present in the ZnTe thin film, as visible in Figure 3.12a.

The sample was tilted parallel to the ZnTe/GaSb interface to minimize diffraction contrast caused by the dislocations and to keep the interfaces sharp in the electron-beam projection.

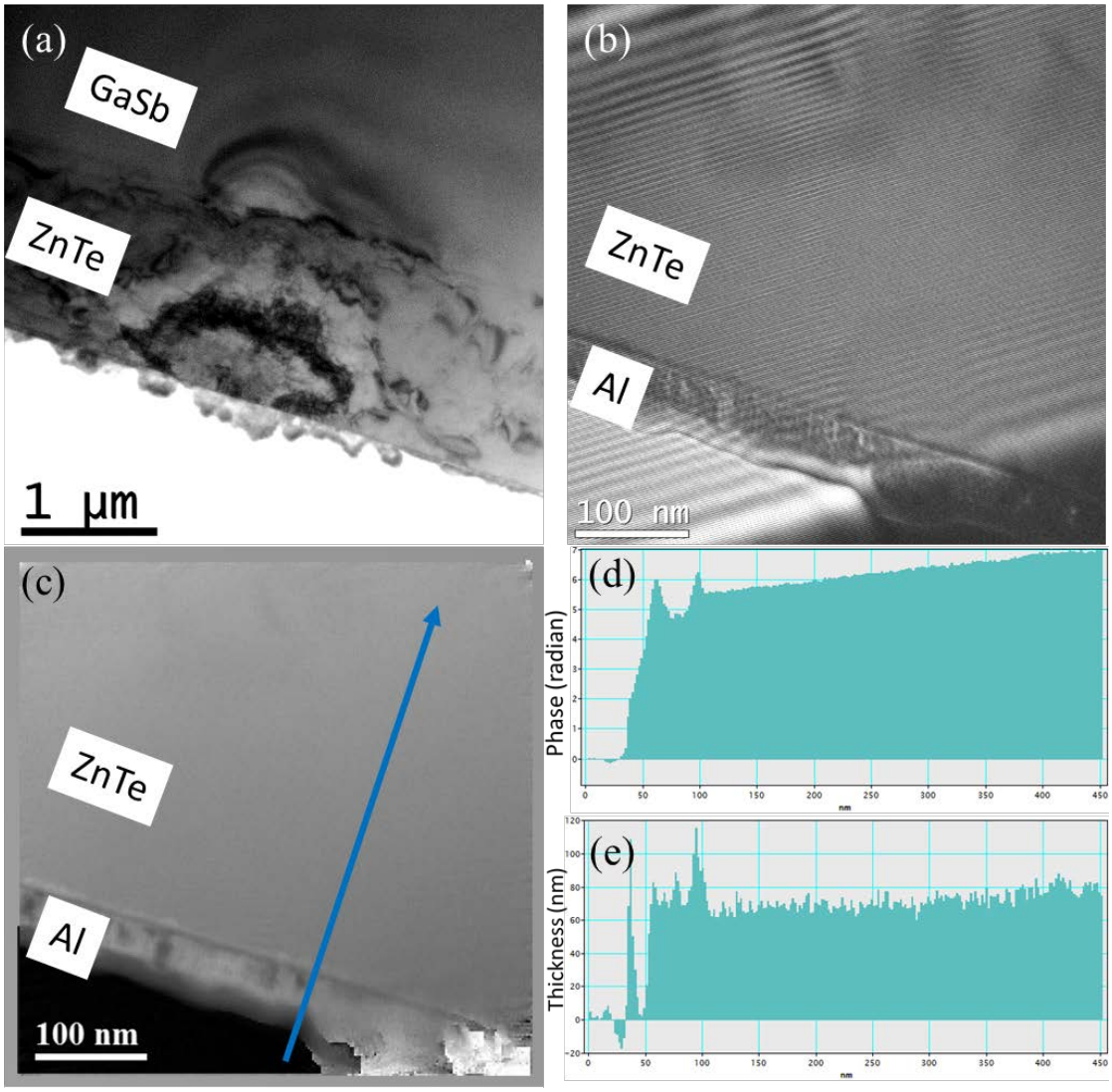

Figure 3.12 Holography of Al-doped ZnTe thin film with supposed *pn* junction: (a) TEM image of ZnTe thin film on GaSb substrate; (b) Hologram of ZnTe thin film; (c) Reconstructed phase image of ZnTe; (d) and (e) Phase and thickness profiles, respectively, along blue arrow in (c).

Figures 3.12b and 3.12c show the hologram and the corresponding reconstructed phase image, respectively. Phase and thickness profiles were extracted along the blue arrow in Figure 3.12c. The phase and thickness profiles show similar linear changes from the ZnTe surface towards the ZnTe/GaSb interface. However, no abrupt change of phase possibly caused by built-in potential across any *pn* junction can be observed in the phase profile. The reasons for the absence of a built-in potential are not clear, but might be due to several possible causes, including: (a) Al dopants are not activated during the diffusion process; or (b) the *pn* junction is much deeper within the ZnTe layer than anticipated, and cannot be imaged by holography because of the restricted field of view.

3.2.3 Simulation of Dynamical Effects

In the MIP measurement, only the zero term of Fourier transform of crystal potential is considered, which corresponds to the forward transmitted [000] beam [32]. However, it is difficult to maintain kinematical conditions due to dynamical scattering from the diffracted beams, and non-zero terms of the Fourier transform of the crystal potential contribute to the forward transmitted beam [34,35]. Therefore, the sample is usually tilted away from the zone axis to minimize diffraction conditions when performing holography experiments [21]. It is helpful to study the dynamical effects as a function of sample thickness and tilting to provide guidance for these experiments.

Calculations of the dynamical effects for ZnTe were done using the many-beam Bloch wave simulation program Mbfit developed by Tsuda [31]. During the simulations, the real φ_{re} and imaginary part φ_{im} of the [000] forward transmitted beam were recorded as a function of different incident beam orientations. The phase of the [000] beam was calculated using the equation below:

$$phase = \arctan(\frac{\varphi_{im}}{\varphi_{re}}) \tag{3.4}$$

The simulation does not include the zero term of the Fourier transform of crystal potential (MIP) so that only the dynamical effects from the diffracted beams are included.

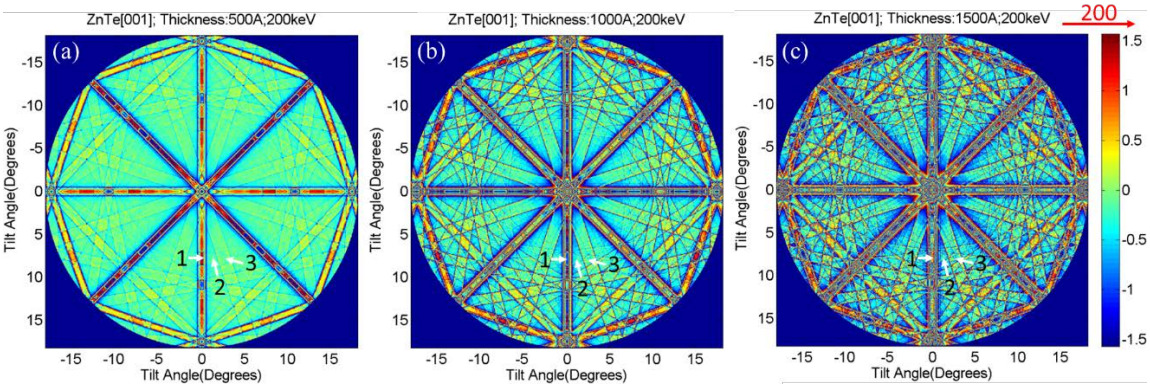

Figure 3.13 Simulation of dynamical effects at different ZnTe thicknesses. The electron beam energy is 200keV, the zone axis is [001], the tilting direction is shown by the red arrow, and the phase scale bar in the unit of radian is shown on the right. (a) 50nm; (b) 100nm; (c) 150nm.

Table 3.3 Dynamical effects for ZnTe near [001] zone axis with different thicknesses.

(Positions shown in Figure 3.13)

Positions	50nm	100nm	150nm
MIP	5.0 radian	10.0 radian	15.0 radian
1: (0.0˚, 7.9˚)	1.43 radian	-1.102 radian	0.51 radian
2: (1.3˚, 7.9˚)	-0.08 radian	-0.123 radian	-0.19 radian
3: (2.5˚,7.7˚)	-0.16 radian	-0.5678 radian	-1.21 radian

It is obvious and expected that the phase of the [000] beam changes as the direction of the incident beam changes, as shown in Figure 3.13. To illustrate how the sample tilting and thickness contribute to dynamical effects, three positions were chosen for each of the thicknesses: (1) (0˚, 7.9˚) is in a major Kikuchi band, (2) (1.3˚, 7.9˚) is off the zone and Kikuchi band and (3) (2.5˚, 7.7˚) is in a minor Kikuchi band. The results are shown in Table 3.3 and the phase shift solely due to MIP for 200keV electrons are also shown in the row labeled MIP. When the beam is close to the zone axis or to Kikuchi bands, the dynamical effects become more important, as shown at position (1), where the phase due to dynamical effect fluctuates from 1.4 to 0.5 radian, as the thickness changes from 50 nm to 150 nm and this effect is ~30% of the phase due to MIP at the thickness of 50nm. However, at position (2), the phase only changes from -0.1 to -0.2 radian and its effect only takes ~2%. Thus, it is usually necessary in holography experiments to tilt the sample away from the zone axis and also to avoid major Kikuchi bands. The sample thickness increases from Figure 3.13a to 3.13b and the dynamical effects become more obvious, by comparing the results at position (3) for different thicknesses. Thus, the sample must be tilted to a low diffraction contrast condition, when the sample is thick.

In Figure 3.14, the dynamical effects were simulated and compared for different zone axes, while the other parameters were kept constant. These results indicate that the [111] and [011] zone axes have more dynamical effects, compared to [001] axis. The area with small phase change, such as in the range of -0.5 to 0.5 radian, is larger for the [001] zone axis, compared to the other two cases. Choosing a low symmetry zone axis will obviously reduce the diffraction scattering.

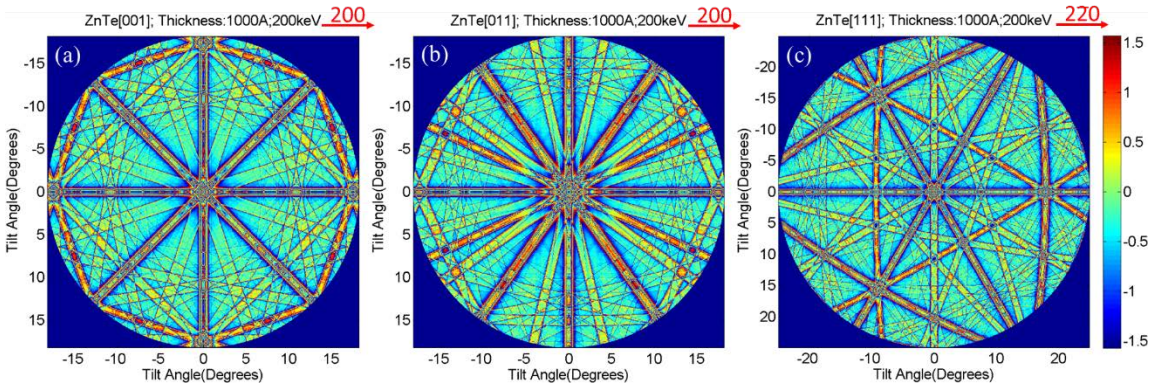

Figure 3.14 Simulation of dynamical effects for ZnTe at different zone axes. The electron beam energy is 200keV, the thickness is 100nm, the tilting directions are shown by red arrows and the color scale bar in the unit of radian is shown on the right. (a) [001]; (b) [011]; (c) [111].

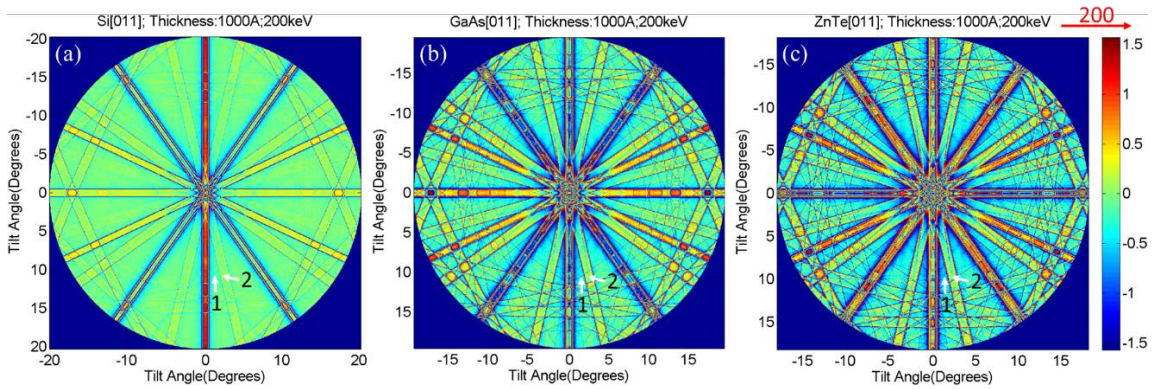

Figure 3.15 Simulation of dynamical effects in different materials. The electron beam energy is 200keV, the thickness is 100nm, the zone axis is [011], the tilting direction is shown by the red arrow and the color scale bar in the unit of radian is shown on the right. (a) Si; (b) GaAs; (c) ZnTe.

Table 3.4 Measurement of dynamical effects for different materials at [011] zone axis.

(Positions shown in Figure 3.15)

Positions	Si	GaAs	ZnTe
MIP	8.8 radian	10.2 radian	10.0 radian
1: (1.6˚, 11.0˚)	-0.16 radian	0.19 radian	-0.43 radian
2: (2.7˚, 11.0˚)	-0.02 radian	0.08 radian	-0.04 radian

The dynamical effects were simulated and compared for several different crystalline materials in the [011] projection, while the other parameters were kept constant. Values taken off the zone and the Kikuchi band (Position 1), and at a minor Kikuchi band (Position 2), are shown in Table 3.4. The dynamical effects at these positions are still low and ~4% of the phase due to MIP only. However, the phase change across the Kikuchi bands become more visible when changing from Si to ZnTe, which indicates that the dynamical effects become more important for heavier material. These results confirm that the dynamical effects increase as the average atomic number increases. Therefore, for higher Z materials, such as ZnTe, it is necessary to examine thinner areas to reduce diffraction effects.

3.2.4 Conclusions

The MIP of ZnTe was measured to be V_0=13.7±0.6 V and the IMFP for 200keV electron beam was measured to be λ_i=46±2 nm, using CBED and off-axis electron holography. The measured MIP and IMFP were then used to investigate a ZnTe thin film expected to have a *pn* junction. However, no change in signal due to built-in potential across a junction was observed. The reasons might be: (a) Al dopants were not activated; (b) the junction was beyond the field of view of the holography experiment. Dynamical

effects were systematically studied by using Bloch wave simulations. Choosing thinner samples, avoiding low-index zone axes and careful tilting will all help to minimize dynamical effects.

References

[1] Z. L. Wang, Journal of Physics: Condensed Matter **16** R829 (2004).

[2] M. H. Huang, S. Mao, H. Feick, H. Yan, Y. Wu, H. Kind, E. Weber, R. Russo, and P. Yang, Science **292** 1897 (2001).

[3] B. Pal and M. Sharon, Mater Chem Phys **76** 82 (2002).

[4] C. J. Lee, T. J. Lee, S. C. Lyu, Y. Zhang, H. Ruh, and H. J. Lee, Applied Physics Letters **81** 3648 (2002).

[5] N. Ohashi, K. Kataoka, T. Ohgaki, T. Miyagi, H. Haneda, and K. Morinaga, Applied Physics Letters **83** 4857 (2003).

[6] G. Sberveglieri, S. Groppelli, P. Nelli, A. Tintinelli, and G. Giunta, Sensors and Actuators B: Chemical **25** 588 (1995).

[7] S. Baosheng, Y. Akira, and K. Makoto, Japanese Journal of Applied Physics **37** L206 (1998).

[8] J. J. Lee, Y. B. Kim, and Y. S. Yoon, Applied Surface Science **244** 365 (2005).

[9] U. Özgür, Y. I. Alivov, C. Liu, A. Teke, M. A. Reshchikov, S. Doğan, V. Avrutin, S. J. Cho, and H. Morkoç, Journal of Applied Physics **98** 041301 (2005).

[10] Y. Li, G. W. Meng, L. D. Zhang, and F. Phillipp, Applied Physics Letters **76** 2011 (2000).

[11] Y. C. Kong, D. P. Yu, B. Zhang, W. Fang, and S. Q. Feng, Applied Physics Letters **78** 407 (2001).

[12] J.-J. Wu, S.-C. Liu, C.-T. Wu, K.-H. Chen, and L.-C. Chen, Applied Physics Letters **81** 1312 (2002).

[13] Z. W. Pan, Z. R. Dai, and Z. L. Wang, Science **291** 1947 (2001).

[14] X. Y. Kong, Y. Ding, R. Yang, and Z. L. Wang, Science **303** 1348 (2004).

[15] A. Sekar, S. H. Kim, A. Umar, and Y. B. Hahn, Journal of Crystal Growth **277** 471 (2005).

[16] A. Umar, S. H. Kim, Y. S. Lee, K. S. Nahm, and Y. B. Hahn, Journal of Crystal Growth **282** 131 (2005).

[17] B. P. Zhang, N. T. Binh, K. Wakatsuki, Y. Segawa, Y. Yamada, N. Usami, M. Kawasaki, and H. Koinuma, Applied Physics Letters **84** 4098 (2004).

[18] A. Umar, S. Lee, Y. S. Lee, K. S. Nahm, and Y. B. Hahn, Journal of Crystal Growth **277** 479 (2005).

[19] J. Q. Hu, Y. Bando, J. H. Zhan, Y. B. Li, and T. Sekiguchi, Applied Physics Letters **83** 4414 (2003).

[20] A. Umar and Y. B. Hahn, Nanotechnology **17** 2174 (2006).

[21] M. R. McCartney, N. Agarwal, S. Chung, D. A. Cullen, M.-G. Han, K. He, L. Li, H. Wang, L. Zhou, and D. J. Smith, Ultramicroscopy **110** 375 (2010).

[22] E. Müller, P. Kruse, D. Gerthsen, M. Schowalter, A. Rosenauer, D. Lamoen, R. Kling, and A. Waag, Applied Physics Letters **86** 154108 (2005).

[23] T. Tanaka, Q. Guo, M. Nishio, and H. Ogawa, Journal of Physics: Conference Series **61** 1162 (2007).

[24] K. Sato, M. Hanafusa, A. Noda, A. Arakawa, M. Uchida, T. Asahi, and O. Oda, Journal of Crystal Growth **214–215** 1080 (2000).

[25] G. Mandel, Physical Review **134** A1073 (1964).

[26] T. Teiji, M. Toyosaka, and T. Kiyoshi, Japanese Journal of Applied Physics **11** 1024 (1972).

[27] W. D. Callister, T. L. Larsen, C. F. Varotto, and D. A. Stevenson, Journal of Physics and Chemistry of Solids **33** 1433 (1972).

[28] O. Hiroshi, I. Gheyas Syed, N. Hitoshi, N. Mitsuhiro, and Y. Akira, Japanese Journal of Applied Physics **33** L980 (1994).

[29] I. W. Tao, M. Jurkovic, and W. I. Wang, Applied Physics Letters **64** 1848 (1994).

[30] T. Tanaka, K. Hayashida, K. Saito, M. Nishio, Q. Guo, and H. Ogawa, physica status solidi (b) **243** 959 (2006).

[31] J. C. H. Spence and J. M. Zuo, Electron microdiffraction. Plenum Press, New York, (1992).

[32] M. Gajdardziska-Josifovska and A. H. Carim, Chapter 12, Introduction to electron holography, Kluwer Academic/Plenum Publishers, New York, (1999).

[33] M. Schowalter, D. Lamoen, A. Rosenauer, P. Kruse, and D. Gerthsen, Applied Physics Letters **85** 4938 (2004).

[34] A. Lubk, D. Wolf, and H. Lichte, Ultramicroscopy **110** 438 (2010).

[35] M. Gajdardziska-Josifovska, M. R. McCartney, W. J. de Ruijter, D. J. Smith, J. K. Weiss, and J. M. Zuo, Ultramicroscopy **50** 285 (1993).

CHAPTER 4

MAPPING ELECTROSTATIC PROFILES ACROSS AXIAL *p*-*n* JUNCTIONS IN Si NANOWIRES USING OFF-AXIS ELECTRON HOLOGRAPHY

This chapter describes the measurement of electrostatic and built-in potential profiles across axial *p*-*n* and Schottky junctions in Si nanowires (NWs). The Si NWs were grown using the vapor-liquid-solid method, and were provided by Daniel Perea from Pacific Northwest National Laboratory and Tom Picraux from Los Alamos National Laboratory. My role in this work included preparation of samples for TEM characterization of the NW structures, measurements of electrostatic and built-in potential profiles across the axial *p*-*n* and Schottky junctions in the NWs using off-axis electron holography, and device simulations for determination of active dopants. The major results in this study have been published [1].

4.1 Introduction

Silicon nanowires (NWs) have electrical transport properties that are considerably different from those of bulk material due to their one-dimensional structure [2]. Control of the dopant profiles in the Si NWs enable promising applications for nanoscale electronic devices, such as sensors [3] and field-effect transistors [4]. To improve the performance of these devices, where theories for bulk materials are likely to fail, it is necessary to understand their unique charge transport mechanisms. In particular, the active dopant location, concentration and spatial distribution in the NWs play a critical role [2].

Different experimental techniques have been used to characterize NW composition, such as transmission electron microscopy (TEM), scanning TEM (STEM) [5], secondary ion mass spectroscopy [6], and atom probe tomography [7]. However, it is difficult to make direct measurements of the active dopant distribution and resultant electronic properties within NWs because of their nanoscale dimensions. In addition, multiple junctions in real devices can further complicate measurements. The technique of off-axis electron holography provides an effective approach to quantitatively map electrostatic fields with nanoscale spatial resolution, without the need for micro-fabricated electrical contacts [8,9]. In addition, the technique has recently been used to characterize the electrical properties of different NWs [10-12].

Off-axis electron holography is a TEM-based interferometric technique [8,9]. In cases where magnetic field is absent, and cylindrical NW shape as well as uniform distribution in the NW cross section are assumed, the phase shift due to the sample can be described by:

$$\Delta\varphi(x,y) = C_E \times (V_0(x,y,z) + V_{bi}(x,y,z)) \times \mathrm{t} \tag{4.1}$$

where C_E is an electron-energy-dependent interaction constant with the value of 0.00728 rad V^{-1} nm^{-1} for 200-keV electrons, V_0 is the mean inner potential (MIP) of the sample, V_{bi} is the built-in potential and t is the diameter of NW served as the projected thickness.

In the case of a single *p-n* junction without bias, the built-in junction potential can be calculated using the expression:

$$V_{bi} = \frac{k \times T}{e} \times \ln\left(\frac{N_A \times N_D}{n_i^2}\right) \tag{4.2}$$

where k is Boltzmann's constant, T is the absolute temperature, e is the electron charge, n_i is the intrinsic carrier concentration, and N_A and N_D are the acceptor and donor

concentrations [13]. Multiple junctions that are not far apart may cause the carriers to be redistributed, such as for the case where a Schottky contact is located close to the *p*-*n* junction. Furthermore, trap states at the native surface oxide/NW interface or within the oxide itself will form a surface depletion region which further complicates transport analysis [14,15]. Thus, more comprehensive simulations are necessary when charge distributions and any changes in the sample geometry (eg. local NW thickness) are taken into consideration. Careful comparison between simulation and experiment could then give information about the distribution and concentration of the active dopants. In this study, electron holography has been used to map the electrostatic field across the axial *p*-*n* junction and the Au catalyst Schottky contact of a Si NW and estimates of the active dopant concentrations have been extracted based on comparisons with simulations.

4.2 Experimental Details

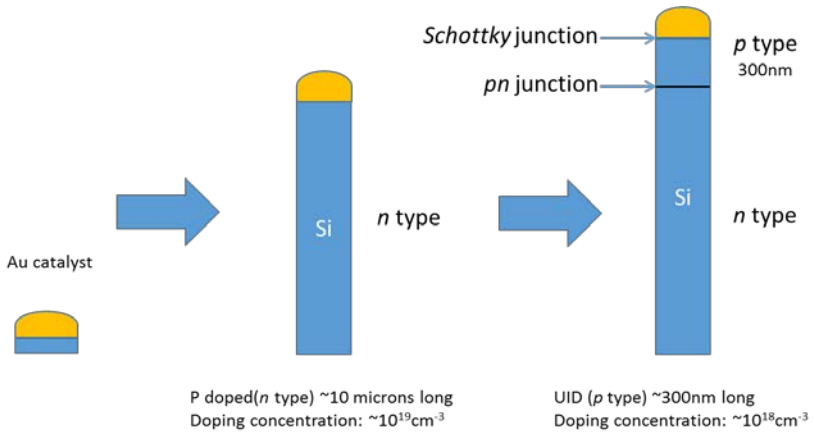

Figure 4.1 Schematic diagram of the Si NW growth procedure: (a) Au particles were deposited on Si substrate as catalysts; (b) *n*-type Si segment was grown using P as dopant; (c) P source was switched off and a *p*-type Si segment was grown due to unintentional dopant.

Figure 4.1 shows a schematic diagram of the Si NW growth procedure. The Si NWs with axial *p*-*n* junctions were grown in a cold-wall chemical vapor deposition reactor via the vapor-liquid-solid (VLS) method using 30-60 nm diameter Au colloid nanoparticle catalysts on silicon (111) substrates. The growth sequence is as follows. A ~10-μm-long phosphorus-doped (*n*-type) Si segment was initially grown using the gas mixture of SiH_4 and PH_3 at a growth temperature of 550°C and total pressure of 3 Torr. A partial pressure ratio of $PH_3/SiH_4 = 5.3 \times 10^{-3}$ was used which would result in an estimated doping concentration of ~10^{19} cm^{-3}. The PH_3 gas was then turned off, and a ~300-nm segment of pure unintentionally-doped Si was grown before termination of growth. For unintentional doping, the pure Si segment tends to be *p*-type as a result of electrical trap defects near the interface due to the presence of a thin oxide layer on the NW surface; the corresponding dopant concentration was estimated to be roughly 10^{17} to $10^{18}$$cm^{-3}$ [Ref. 15]. A *p*-*n* junction should thus be formed in the Si NW at a distance of about 300 nm away from the Au catalyst at the tip of the NW. For TEM analysis, the NWs were ultrasonicated in isopropyl alcohol and transferred via pipette to TEM copper mesh grids with holey carbon support films, and air-dried before observation.

Electron microscopy and off-axis electron holography characterization were carried out using FEI CM200 and Tecnai F20 TEMs equipped with electrostatic biprisms and operated at 200 kV. Holograms were taken using the Lorentz mini-lens with the objective lens switched off to obtain a larger field of view. The typical biprism voltage was 120 V giving a fringe spacing of about 5nm at the usual magnification of 20kX. The exposure time for hologram recording was 2s.

4.3 Results and Discussions

Electron micrographs taken from near the catalyst tip show the as-grown NW to have excellent crystallinity with a diameter of 80 nm (Figure 4.2). A slightly tapered morphology is observed and attributed to unintentional vapor-solid-solid growth during synthesis [16]. The change of doping during NW growth did not appear to introduce any kinking or defects. A close look at faint dark spots near the NW tip indicated that some small Au particles were present on the NW surface, due to Au surface diffusion from the catalyst particle during growth [17,18]. However, these particles were limited to a region of ~80 nm from the NW tip, and their amount was small with a concentration of ~$10^{11}$$cm^{-2}$ as estimated from the images, so that they were not expected to have a significant effect on the measurements of electrostatic potential profile.

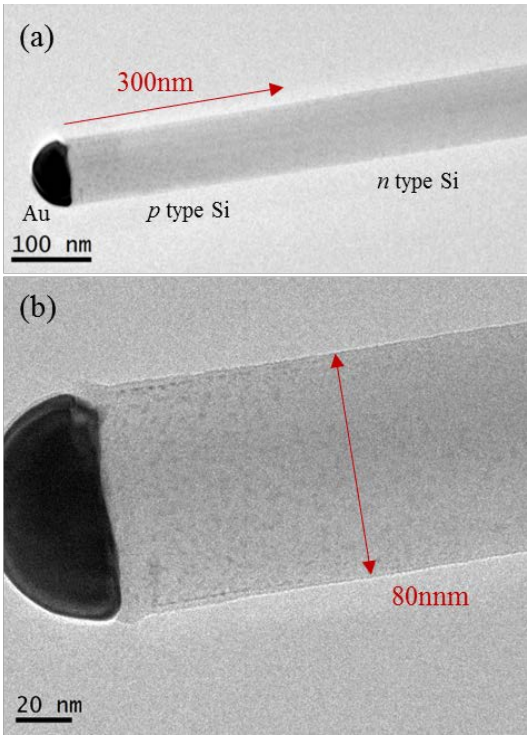

Figure 4.2 Electron micrographs showing the morphology of a typical Si NW, with *p*-*n* junction location estimated to be ~300nm from top end of the NW.

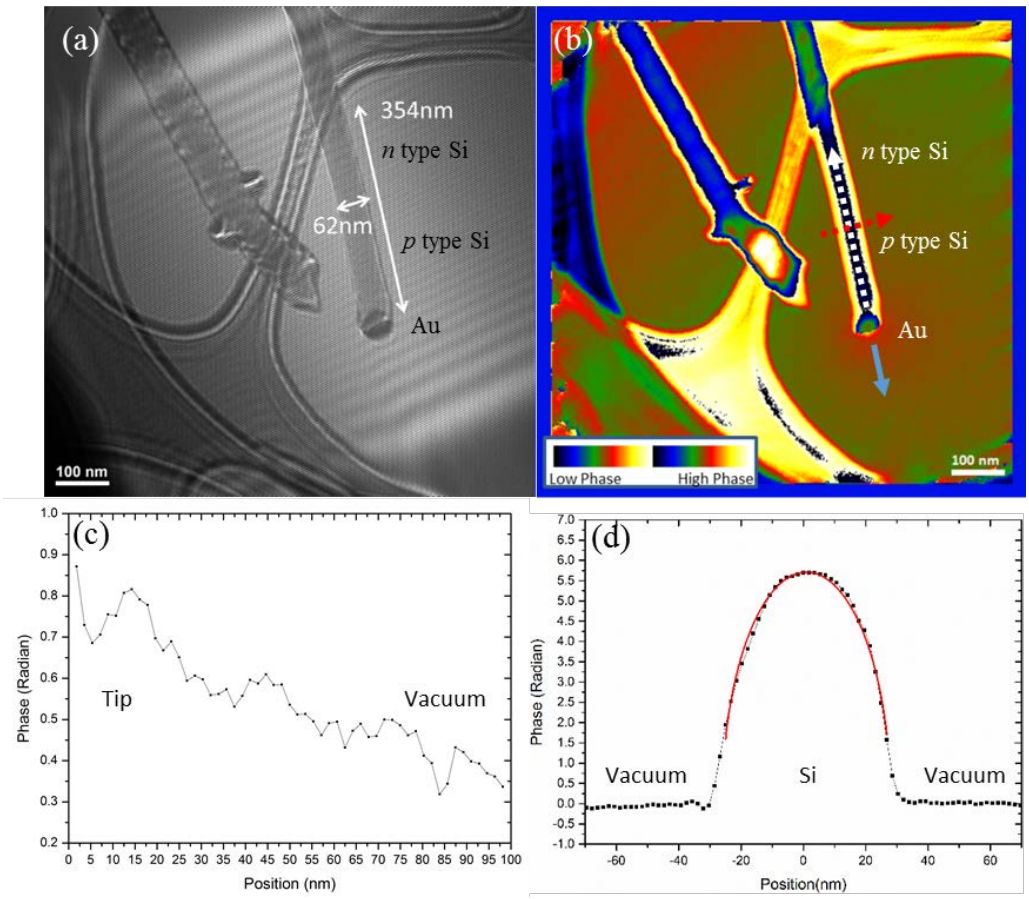

Figure 4.3 (a) Hologram of doped Si NW supported on holey carbon film; (b) Reconstructed phase image visualized with pseudo-color; (c) Phase profile along blue arrow in (b); (d) Phase profile across width of NW along the red arrow in (b) and fitting result (red line) using cylindrical NW model.

Electron holography from across the diameter and upper end of a different NW (Figure 4.3) reveals the effect of the Au catalyst tip and surface charge on the resultant phase profile. In this case, the NW is about 62nm in diameter and it is grounded with the *n*-type segment base via contact with the carbon grid, while the upper *p*-type segment with Au catalyst protrudes out into vacuum. Figures 4.3a and 4.3b show the original hologram

and the reconstructed phase image respectively, using pseudo-colorization to emphasize the phase change. The phase profile in Figure 4.3c, taken along the NW (blue arrow in Figure 4.3b), shows a monotonic decrease in phase to zero moving away from the tip. This higher phase in the vacuum outside the Au particle suggests that the catalyst is positively charged, most likely due to secondary electron emission under the high-energy electron beam used during imaging. The phase profile across the NW shown in Figure 4.3d (red arrow in Figure 4.3b), indicates that the NW cross-section is approximately round, by comparing the experimental result (black dots) with the fitting result using a cylindrical NW shape (red line). The flat phase in the surrounding vacuum region suggests that any NW surface charge is small [10]. The thickness profile extracted from the reconstructed thickness image along the white arrow in Figure 4.3b suggests that the projected thickness of NW is constant with a value of ~60nm, which is consistent with the width measurement of the NW and confirms the assumption of cylindrical NW shape.

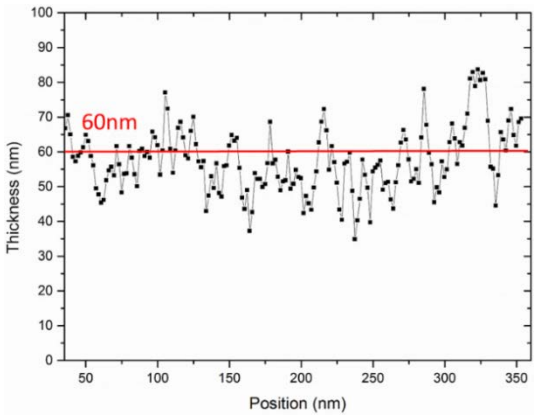

Figure 4.4 Thickness profile along white arrow in Figure 4.3b showing the NW has a constant projected thickness of ~60nm.

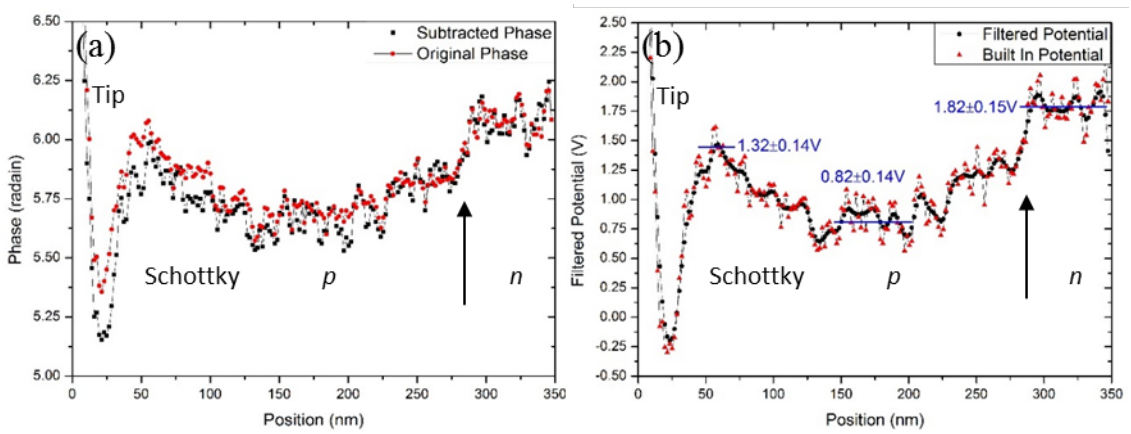

Figure 4.5 (a) Vacuum-subtracted phase line profile along white arrow in Figure 4.3b; (b) Built-in potential before and after application of Gaussian filter.

The phase profile along the length of the NW, as shown in Figure 4.5a, reveals the electrostatic potential profile of the *p*-*n* junction (white arrow in Figure 4.3b). The approximate position of the *p*-*n* junction is indicated by the arrow. In order to remove the phase shift due to the projection of the electric field in vacuum caused by charging at the Au catalyst tip, a similar line profile is also extracted from the vacuum region along the edge of the NW and then subtracted from the NW profile. The difference is the phase profile due only to the NW, as shown in the subtracted phase of Figure 4.5a. By comparing the original phase and the subtracted phase, it appears that charging at the Au particle most strongly influences the phase near the tip, whereas the phase around the region of the *p*-*n* junction remains unchanged because the fringing electrostatic field from the Au particle has been attenuated.

Based on the subtracted phase, an average built-in potential profile was calculated using equation (4.2) and shown in Figure 4.5b, taking the NW thickness of 62 nm, as measured from its diameter, and a mean inner potential for intrinsic Si of 12.1 V [19]. A

Gaussian filter is then applied to the profile to remove high frequency noise. The small peaks in the profile shown in Figure 4.5b may still be due to noise rather than electrostatic field because of the low signal-to-noise ratio. The potential step located at ~300 nm is consistent with the position of the *p*-*n* junction, while the potential drop located near ~100 nm possibly represents a Schottky contact formed between the Au catalyst and the Si NW [12]. The built-in potential at the *p*-*n* junction drops from 1.82±0.15 V at the *n*-type segment to 0.82±0.14V at the *p*-type segment so that the *p*-*n* junction height is estimated to be 1.0±0.3 V. The error estimates are based on the standard deviations of each separate potential measurement. In contrast, the built-in potential at the Schottky contact goes from 0.82±0.14 V at the *p*-type segment to 1.32±0.14V at the Au particle, giving a barrier height of 0.5±0.3V. We note that the apparent drop in potential visible at ~25 nm from the Au catalyst is likely to be due to a Fresnel fringe originating from the edge of the Au particle. We attribute the steep increase in potential within the NW at distances of less than 25 nm as being due to the much higher MIP of Au compared with that of Si.

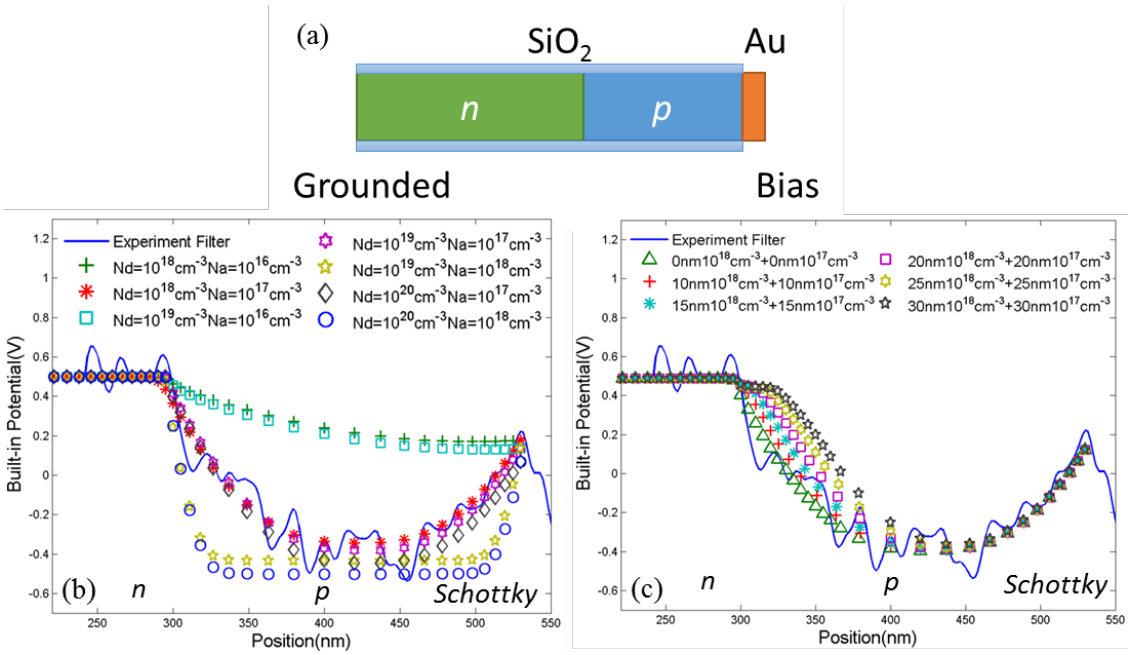

Figure 4.6 (a) Schematic showing cross section of model used for simulations consisting of Si NW with *p*-*n* junction, grounded on the *n*-side and biased on the Au particle at the end of the *p*-doped region; (b) Experimental built-in potential profile and simulated profiles for different dopant concentrations at *p*-*n* junction, work function ϕ =4.6 V; (c) Simulated built-in potential profiles with different gradient widths, dopant concentrations $N_A=10^{17}$ cm^{-3}, $N_D=10^{19}$ cm^{-3}, and work function ϕ =4.6 V. Two layers in the dopant concentrations of $N_D=10^{18}$ cm^{-3} and $N_D=10^{17}$ cm^{-3}, respectively, are added after *n*-type region with layer widths as shown in the legend.

In order to better interpret the electrostatic potential profiles, simulations of the NW potential distribution were performed using the Silvaco™ software package. The parameters for the simulation are schematically illustrated in Figure 4.6a. The Si NW was simulated as a cylinder with a diameter of 62 nm and an SiO_2 shell of 5 nm. The SiO_2 was used to define surface charge so that its thickness should not influence the results. Since

the effect of the surface charge was not apparent in the experimental results, the surface charge in the simulation was defined to be zero at the interface between Si and SiO_2. The validity of this assumption was tested by additional simulations with varying surface charges, as discussed below. The *n*-type segment of the Si NW was connected to ground, while the *p*-type segment was connected to Au via a Schottky contact with bias applied to the Au contact. An abrupt junction model was initially used in the simulations, but a non-abrupt junction was later tested and did not affect the overall trend of the results. The donor concentration, acceptor concentration, Au work function and bias were then systematically adjusted in order to find a match with the experimental electrostatic profile.

As shown by the magenta hexagrams in Figure 4.6b, a donor concentration of ~10^{19} cm^{-3}, an acceptor concentration of ~10^{17} cm^{-3}, a work function of 4.6 V and 0 V bias gave the best fit to the experimental profile. The corresponding simulated built-in potential height and depletion length for the *p*-*n* junction were 0.93 V and 120 nm, respectively, and 0.51 V and 100 nm for the Schottky contact, respectively. These values are consistent with the experimental values. Most of the depletion region was located on the lower concentration, *p* side. Since the distance between the *p*-*n* junction and the Schottky contact is ~250 nm, they should not have any significant effect on each other. By using Equation 4.3, the built-in potential due to single *p*-*n* junction can also be calculated to be ~1V with a depletion region width of ~112nm, which confirms the simulation results above. When the simulated acceptor concentration is lower than 10^{17} cm^{-3} (refer to colored points) or the donor concentration is lower than 10^{19} cm^{-3} (refer to colored points), then the depletion regions across the *p*-*n* junction and the Schottky contact are larger and the built-in potential changes less rapidly, resulting in a higher potential in the *p*-type region than measured

experimentally. Conversely, when the simulated acceptor concentration is greater than 10^{17} cm^{-3} (refer to colored points) or donor concentration is greater than 10^{19} cm^{-3} (refer to colored points), the depletion region of the *p*-*n* junction and the Schottky contact are smaller and the built-in potential changes more rapidly, giving deeper potential in the *p*-type region than measured.

Any change in dopant concentration during VLS growth usually results in an exponentially-decreasing gradient at the interface [20-22], with a length that is comparable to the NW diameter, which is ~60 nm in this case, forming an n^+-n^--*p* junction. To assess the effect of such gradients, two *n*-type segments with concentrations of 10^{18} cm^{-3} and 10^{17} cm^{-3}, respectively, were added in the simulations between the *n*-type and *p*-type segments, as shown in Figure 4.6c. The simulations suggest that the short n^- portion is fully depleted and has only a small effect on the *p*-*n* junction, making the junction slightly flatter in the middle. As the gradients become longer, the flatter part is extended further into the *p*-type segment. Because the total depletion length is very long compared to the gradient due to low concentration on the *p* side, the gradients do not have a significant effect on the junction height nor the total depletion width.

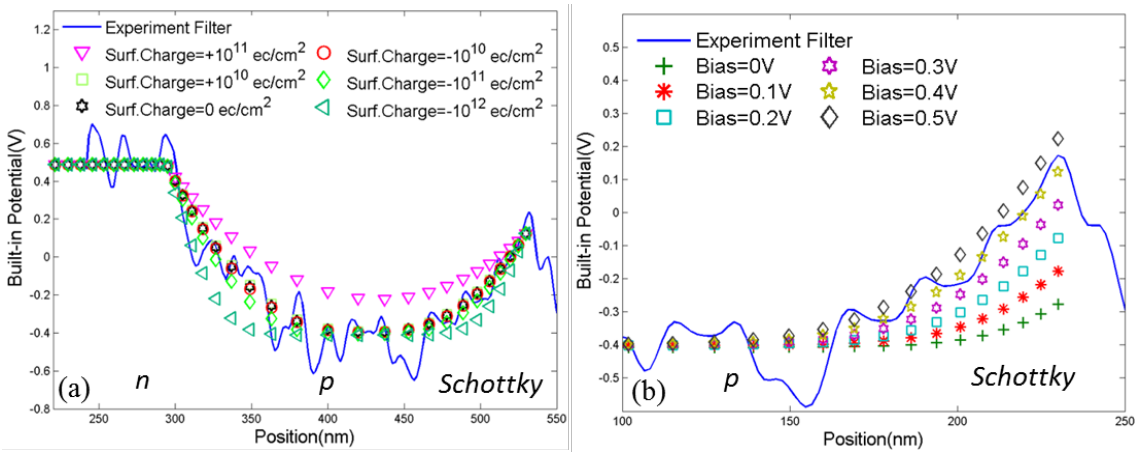

Figure 4.7 (a) Simulated built-in potential profiles with different surface charges and experimental potential profile, dopant concentrations $N_A=10^{17}$ cm^{-3}, $N_D=10^{19}$ cm^{-3}, work function ϕ =4.6V; (b) Simulated built-in potential profiles with different bias on a single Schottky diode, dopant concentrations $N_A=10^{17}$ cm^{-3}, work function ϕ =5V.

A conformal native oxide is usually observed on Si NW surfaces resulting in interface charge or surface states around the NWs [14,15]. However, the flat phase observed in vacuum near the NW indicated that the interface charge was too small to be directly detected by phase change in the present measurements. To investigate possible effects of the interface charge on the inferred dopant profiles, various surface charges were added to the simulations. A charge density of 10^{11} electron/cm^2 did not have a significant effect on the results, as shown in Figure 4.7a. As the surface charge was increased, the built-in potential went either slightly higher or lower in the *p*-type Si, depending on the sign of the charge. A closer look at the phase image at the edge of the NW shows that the edge is equal-phase or equipotential across the *p*-*n* junction, suggesting that the potential is pinned at mid-gap at the NW surface, which could indicate a small depletion region at the NW

surface due to surface states [23]. This depletion region may also cause somewhat lower measured dopant concentrations since averaged values are being measured through the thickness.

Si NWs with Au contacts have been reported to form Schottky barriers due to their differences in Fermi level [12,24], which is consistent with our observations. The built-in potential height and depletion region width of the Schottky barrier depend on the *active* dopant concentration, the bias applied to the barrier, interface oxide charge and surface states. If only active dopant and bias are considered, the built-in potential can be expressed as:

$$V_{bi} = \chi + \frac{E_c - E_f}{q} - \phi + V_{bias} \tag{4.3}$$

where χ is the electron affinity for silicon, E_c is the conduction band energy, E_f is the Fermi level, q is the electron charge, ϕ is the Au work function and V_{bias} is the bias applied to Au [13]. The Au work function and bias both contribute to the height of the built-in potential of the barrier according to this equation.

Simulation results for a biased Schottky diode with 0.4 V bias without *p*-*n* junction are given in Figure 4.7b, and these show a very good fit with the experimental profile. Since the Au is positively charged, the Schottky contact is in reverse bias. The Fermi level on the Au side will be lower, increasing the height of the built-in Schottky potential. If the Si *p* side remains grounded and its Fermi level stays flat, the bias will only change the Fermi level across the Schottky contact, rather than the whole Si NW, which is equivalent to applying bias to a single Schottky diode without *p*-*n* junction. Simulations with a lower work function of 4.6 V, compared to values reported in the literature of around 5V [25], give the best fit here with experiment. Therefore, in Figures 4.6b, 4.6c and 4.7a, such bias

can be considered as a change of work function in the simulation that keeps the Fermi level flat across the *p*-*n* junction.

4.4 Conclusions

Si NWs have been grown with axial *p*-*n* junctions using the VLS method. A Schottky junction is formed at the end of the NW due to the presence of the Au catalyst particle. The electrostatic potential profile measured by electron holography shows that the built-in potentials across the *p*-*n* junction and the Schottky junction, have values of 1.0±0.3 V and 0.5±0.3 V, respectively. Simulations indicate that the dopant concentrations are ~$10^{19}$$cm^{-3}$ for donor and ~10^{17} cm^{-3} for acceptor. The positively charged Au particle at the end of the grounded NW is considered to account for the lower work function in the simulation. The effects of a possible transition region forming n^+-n^--*p* junction and possible surface charge were also systematically studied by simulations. Overall, these results demonstrated that the off-axis electron holography technique can provide valuable information on the electrically active dopant distributions in NW device structures.

References

[1] Z. Gan, D. E. Perea, J. Yoo, S. Tom Picraux, D. J. Smith, and M. R. McCartney, Applied Physics Letters **103** 153108 (2013).

[2] V. Schmidt, J. V. Wittemann, S. Senz, and U. Gösele, Advanced Materials **21** 2681 (2009).

[3] Y. Cui, Q. Wei, H. Park, and C. M. Lieber, Science **293** 1289 (2001).

[4] J. Goldberger, A. I. Hochbaum, R. Fan, and P. Yang, Nano letters **6** 973 (2006).

[5] P. M. Voyles, D. A. Muller, J. L. Grazul, P. H. Citrin, and H. J. Gossmann, Nature **416** 826 (2002).

[6] T. Tanaka, N. Murata, K. Saito, M. Nishio, Q. Guo, and H. Ogawa, physica status solidi (b) **244** 1685 (2007).

[7] D. E. Perea, E. R. Hemesath, E. J. Schwalbach, J. L. Lensch-Falk, P. W. Voorhees, and L. J. Lauhon, Nature nanotechnology **4** 315 (2009).

[8] M. R. McCartney and D. J. Smith, Annual Review of Materials Research **37** 729 (2007).

[9] M. R. McCartney, N. Agarwal, S. Chung, D. A. Cullen, M.-G. Han, K. He, L. Li, H. Wang, L. Zhou, and D. J. Smith, Ultramicroscopy **110** 375 (2010).

[10] M. I. den Hertog, H. Schmid, D. Cooper, J.-L. Rouviere, M. T. Björk, H. Riel, P. Rivallin, S. Karg, and W. Riess, Nano letters **9** 3837 (2009).

[11] L. Li, D. J. Smith, E. Dailey, P. Madras, J. Drucker, and M. R. McCartney, Nano letters **11** 493 (2011).

[12] H. Kai, C. Jeong-Hyun, J. Yeonwoong, S. T. Picraux, and C. John, Nanotechnology **24** 115703 (2013).

[13] S. M. Sze, Physics of semiconductor devices. Wiley-Interscience, New York, (1969).

[14] I. Kimukin, M. S. Islam, and R. S. Williams, Nanotechnology **17** S240 (2006).

[15] S. Ingole, P. Manandhar, S. B. Chikkannanavar, E. A. Akhadov, and S. T. Picraux, Electron Devices, IEEE Transactions on **55** 2931 (2008).

[16] S. A. Dayeh, J. Wang, N. Li, J. Y. Huang, A. V. Gin, and S. T. Picraux, Nano letters **11** 4200 (2011).

[17] S. A. Dayeh, N. H. Mack, J. Y. Huang, and S. T. Picraux, Applied Physics Letters **99** 023102 (2011).

[18] J. E. Allen, E. R. Hemesath, D. E. Perea, J. L. Lensch-Falk, Z. Y. Li, F. Yin, M. H. Gass, P. Wang, A. L. Bleloch, R. E. Palmer, and L. J. Lauhon, Nature nanotechnology **3** 168 (2008).

[19] J. Li, M. R. McCartney, and D. J. Smith, Ultramicroscopy **94** 149 (2003).

[20] T. E. Clark, P. Nimmatoori, K.-K. Lew, L. Pan, J. M. Redwing, and E. C. Dickey, Nano letters **8** 1246 (2008).

[21] D. E. Perea, N. Li, R. M. Dickerson, A. Misra, and S. T. Picraux, Nano letters **11** 3117 (2011).

[22] N. Li, T. Y. Tan, and U. Gösele, Applied Physics A **90** 591 (2008).

[23] D. Cooper, C. Ailliot, J.-P. Barnes, J.-M. Hartmann, P. Salles, G. Benassayag, and R. E. Dunin-Borkowski, Ultramicroscopy **110** 383 (2010).

[24] E. Koren, N. Berkovitch, O. Azriel, A. Boag, Y. Rosenwaks, E. R. Hemesath, and L. J. Lauhon, Applied Physics Letters **99** 223511 (2011).

[25] P. A. Tipler, Modern physics. Worth Publishers, New York, (1978).

CHAPTER 5

MEASUREMENT OF ACTIVE DOPANTS IN AXIAL Si-Ge NANOWIRE HETEROJUNCTIONS USING OFF-AXIS ELECTRON HOLOGRAPHY AND ATOM-PROBE TOMOGRAPHY

This chapter describes the measurement of active dopants in axial Si-Ge nanowire (NW) heterojunctions using off-axis electron holography and atom-probe tomography. The axial Si-Ge NWs were grown using the vapor-liquid-solid method, and were provided by Daniel Perea from Pacific Northwest National Laboratory, Jinkyoung Yoo and Tom Picraux from Los Alamos National Laboratory. The atom-probe tomography experiment was performed by Daniel Perea. My role in this work included preparation of TEM samples, characterization of the NW structures, measurements of electrostatic and built-in potential profiles across the hererojunction and Schottky junctions in axial Si-Ge NWs using off-axis electron holography, and device simulations for active dopant determination. The main results of this work have been submitted for publication [1].

5.1 Introduction

Semiconductor heterostructures have many novel and attractive applications compared with individual semiconductors such as Si due to their ability to tune electronic transport properties by varying composition in addition to dopant type and concentration [2]. Si-Ge axial heterojunction nanowires (NWs) are considered as potential high-performance transistor devices because Ge has low effective mass, high mobility and small band gap compared with Si [3]. Moreover, the NW geometry can reduce the density of

dislocations caused by lattice mismatch [2], and also provide new options for 3D device integration [4,5]. Axial Si/Ge NW heterojunctions with abrupt interfaces have been grown using the vapor-liquid-solid (VLS) [6] and vapor-solid-solid (VSS) methods [7]. Changes in electronic transport properties have been achieved with different dopant profiles by growing Ge NWs on Si pillars formed by etching [8]. To improve the engineering and performance of Si-Ge NW integrated devices, it is necessary to understand their charge transport mechanisms. In particular, knowledge of active dopant profiles and the resultant built-in potential can play a critical role.

The present study has used off-axis electron holography (EH) to measure the built-in electrostatic potential across doped Si-Ge NW heterojunctions with/without *in situ* bias, in combination with atom-probe tomography (APT) to measure the total dopant distributions. The active dopant profiles were then extracted by comparing the experimental results with TCAD simulations.

5.2 Experimental Details

Figure 5.1 shows a schematic diagram of the NW growth procedure. The axial Si-Ge heterojunction NWs were grown using the VLS method in a cold-wall CVD reactor [6]. The growth process was as follows. First, Si (111) substrates were solvent-cleaned and native-oxide-etched. Then Au colloid nanoparticles were dispersed as catalysts on the substrate surface. Germane (GeH_4) diluted in hydrogen (H_2) with a concentration of 30% was introduced into the chamber, while the total pressure was maintained at 3 Torr. The Ge <111> NW growth was initiated at 340℃ for 3min followed by further growth at 280℃ for 20−30mins. 100 ppm diborane (B_2H_6) diluted in H_2 was also introduced to provide a *p*-

type dopant during growth. To form the AuGa alloy catalyst and to reduce Ge solubility in the catalyst prior to formation of the heterojunction, trimethylgallium (TMGa) at ~90 μmol/min was introduced into the chamber for 15s using H_2 as carrier gas while the GeH_4 was still on and B_2H_6 gas shut off. Both TMGa and GeH_4 were then turned off, while silane (SiH_4) diluted in H_2 with a concentration of 50%, and 5000 ppm phosphine (PH_3) diluted in H_2, were introduced to start the Si <111> segment growth with *n*-type doping, thereby forming the axial Si-Ge NW heterostructure. The growth temperature was increased to 495℃, while the total pressure was reduced to 0.5Torr. Some NWs were specifically grown on microfabricated Si micropost substrates for APT analysis [9]. For transmission electron microscopy (TEM), scanning TEM (STEM) and EH analysis, the NWs were ultrasonicated in isopropanol and transferred via pipette to TEM copper mesh grids with thin carbon films, and then air-dried before observation.

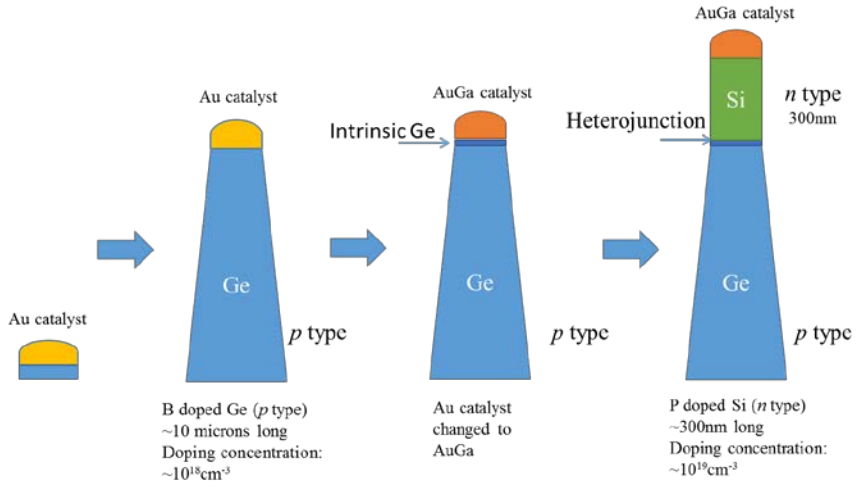

Figure 5.1 Schematic diagram of the axial Si-Ge NW growth procedure: (a) Au particles were deposited on Si substrate as catalysts; (b) *p*-type Ge segment was grown using B as dopant; (c) Ga was added to catalyst, forming AuGa alloy, and *i*-type Ge segment was grown; (d) *n*-type Si segment was grown using P as dopant.

Atom probe tomography (APT) is currently the only technique that can directly quantify the relative composition and distribution of dopants within nanowires [10]. Here we have used APT to measure the total dopant profile along the nanowire growth axis across the Si-Ge heterojunction. Due to a combined limitation in detection efficiency and spatial resolution, APT analysis cannot provide information about the bonding environment of the dopants, and thus cannot provide information about whether dopants are interstitially (electrically inactive) or substitutionally (electrically active) incorporated. Thus, APT only provides the *total* dopant composition. However, when combined with EH which can be used to estimate the composition of *electrically active* dopants, any differences between the two techniques can lead to an estimate of doping efficiency.

Determination of the electrically active dopants in the Si-Ge NWs is an important step towards useful device applications. Off-axis electron holography is an interferometric TEM technique that can provide amplitude and phase information about the sample under observation [11,12]. By using the reconstructed phase image, the electrostatic potential profile and thus the built-in potential of the sample, can be measured and compared with simulations to estimate the active dopant concentrations. For a non-magnetic sample and assuming that the potentials are distributed uniformly across the projected thickness, the phase shift in a reconstructed phase image can be simplified to:

$$\Delta\varphi(x,y) = C_E \times (V_0(x,y,z) + V_{bi}(x,y,z)) \times t \qquad (5.1)$$

where C_E is an electron-energy-dependent interaction constant having the value of 0.00653 rad. V^{-1}. nm^{-1} for 300-keV electrons, V_0 is the mean inner potential (MIP) of the sample caused by incomplete screening of atomic cores, V_{bi} is the built-in electrostatic potential resulting from any electric field and/or charge accumulation in the sample and t is the

projected sample thickness [12]. The EH technique has been widely used for characterizing electrostatic potential profiles in nanoscale semiconductors [13-15].

TEM, STEM and EH studies were done using an FEI Titan 80-300 equipped with a Schottky field-emission electron gun, probe corrector, Lorentz mini-lens and electrostatic biprism. The EH experiments were performed using the Lorentz mini-lens with the normal objective lens switched off in order to obtain a larger field of view. The biprism voltage was typically 120 V, giving 2.5-nm interference-fringe spacing, and the hologram exposure time was 2 s. APT analysis was performed using a LEAP 4000X-HR. A 355-nm UV laser pulsed at 200 kHz was used to initiate thermally-assisted field evaporation at a detection rate of 0.005 ions/pulse. A more detailed description of the APT analysis of NWs is given in reference [10].

5.3 Results and Discussions

Figures 5.2a and 5.2c show STEM HAADF images of a typical straight axial Si-Ge NW, which was grown using the same procedure but at different temperature. The tapered Ge segment is not obvious in this case. The grey region at the Si-Ge heterojunction indicates that the Ge-Si transition region is short and faceted. Catalyst materials are observable as small bright dots on the Ge surface, which is likely due to diffusion from the catalyst particle during the growth. EDX profiles were extracted across the Si-Ge heterojunction (Figure 5.2b) and the Si-catalyst interface (Figure 5.2d), along the blue arrows in Figures 5.2a and 5.2c, respectively. The EDX profile across the heterojunction suggests that the Si-Ge transition region is ~50nm long, which is short compared to growth using Au catalysts, which are usually on the size of the NW diameter (~110nm) [16]. The

short transition region confirms that the AuGa alloy reduced the amount of Ge in the catalyst because of the lower solubility, forming a much sharper Ge-Si interface [6]. The Ga content in the Si segment is not detectable. The EDX profile across the Si-catalyst interface indicates that the catalyst consists Au, Ga, Si and residual Ge, confirming that an AuGa alloy had been formed to grow the Si segment.

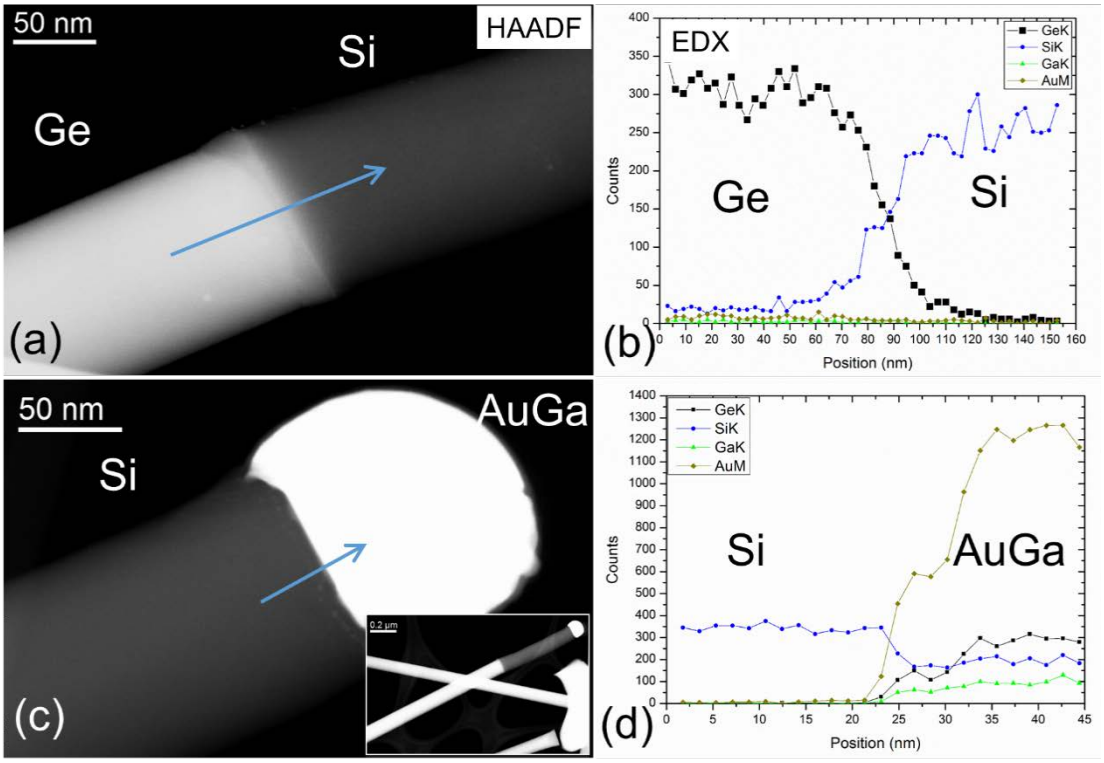

Figure 5.2 STEM HAADF images of axial Si-Ge NW (a) and (c), and EDX profiles across Si-Ge heterojunction (b) and Si-catalyst interface (d).

Figure 5.3 shows TEM and STEM images of a typical tapered axial Si-Ge NW heterostructure as used for holography and APT experiments. The NW structure includes a long tapered Ge base (~10 μm long), an untapered ~70-nm-diameter segment of Si (~300 nm long) and the AuGa catalyst particle located at the NW tip. From the growth conditions,

the Ge is doped with boron (B) at a nominal concentration of 4×10^{18} cm^{-3}, while the Si is doped with phosphorus (P) at a nominal concentration of 2×10^{19} cm^{-3}. The tapered Ge base resulted from VSS growth on the Ge surface at the growth temperature of 280℃ [17]. Small particles are also present on the NW surface and likely result from catalyst material at the NW tip being left behind during growth of the Ge segment and the transition from Ge to Si [18,19]. These small particles can serve as catalysts for dendritic NW growth perpendicular to the Ge surface, as visible in the images. A short Ge-Si transition region (~20nm in length) is also observable in this example, as shown by the blue arrow in Figure 5.3b. The EELS mapping shown in Figure 5.4 indicates a complicated Si-Ge facetted interface, similar to Figure 5.2.

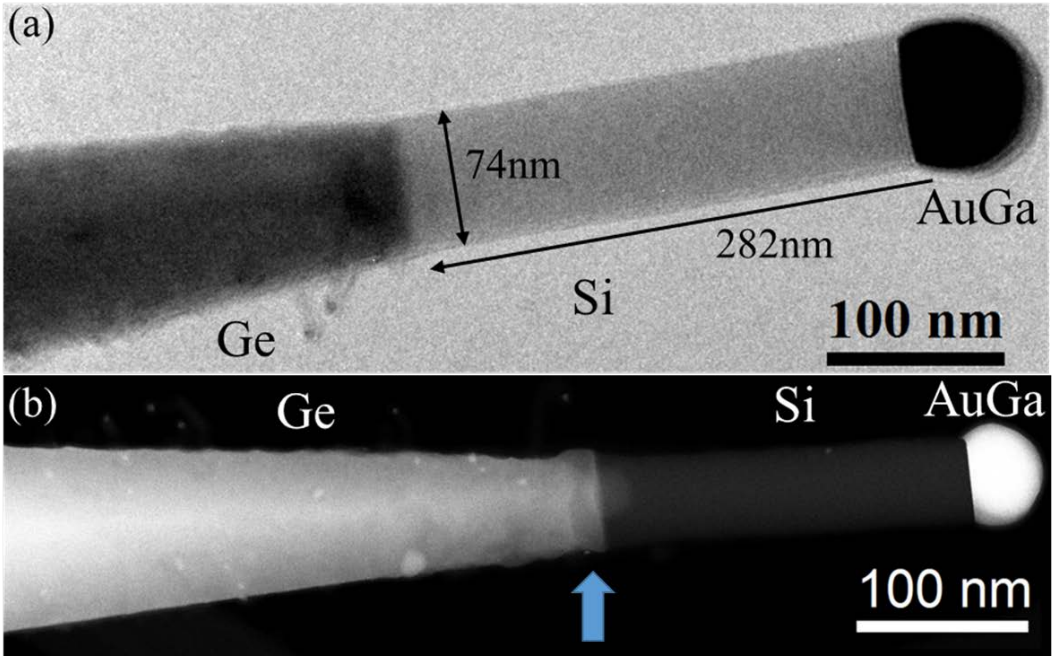

Figure 5.3 (a) TEM image showing the morphology of a typical Si-Ge heterojunction NW; (b) STEM HAADF image showing the morphology of a different Si-Ge heterojunction NW from the same growth substrate.

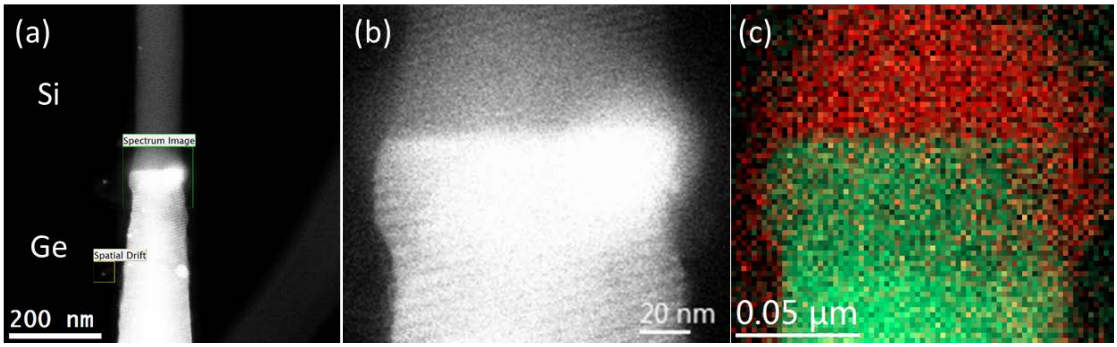

Figure 5.4 EELS mapping of axial Si-Ge NW: (a) and (b) STEM HAADF images; (c) EELS mapping of Si (red) and Ge (green) at Si-Ge interface.

Interfacial strain may affect the device electrical performance. In order to understand the strain distribution and relaxation at the Si-Ge heterojunction, Geometric Phase Analysis (GPA) was performed on a STEM HAADF image of Si-Ge NW, as shown in Figure 5.5 [20]. The diffraction spots chosen for analysis are indicated by the blue arrows in the inserted image of Figure 5.5a and the out-of-plane E_{xx} strain is shown in Figure 5.5b, which is along the [111] growth direction. The left Ge end was assumed to be unstrained and used as reference. The E_{xx} can also be calculated by using the equation below:

$$E_{xx} = \frac{c_{Si} - c_{Ge}}{c_{Ge}} \tag{5.2}$$

where c_{Si} and c_{Ge} are the lattice spacing along the [111] growth direction for Si and Ge, respectively. For relaxed Si and Ge, the lattice constants are 0.5431 nm and 0.5658 nm, respectively. Thus, the E_{xx} is calculated to be 4% for unstrained Si-Ge interface. The strain profile shown in Figure 5.5c was extracted along the white arrow in Figure 5.5b, where the blue line roughly indicates the Si-Ge interface. From ~30nm to ~55nm, the E_{xx} value drops from 0 to ~4%, which indicates that this is the strained or unstrained but chemically mixed Si-Ge transition region. Away from this region, the E_{xx} values for Si and Ge go to 4% and

0%, respectively, indicating that they are completed relaxed. The length of the strained region is consistent with the Si-Ge transition region measured from the HAADF image in Figure 5.3b. This strained region causes diffraction contrast, as shown by the darker contrast at the Si-Ge interface in Figure 5.3a.

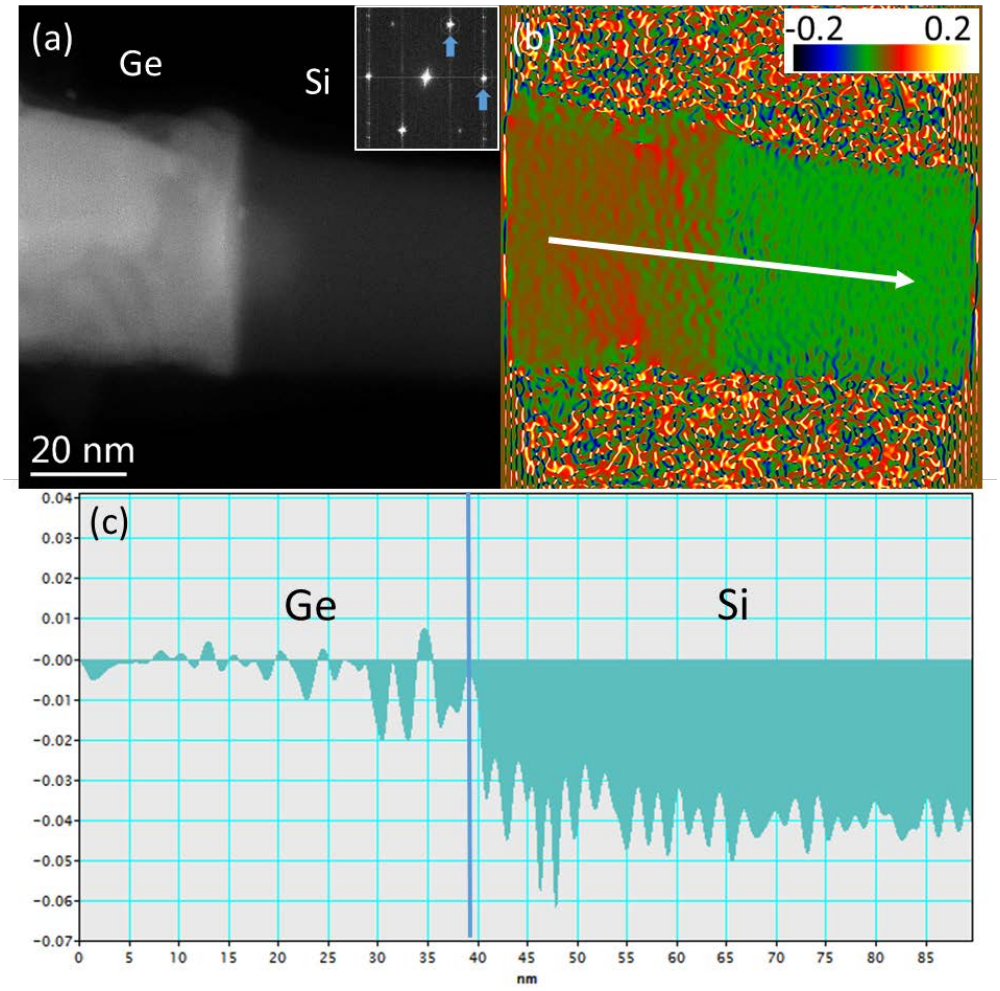

Figure 5.5 Geometric Phase Analysis of axial Si-Ge NW: (a) STEM HAADF image, with the diffraction spots chosen for analysis arrowed in the inserted diffractogram; (b) Calculated out-of-plane strain E_{xx} mapping; (c) E_{xx} Strain profile extracted along white arrow in (b).

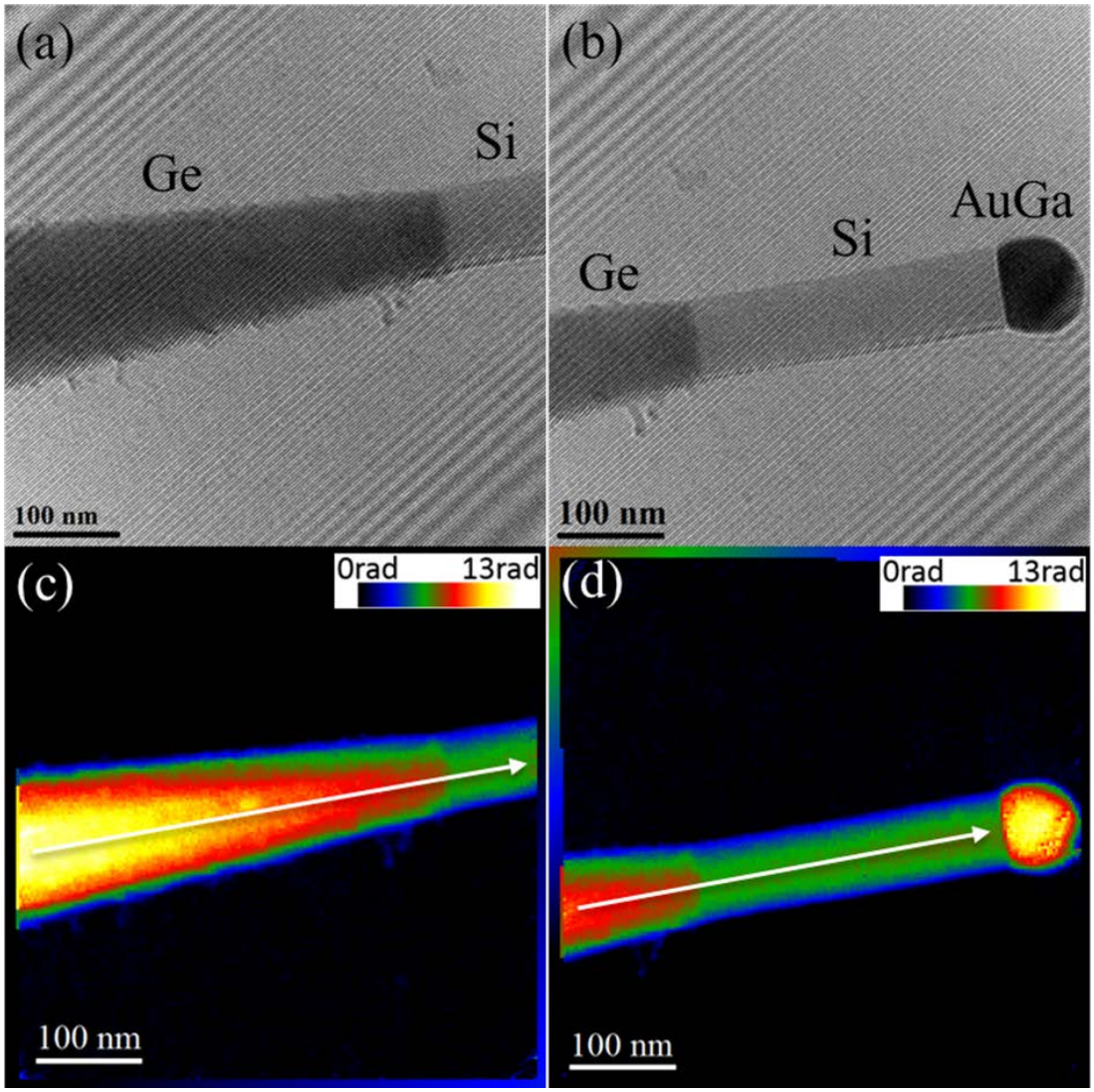

Figure 5.6 (a) and (b) Typical holograms of Si-Ge NW heterojunction; (c) and (d) Reconstructed phase images from holograms in (a) and (b), respectively.

Figures 5.6a and 5.6b show two holograms of a typical Si-Ge NW heterojunction, where the fringes that are visible result from interference of the object wave and the vacuum (reference) wave. Figures 5.6c and 5.6d show the corresponding phase images after hologram reconstruction, using pseudo-color to indicate the magnitude of the phase

change. The observed change in phase not only results from accumulated charge and/or internal electric field, but also from changes in specimen thickness and chemistry. In Figure 5.6c, the phase within the Ge segment increases towards the left, because of the increasing NW diameter. Some small dendritic growth is also visible on the Ge surface, which adds significant noise to the analysis carried out below. No dendrite growth is observed on the Si side in Figure 5.6d. Instead, the diameter of the Si NW increases slightly towards the catalyst. The phase at the NW center also increases slightly, as shown by the red color.

The change in width as a function of distance for the Ge and Si segments, as well as the corresponding phase profile, were extracted from left to right at the center of the NW, along the white arrows in Figures 5.6c and 5.6d, respectively. These results were then combined together, as shown in Figure 5.7a, where the phase is shown in black and the width is shown in red. In order to reduce the effect of noise caused by the surface dendrite growth, linear fitting is applied to the measured Ge width profile while constant width is used for the Si part (shown by the blue line). By assuming that the NW has a cylindrical shape, then its width can be used as the NW thickness projected along the electron-beam direction. The change of phase is proportional to the change in width, where a monotonic decrease in the phase profile with decreasing width is observed in the Ge segment, consistent with the tapered NW geometry. A deviation in the phase profile is observed at the heterointerface position of ~400nm, which is attributed to the difference in MIP between Ge (14.3V) [21] and Si (12.1V) [22], in addition to the built-in potential. The Si portion has almost constant diameter and phase except for the NW part located near the catalyst, where these increase slightly.

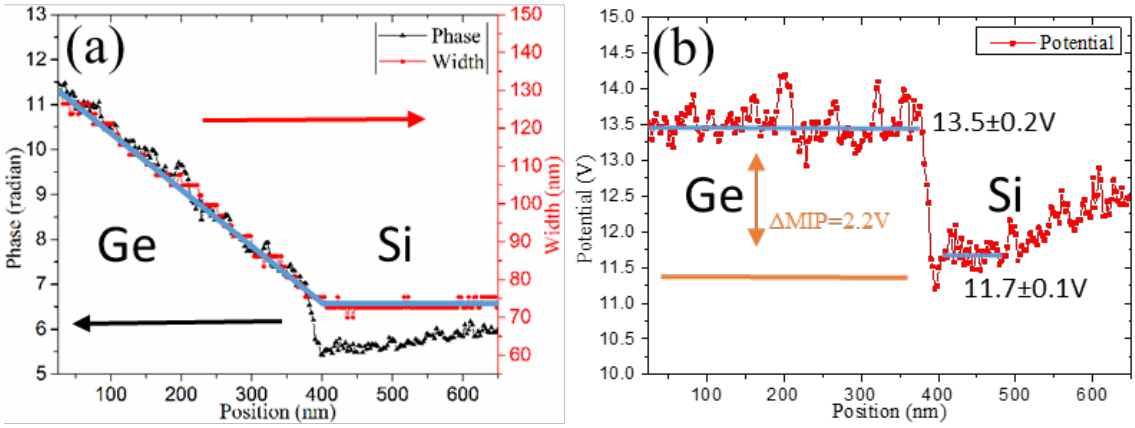

Figure 5.7 (a) Phase and width line profiles extracted from along white arrows in Figure 5.6c and 5.6d and combining results; (b) Potential profile calculated using phase line profile and width line profile after fitting (blue) in (a).

The total potential profile, which includes contributions from the MIP and the built-in potential, can be calculated using equation (1). The result is shown in Figure 5.7b, after dividing the phase line profile in Figure 5.7a by C_E and the width profile. Direct correlation of the total potential profile due to changes in the dopant type and the MIP difference between Si and Ge can be complicated by strain and electron diffraction affects near the heterointerface, thus making it difficult to determine the built-in potential profile. Instead, focus is directed towards regions away from the interface. Figure 5.7b shows that despite the potential on the Ge side being noisy, likely as a result of small dendrite growth on the surface which perturbs the phase, the potential is relatively constant and measured to be 13.5±0.2V. The potential on the Si side is initially 11.7±0.1V for roughly the first ~100nm, and then increases up to 12.4 V moving towards the position of catalyst. This increase in potential near the catalyst is discussed below. The total potential offset across the Ge-Si heterojunction is calculated to be 1.8V±0.2 V, with the Si side lower, using the larger

measurement error of 0.2V as the potential offset error. The total potential profile and the total potential offset in Figure 5.7b are due to a combination of built-in potential and the difference in MIP. The built-in potential offset across the Ge-Si interface is calculated by subtracting the MIP difference of 2.2 V between Ge and Si from the measured 1.8 V total potential offset between Ge and Si. Thus, the actual built-in potential offset of 0.4V±0.2V, with the Ge side lower, is opposite that of the total potential offset obtained from Figure 5.7b, which is primarily due to the higher mean inner potential of Ge. This built-in potential offset will be compared later with simulations to determine the active dopant (Ga, P and B) concentrations.

In order to characterize the electrical properties of Si-Ge NWs under working conditions, an *in situ* biasing experiment was carried out using a Nanofactory^{TM} biasing holder and the same EH configuration. To more easily make electrical contacts to the Si-Ge heterojunction NWs for biasing purposes, NWs were grown with *n*-Si segments that were approximately three times greater in length. Considering that the NWs used for the biasing experiments were grown using the same growth procedure described above, the compositions of these NWs are expected to be consistent with those discussed above. As shown in Figure 5.8a, the upper end of the Si segment is kinked, which could be due to twin formation arising from defect formation as well as change in growth direction from [111] to [112], possibly caused by strain relaxation in the Si region [17]. The Ge and Si ends of the NW were connected separately *in situ* to tungsten needle wires. The specific NW visible in Figure 5.8a, has a diameter of 61nm on the Si side. The Ge end was kept connected to ground, while bias was applied to the Si end, and holograms were recorded while the bias was kept at fixed values. A hologram taken at +4V bias is shown in Figure

5.8b, and the corresponding reconstructed phase image is shown in Figure 5.8c, again using pseudo-color to represent the magnitude of the phase change.

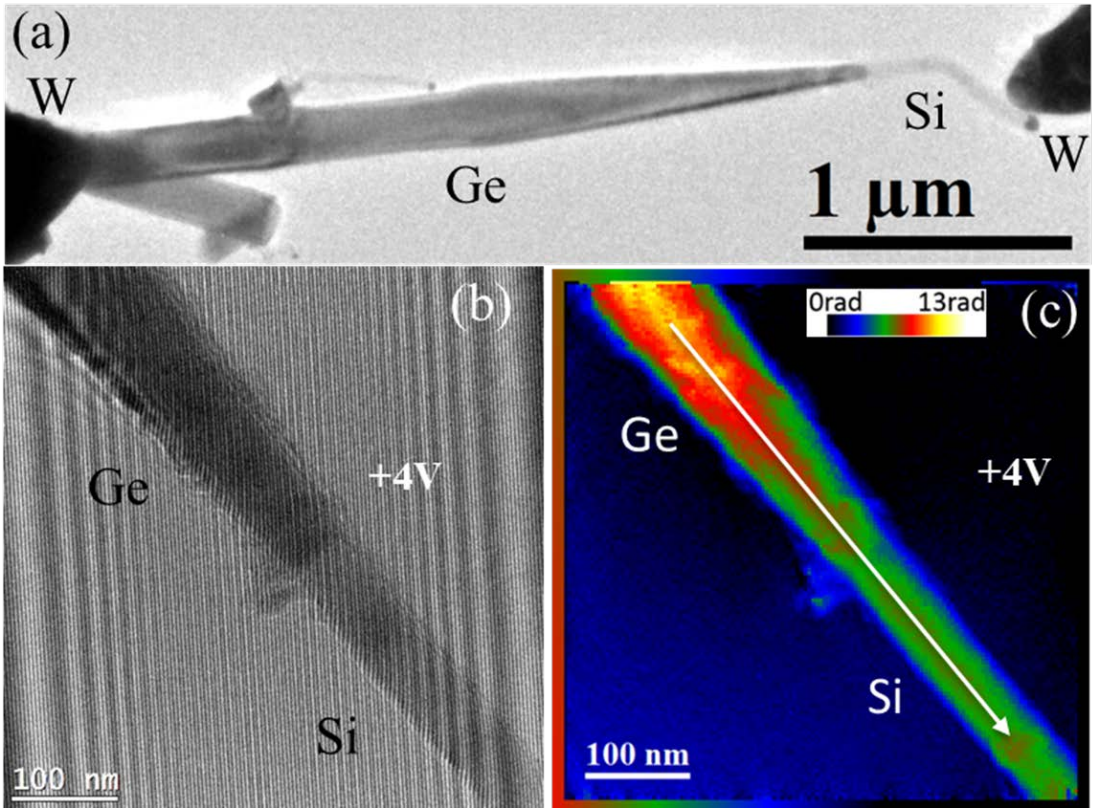

Figure 5.8 (a) TEM image showing the Si-Ge heterojunction NW after *in situ* mounting to biasing holder. (b) Typical hologram of the Si-Ge heterojunction NW with +4V bias on Si side. (c) Reconstructed phase image from (b).

To compare the electrostatic potentials across the Si-Ge heterointerface under different bias conditions, phase line profiles were extracted along the line of the white arrow from Ge to Si, as shown on the left vertical axis in Figure 5.9a. Since only the potential changes in the Si segment and across the Si-Ge heterointerface matter, but not for the grounded Ge taper base because of the high doping concentrations and short depletion

region, these phase profiles were divided by the width of the Si segment (61nm) and C_E, and then converted to potential, as also shown in Figure 5.9a, using the right vertical axis for reference. The bias conditions are shown in the legend. In Figure 5.9a, the potentials on the Ge side under different bias conditions are very similar because the Ge end is connected to ground. The linear change of phase and potential on the Ge side is caused by the tapered Ge NW shape which is not considered here. On the Si side, the potential is observed to increase in proportion to an increase in bias for applied positive voltage. For example, the potential on Si side increases by 5V, when +5 V bias is applied to the NW. The slope of potential change near the SiGe heterointerface also increases as the positive bias is increased. However, when negative bias is applied, the potential on the Si side decreases only slightly as the bias becomes more negative, although the slope change is not obvious. The dip in potential at ~250 nm is caused by the difference in MIP between Ge, Si and mixed region, offset by the built-in potential. When positive bias is applied, the bottom of the dip and the nearby mixed interface region and Ge segment also increase by small amounts as the bias increases, whereas this area remains almost constant when negative bias is applied. The slight bending in the potential and phase profiles is similar under different bias conditions and could be caused by small bending of the NW in the Si segment and/or diffraction effects, which can be seen in the darker contrast of Si in Figure 5.8b.

The corresponding current−voltage *(I-V)* characteristic curve measurement is shown in Figure 5.9b. When positive bias is applied to Si, the *I-V* curve shows a rectifying effect and the current starts to increase rapidly when the bias exceeds ~2 V. When negative bias is applied, the current starts to increase when the bias is greater than ~-2V and the *I-V* curve

in Figure 5.9b again shows a rectifying effect. The current changes faster under negative bias, relative to positive bias, while the on-voltages are very similar in value. These trends in measured potential profiles as a function of distance and bias together with the no-bias case are compared below with simulations in order to estimate the active dopant concentrations.

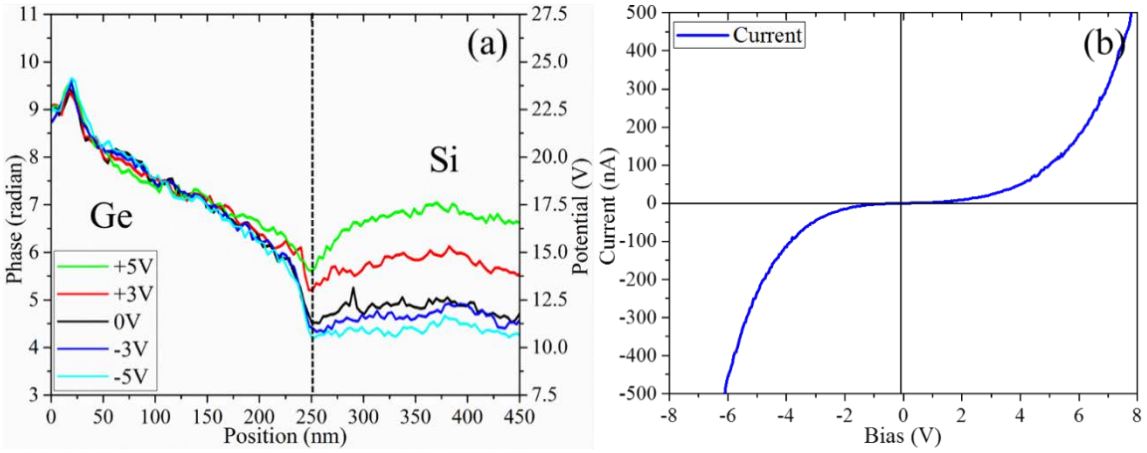

Figure 5.9 (a) Phase line profiles extracted from along white arrow in Figure 5.8c under different biasing conditions and potential profiles calculated from phase line profiles using a constant width of 61nm. (b) *IV* characteristic curve from measurement.

The results of APT measurement for a Ge-Si NW are shown in Figure 5.10. Within the Ge segment, the B distribution decreases from a doping density of ~10^{19}cm^{-3} at ~50 nm, to background levels at ~200 nm, followed by *i*-Ge growth for ~50 nm which results from the continued Ge NW growth in the absence of the B source during the lag time preceding the catalyst alloying step. The heterointerface between Ge and Si occurs at a position of ~250nm, with a width of ~10 nm consistent with the same heterointerface width measured previously by x-ray dispersive spectroscopy for very similar NWs [6]. Within the Si

segment, the P concentration increases monotonically from a dopant density of ~4×10^{18} cm^{-3} at the heterointerface, to 2×10^{20} cm^{-3} at the catalyst location. In addition to P, unintentional incorporation of Ga is also observed in the Si segment. A spike in Ga composition to ~6×10^{19} cm^{-3} is found at the heterointerface, followed by a relatively constant profile of ~2×10^{19} cm^{-3} throughout the Si segment. A detailed discussion of the reasons for the measured dopant profiles is outside the scope of this work, and will be the subject of a separate paper.

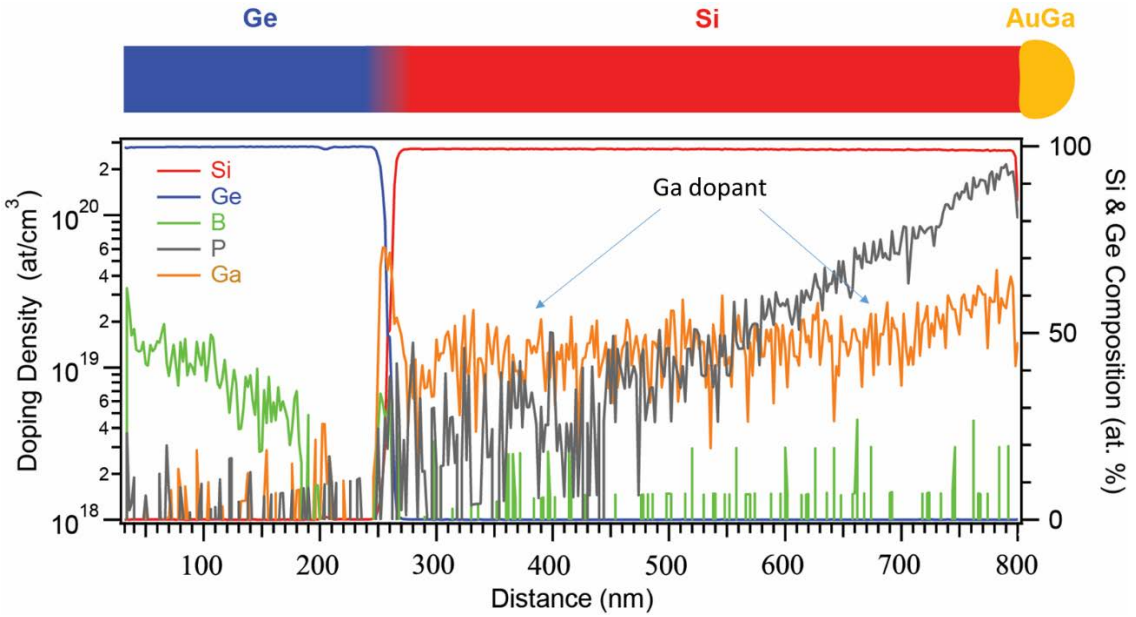

Figure 5.10 B, P and Ga dopant profiles, and Si, Ge compositions of a typical Si-Ge heterojunction NW measured using APT.

The controlled incorporation of dopants within the NW was intended to modulate the carrier type and concentration to achieve desired transport characteristics. However, the incorporation of unintentional impurities will complicate transport, especially when it has the potential to compensate intentional carriers, such as in the current case for *p*-type Ga

and *n*-type P within the Si segment. From the profiles measured by APT, a constant Ga doping density of 1-2×10^{19} cm^{-3} is observed in Si. If all dopants (B, P and Ga) are considered to be electrically active, then all of the Ga in Si would act as a *p*-type dopant and compensate the *n*-type P dopant, and the higher concentration dopant would determine the effective type of dopant.

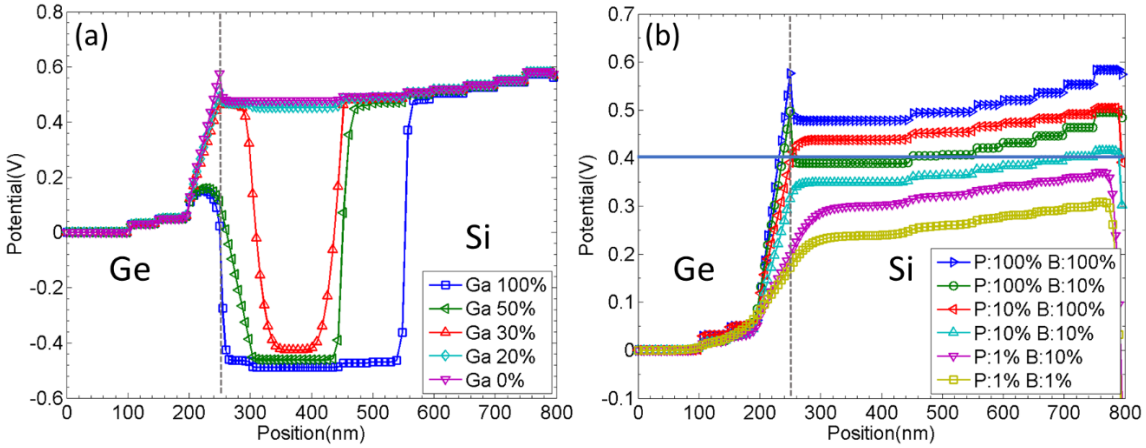

Figure 5.11 (a) Simulated built-in potential line profiles using different fractions of active Ga, fully activated B and P from Figure 5.10, where legend shows the amount of active Ga; (b) Simulated built-in potential line profiles using different fractions of active B and P, but without Ga from Figure 5.10, where legend shows the amount of active B and P.

In order to estimate the active dopant distributions, Silvaco™ TCAD simulations were performed for comparison with the APT and EH experiments. An abrupt Si-Ge interface was assumed, and the dopant profiles (B, P and Ga) from APT shown in Figure 5.10 were used for the device simulation. This result suggests that this structure should consist of *n*-type Si, to *p*-type Si, and then to *i*-Ge and finally *p*-type Ge. The simulated potential profile assuming 100% dopant activation is shown by the blue line of Figure 5.11a.

The built-in potential of the *n*-type Si would be ~0.5V (at ~600nm), while the potential of the *p*-type Si would be ~-0.4V (at ~400nm), relative to Ge (at ~0nm). Thus, this dopant profile would result in a potential drop of ~0.9V in Si from the *n*-type segment to the *p*-type segment and another 0.4V potential step across the SiGe interface with the Ge side being higher. The slow potential decrease in Si from 600nm to ~800nm is caused by the P dopant concentration decrease.

The unintentional Ga dopant in the Si part of the NW might incorporate interstitially, or it could form Ga-vacancy defects or other small defect clusters and not be fully activated. Thus, simulations with partially activated Ga are also shown in Figure 5.11a, where the legend shows the fraction of activated Ga. With lower active Ga concentrations, the *p*-type segment length in Si is reduced, while the potential offset between *n*-type Si and *p*-type Si decreases slightly (less than 0.1V from 100% to 30%). When the active Ga is reduced to concentrations lower than that of P (~20% of Ga dopant), the *p*-type Si segment disappears and only one potential drop of ~0.5V is visible within Ge at ~250nm, effectively forming an *nip*-like Si-Ge heterojunction. The experimental EH result from Figure 5.7b indicated that the built-in potential had 0.4V offset across the Si-Ge interface and the potential for the Ge side was always lower than for Si. Moreover, if there is a *p*-type Si segment, either the Si-Ge heterointerface or the *np* junction in the Si segment would always be in reverse bias and the current should be small until the junction breaks down. This situation is not consistent with the *I-V* curve measurements, as shown in Figure 5.9b. These comparisons suggest that the Ga is less than 20% activated. According to the literature [23], the solubility of Ga in Si is lower than 1×10^{19} cm^{-3}. Also, Ga dopants in Si have only been reported to be active up to ~10^{18} cm^{-3} with only partial activation at higher concentrations due to the

relatively high activation energy [24-26]. Therefore, we conclude that only a small fraction of the Ga atoms present are activated at most, and since the active Ga concentration must be lower than that of the active P, its influence can be included in the simulations below by the active P level.

In order to determine the activation of the P and B dopants, the built-in potentials across the Si-Ge heterojunction were simulated using varying amounts of active P and B, as shown in Figure 5.11b. These simulations show that the built-in potential offset between Si and Ge is ~0.48V (at ~400nm relative to Ge at 0nm), with the Ge side lower, if both P and B are fully activated (100% P and 100% B). If the active B is 100% and P is only 10%, then the potential offset is reduced to 0.44V and if the active B is only 10% and P is 100%, then the potential offset is 0.39V. Further reductions of the active P and B concentrations by an order of magnitude did not affect the built-in potential offset by very much. Moreover, most of the depletion and built-in potential change across the Si-Ge heterojunction remained in the region from 200 nm to 250 nm so that the length of the depletion region stayed at about the same size as the *i*-Ge segment (~50 nm). Since most of the built-in potential increase from Ge to Si is in the *i*-Ge region, from 200 nm to 250 nm, a phase increase in the Ge segment right before the Si-Ge interface would be expected at ~400nm in Figure 5.7b. However, this signal was not observed in the experiment, possibly because of the complexity of the SiGe interface and differences in MIP discussed above. The built-in potential offset measured from the holography experiment was ~0.4±0.2 V, which closely fitted the cases simulated for 10% B in Ge and 100% P in Si, and for 100% B in Ge and 10% P in Si. However, the potential profile from the holography experiments was noisy because of the NW surface irregularities and cannot readily distinguish the ~0.2 V

difference. Therefore, the amount of active P and B dopants cannot be accurately determined under these experimental conditions, and it can only be concluded that either 100% active P and 10% B, or 10% P and 100% B give the closest fit between experiment and simulations. A further comparison with simulation under biasing conditions is most likely needed to determine the active dopant concentrations.

In Figure 5.7b, the total change of potential in the Si segment from 500nm to 650nm is ~0.7 V, whereas the change of Si NW width, measured from the width profile in Figure 5.7a and 5.6d, is only 3%, which would only cause about 0.3 V difference. Moreover, the potential in the Si segment extending from 450nm to 800nm in Figure 5.11b increases by 0.1 V because the dopant level increases close to the catalyst. Au has been reported to form a Schottky contact with Si [13]. However, because the P dopant concentration near the catalyst is so high, the built-in potential change due to the Schottky contact is limited to a very small area adjacent to the catalyst and should not influence measurements across the Si-Ge heterojunction, as shown at ~800nm in Figure 5.11b. Thus, the increase of potential from 550nm to 650nm in Figure 5.7b can be partially explained by the combined effect of diameter increase and P dopant concentration increase. The extra potential offset could be due to diffraction near the catalyst.

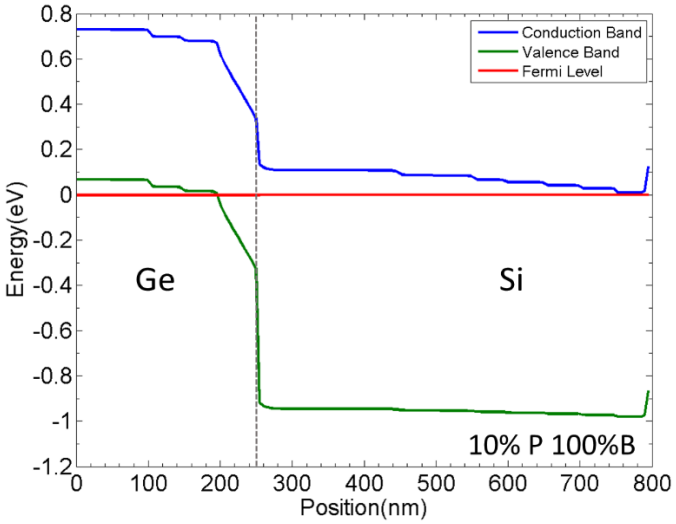

Figure 5.12 Simulated band structure using 100% activated B and 10% P, but without Ga from Figure 5.10.

To better understand the carrier transport properties of the NW, Figure 5.12 shows the simulated band structure alignment using dopant profiles of 100% B and 10% P, as measured from APT. The Fermi level is in the valence band on the Ge side due to the high level of *p*-type dopant, while it is under but close to the conduction band on the Si side. When the dopant level towards the catalyst increases to 10^{19} cm^{-3}, the Fermi level on the Si side gets closer to the conduction band. For a typical tunneling transistor, the Fermi level on Si side should be in the conduction band and it should be in the valence band on the Ge side across the Si-Ge interface. However, because the dopant level in Si near the SiGe interface is not high enough, the Fermi level near the SiGe interface is still in the forbidden band and electrons cannot easily tunnel through the interface. When the positive bias on Si is increased, the band structure on the Si side is lower and electrons can then tunnel from the Ge valence band to the Si conduction band. When negative bias is applied to Si, the

band structure on the Si side is higher so that electrons can move easily from the Si conduction band to the Ge conduction band.

In order to interpret the *in situ* EH biasing experiments, further simulations were done for a similar device structure, connecting the Si end to tungsten, forming a Schottky contact, and connecting Ge to an ohmic contact. Bias from -5V to +5V was then applied on the Si side, with the Ge side kept grounded. The simulated built-in potential profiles under bias are shown in Figures 5.13a and 5.13b, where Figure 5.13a uses active dopants of 100% P and 10% B, as measured from the APT results, and Figure 5.13b uses active dopants of 10% P and 100% B. In both cases, the simulated built-in potential offset increases as the applied positive bias increases, whereas it only decreases slightly under different negative bias. The built-in potential of the Ge intrinsic region increases to a smaller amount as positive bias is applied, whereas it only decreases slightly as negative bias is applied, which would cause the change of dip observed in Figure 5.9a. The slope in potential, moving from Ge (200 nm) to Si (250 nm), also increases under positive bias, whereas the slope of the potential decreases slightly under negative bias. Moreover, the depletion region and built-in potential change under negative bias is mostly distributed in the *i*-Ge region, from 200nm to 250nm. However, the distribution of depletion region and built-in potential change between the two cases is different under positive bias. In Figure 5.13a, because of the high dopant concentration of P in Si and relatively low concentration of B in Ge, most of the depletion region and built-in potential change is in part of the *p*-type Ge region and the *i*-Ge region, from 120 nm to 250 nm. There is only a very small built-in potential change region located at the *n*-type Si segment, from 250 to 270nm. On the other hand, in Figure 5.13b, there is a relative low concentration of P in Si and high concentration of B in Ge. The depletion

region and built-in potential change is mostly distributed at the *i*-Ge region and the *n*-type Si, from 200 nm to 320 nm. The experimental results in Figure 5.9a show that the potential goes up slightly on the Ge side from 200 to 250nm and the slope of the potential changing from 250 to 300nm also increases on the Si side under positive bias. Under negative bias, the potential on Ge side does not change, whereas the potential decreases slightly on the Si side. The depletion region change under negative bias is not obvious due to the complexity of the Si-Ge interface region discussed above. Considering the distribution of built-in potential change, Figure 5.13b gives a better fit to the experiment results, where the built in potential change is mostly located in the *i*-Ge and the Si segments (200nm-300nm), suggesting that there may be partial compensation of the P by Ga in the Si segment of the nanowire.

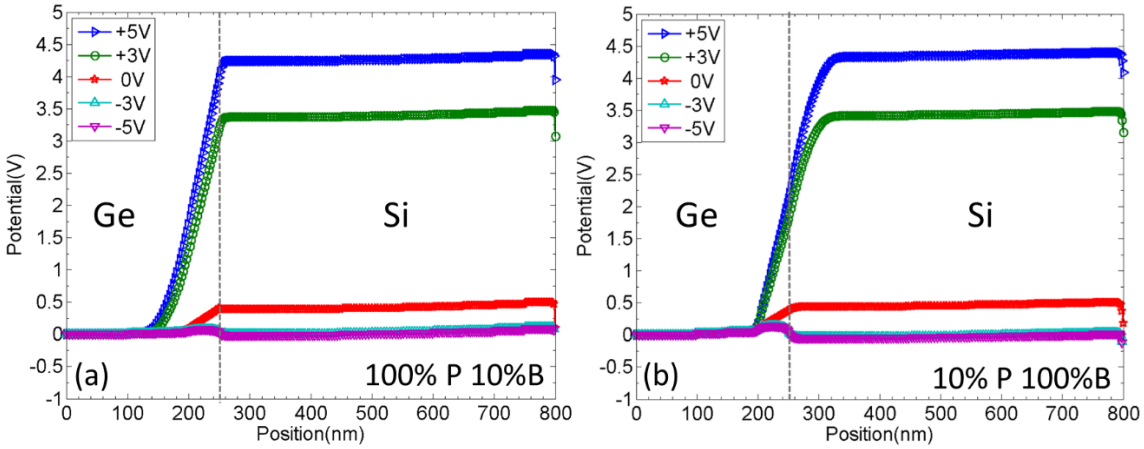

Figure 5.13 (a) Simulated built-in potential line profiles under different bias conditions, using 10% activated B and 100% P, but without Ga from Figure 5.10; (b) Simulated built-in potential line profiles under different bias conditions, using 100% activated B and 10% P, but without Ga from Figure 5.10.

With positive bias applied, the Schottky contact is in forward bias and has low resistance, while the Si-Ge heterojunction is in reverse bias and has high resistance. Thus, most of the positive voltage would be distributed across the Si-Ge heterojunction. The built-in potential offset across the heterojunction will increase as the bias increases. When the bias exceeds a certain value, the Si conduction band will become low enough. Thus, electrons from the Ge valence band can tunnel through the Si-Ge interface into the Si conduction band, giving a rectifying effect in the *IV* curve, as shown in Figure 5.9b. With negative bias, the Schottky contact is in reverse bias and has high resistance, while the Si-Ge heterojunction is in forward bias. The resistance of the heterojunction is low compared to the Schottky and ohmic contacts, and most of the negative voltage is distributed on the contacts. Therefore, the built-in potential offset across the heterojunction will be close to the one without bias and will not change much under different negative bias. Due to the high dopant level in Si near the catalyst, electrons can tunnel through the Schottky contact and thus there is still a rectifying effect due to the Si-Ge heterojunction, which is visible in the *IV* curve in Figure 5.9b. Therefore, the change of dip and nearby Ge segment, as well as the Si segment in Figure 5.9a, can be explained and the simulation results match well with the *in situ* holography biasing experiment.

5.4 Conclusions

Doped Si-Ge heterojunction NWs have been grown using the VLS method, and APT measurements were made to extract the B, P and Ga dopant concentrations as well as the Si, Ge composition profiles. The electrostatic potential profile measured by electron holography showed that the total potential offset across the Si-Ge heterojunction had the

value of 1.8±0.2V, with the Si side lower, whereas the built-in potential offset had the value of 0.4±0.2V, with the Ge side lower because of the difference in MIP between Ge and Si. Comparisons with simulations indicated that the Ga present in the Si region was, at most, only partially activated and that its effect could be ignored. The P and B active dopants could not be determined accurately due to noise from the irregular NW surface and insensitivity in the depletion region length because of the *i*-Ge region. *In situ* biasing experiments combined with electron holography were also performed. With positive bias on Si, most of the voltage was distributed across the Si-Ge heterojunction and its built-in potential increased to the same amount as the applied bias, whereas most of the voltage was distributed on the contacts with negative bias on Si and the built-in potential across the heterojunction was not changed much. Comparisons between biasing EH results and simulations indicated that the B dopant in Ge is mostly activated but not the P dopant in Si, possibly due to partial compensation by Ga in the Si region. The $I-V$ characteristic curve was measured and could also be explained using simulations. Overall, these results demonstrated that off-axis electron holography, APT and TCAD simulations provide a powerful combination for understanding the electrically active dopant distributions in doped NW device heterostructures.

References

[1] Z. Gan, D. Perea, J. Yoo, Y. He, R. Colby, B. Barker, M. Gu, S. Mao, C. Wang, S. Tom Picraux, D. Smith, and M. McCartney, Unpublished (2015).

[2] M. S. Gudiksen, L. J. Lauhon, J. Wang, D. C. Smith, and C. M. Lieber, Nature **415** 617 (2002).

[3] S. M. Sze, Physics of semiconductor devices, 2nd ed. Wiley, New York, (1981).

[4] V. Schmidt, H. Riel, S. Senz, S. Karg, W. Riess, and U. Gosele, Small **2** 85 (2006).

[5] J. Goldberger, A. I. Hochbaum, R. Fan, and P. Yang, Nano letters **6** 973 (2006).

[6] D. E. Perea, N. Li, R. M. Dickerson, A. Misra, and S. T. Picraux, Nano letters **11** 3117 (2011).

[7] C. Y. Wen, M. C. Reuter, J. Bruley, J. Tersoff, S. Kodambaka, E. A. Stach, and F. M. Ross, Science **326** 1247 (2009).

[8] L. Chen, W. Y. Fung, and W. Lu, Nano letters **13** 5521 (2013).

[9] D. E. Perea, E. Wijaya, J. L. Lensch-Falk, E. R. Hemesath, and L. J. Lauhon, Journal of Solid State Chemistry **181** 1642 (2008).

[10] D. E. Perea, E. R. Hemesath, E. J. Schwalbach, J. L. Lensch-Falk, P. W. Voorhees, and L. J. Lauhon, Nature nanotechnology **4** 315 (2009).

[11] M. R. McCartney and D. J. Smith, Annual Review of Materials Research **37** 729 (2007).

[12] M. R. McCartney, N. Agarwal, S. Chung, D. A. Cullen, M.-G. Han, K. He, L. Li, H. Wang, L. Zhou, and D. J. Smith, Ultramicroscopy **110** 375 (2010).

[13] Z. Gan, D. E. Perea, J. Yoo, S. Tom Picraux, D. J. Smith, and M. R. McCartney, Applied Physics Letters **103** 153108 (2013).

[14] L. Li, Z. Gan, M. R. McCartney, H. Liang, H. Yu, W. J. Yin, Y. Yan, Y. Gao, J. Wang, and D. J. Smith, Adv Mater **26** 1052 (2014).

[15] M. I. den Hertog, H. Schmid, D. Cooper, J. L. Rouviere, M. T. Bjork, H. Riel, P. Rivallin, S. Karg, and W. Riess, Nano letters **9** 3837 (2009).

[16] N. Li, T. Y. Tan, and U. Gösele, Applied Physics A **90** 591 (2008).

[17] S. A. Dayeh, J. Wang, N. Li, J. Y. Huang, A. V. Gin, and S. T. Picraux, Nano letters **11** 4200 (2011).

[18] S. A. Dayeh, N. H. Mack, J. Y. Huang, and S. T. Picraux, Applied Physics Letters **99** 023102 (2011).

[19] J. E. Allen, E. R. Hemesath, D. E. Perea, J. L. Lensch-Falk, Z. Y. Li, F. Yin, M. H. Gass, P. Wang, A. L. Bleloch, R. E. Palmer, and L. J. Lauhon, Nature nanotechnology **3** 168 (2008).

[20] M. J. Hytch, E. Snoeck, and R. Kilaas, Ultramicroscopy **74** 131 (1998).

[21] J. Li, M. R. McCartney, R. E. Dunin-Borkowski, and D. J. Smith, Acta Crystallographica Section A **55** 652 (1999).

[22] J. Li, M. R. McCartney, and D. J. Smith, Ultramicroscopy **94** 149 (2003).

[23] F. A. Trumbore, Bell System Technical Journal **39** 205 (1960).

[24] T. Hoshikawa, X. Huang, K. Hoshikawa, and S. Uda, Japanese Journal of Applied Physics **47** 8691 (2008).

[25] K. B. Wolfstirn, Journal of Physics and Chemistry of Solids **16** 279 (1960).

[26] N. Sclar, Electron Devices, IEEE Transactions on **24** 709 (1977).

CHAPTER 6

CHARACTERIZATION OF TRAPPED CHARGES IN Ge/Li_xGe CORE/SHELL STRUCTURE DURING LITHIATION USING OFF-AXIS ELECTRON HOLOGRAPHY

This chapter describes the lithiation of Ge nanowires (NWs) and the measurement of trapped charges in Ge/Li_xGe core/shell NWs using off-axis electron holography. The Ge NWs were grown using the vapor-liquid-solid (VLS) method, and were provided by Chongmin Wang and Meng Gu from Pacific Northwest National Laboratory. My contribution to this work has included characterization of the NW lithiation process, measurement of electrostatic profiles across the core/shell structures, and simulations for estimation of the trapped charge.

6.1 Introduction

Lithium ion batteries (LIBs) have important applications as energy-storage systems for portable electronics, electric vehicles, and sources of renewable energy such as wind and solar [1,2]. Graphite is currently used as the anode material in commercial LIBs. However, graphite has a limited theoretical capacity of 372 $mAhg^{-1}$ and it cannot meet the growing demands for high energy density and long life-time [3,4]. Novel materials such as other group IV materials (Si, Ge and Sn), with higher theoretical capacities, are being considered as possible alternatives [3]. Si has received most attention because of its greatest theoretical capacity of 3579 $mAhg^{-1}$ and 8334AhL^{-1} for $Li_{15}Si_4$ at room temperature, as well as its abundance [5,6]. Relative to Si, Ge has lower theoretical capacities of 1384

$mAhg^{-1}$ and 7366 AhL^{-1} for $Li_{15}Ge_4$ at room temperature, and it is more expensive [3,7]. However, Ge has higher intrinsic electronic conductivity because of its smaller band gap (0.6eV) compared to Si (1.1eV) [8]. Moreover, the Li ion diffusivity in Ge is about two times larger, compared to Si [9,10]. Thus, Ge has high charging/discharging rates in LIBs, compared to Si, which is also an important consideration for LIB applications. Despite these advantages, a major drawback of using Si or Ge is the huge volume change upon full lithiation/delithiation (281% for Si and 246% for Ge), which may lead to degradation of electrodes and the solid electrolyte interface (SEI), causing irreversible loss of LIB capacity [11-15]. Nanostructures have been developed to accommodate the strain during lithiation and to increase rate capability by shortening the Li ion diffusion length [16-18].

In situ transmission electron microscopy (TEM) has been used to characterize the microstructure and phase transition behavior during lithiation/delithiation for several materials, including Si, Ge and Sn, by using open cell structures with liquid or solid electrolytes [11,14,19-23]. Two-step phase transformation: c-Ge(Si)→a-Li_xGe(Li_xSi)→c-$Li_{15}Ge_4$($Li_{15}Si_4$) has been observed during Ge (Si) lithiation [11,20,22]. Anisotropic lithiation was observed for different growth directions in Si, whereas isotropic lithiation was observed in Ge [11,14]. Amorphous Li_xGe(Si) and crystal Ge(Si) interfaces have been studied during lithiation to understand the lithiation mechanism with atomic-scale resolution [19,21,24]. Simulations have also been performed to prove that extra electrons in Si near the Li_xSi-Si interface drive the solid-state amorphization of Li-Si alloy [25]. Knowledge of the charge distribution during lithiation is important for developing a better understanding of the lithiation mechanism and the associated electrochemistry. Off-axis

electron holography has been used to characterize the charge distribution across the Ge/ Li_xGe core/shell nanowire during the lithiation process.

6.2 Experimental Details

The Ge NWs were grown along [111] directions on Ge substrates. After growth, one Ge NW was attached to a Pt tip using silver glue and Li metal was attached to a second Pt tip. Both were then installed in a Nanofactory^{TM} STM holder for the *in situ* lithiation experiments. Before insertion into the TEM column, the STM holder was exposed to air for a few seconds, and a Li_2O layer was formed on the Li metal surface, which would act as a solid electrolyte during lithiation. The Ge NW was moved to make physical contact with the Li source, forming an open cell battery structure, as illustrated in Figure 6.1. A bias of ~-2V was applied to the Ge NW, while the Li metal was kept grounded during the lithiation process. The electron holography experiments were performed using an FEI Titan 80-300, which was operated at 300keV and equipped with field emission gun, probe corrector, biprism, Lorentz lens and Quantum EELS spectrometer. For the holography experiments, the objective lens was switched off, and the Lorentz mini lens was used to obtain a larger field of view. The typical biprism voltage was 120V and the hologram exposure time was 2s.

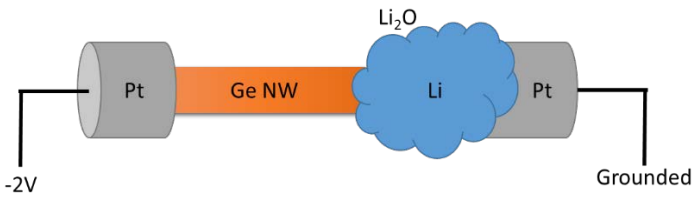

Figure 6.1 Schematic diagram of setup used for *in situ* observations of the Ge NW lithiation process.

6.3 Results and Discussions

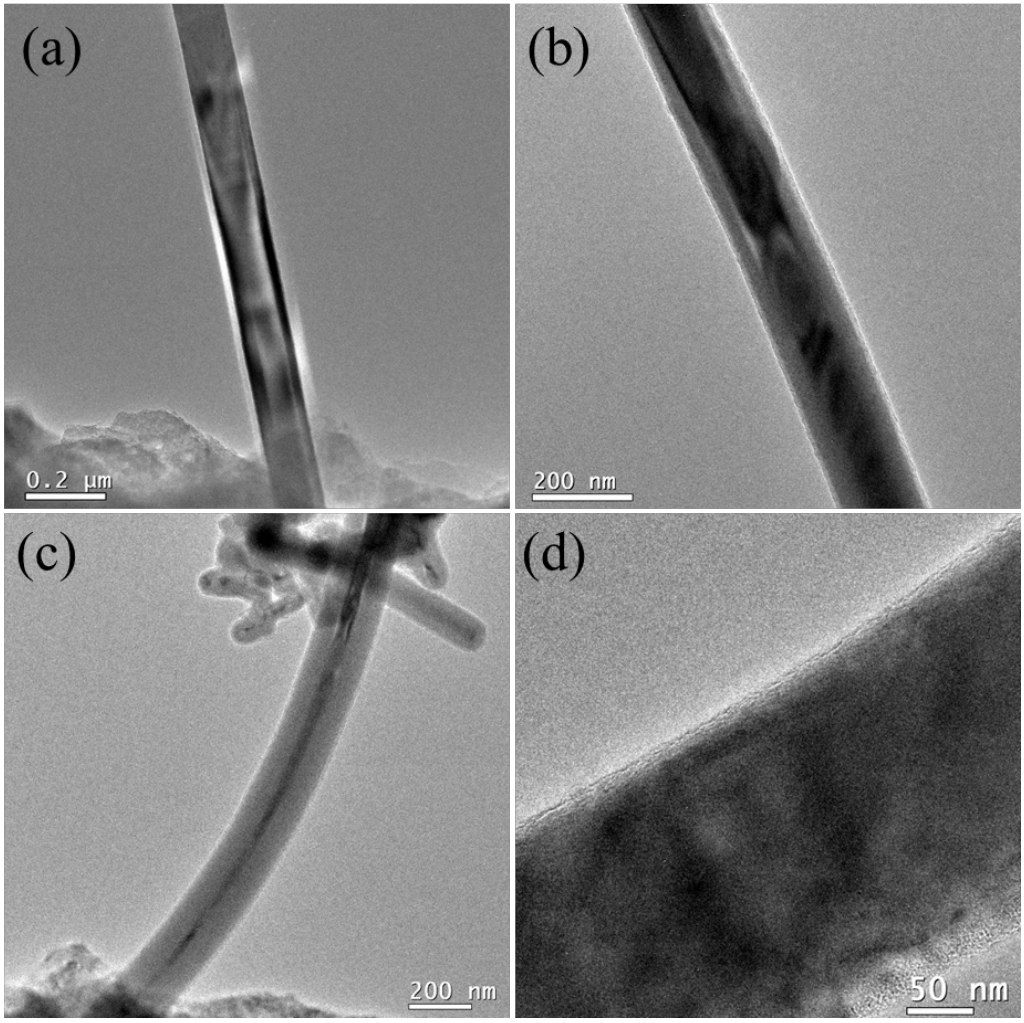

Figure 6.2 TEM images of Ge NW during lithiation process: (a) Before lithiation; (b) Formation of Ge/Li_xGe core/shell structure; (c) The shell part grew while the core part shrank; (d) At the end of lithiation, when polycrystalline Li_xGe has been formed.

Figure 6.2 shows TEM images of the Ge NW during lithiation. Figure 6.2a shows the Ge NW in contact with the Li metal. Application of -2V bias causes Li_2O to diffuse onto the Ge NW surface as the solid electrolyte. Figure 6.2b shows that Li ions diffused into the Ge NW surface, forming a crystalline Ge/amorphous Li_xGe core/shell structure. As

lithiation continued, the shell became thicker, while the core region shrank. The total volume of the NW increased, as clearly visible in Figure 6.2c, and the core decreased to a small size. At the end of the lithiation, the Ge core disappeared completely and the NW became polycrystalline, as shown in Figure 6.2d.

Figure 6.3 shows STEM HAADF and EELS mapping of Ge/Li_xGe core/shell structure, which were recorded immediately after Figure 6.1b. These results indicate the distribution of Li at the shell and confirm the expected core/shell structure.

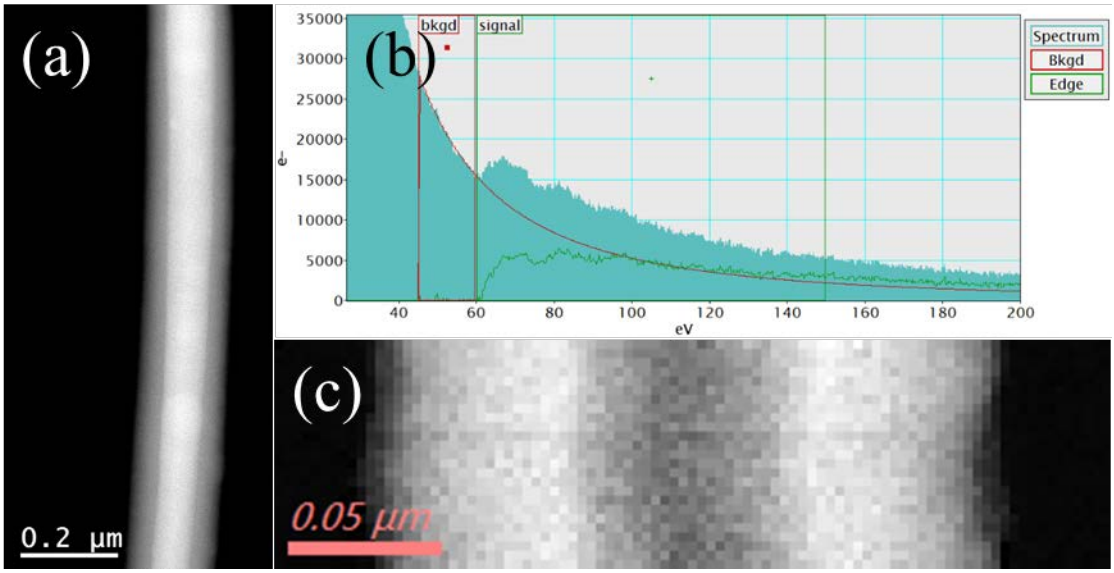

Figure 6.3 EELS mapping of Ge/Li_xGe core/shell structure: (a) STEM HAADF image; (b) EELS spectrum showing the presence of Li; (c) Li mapping of core/shell structure.

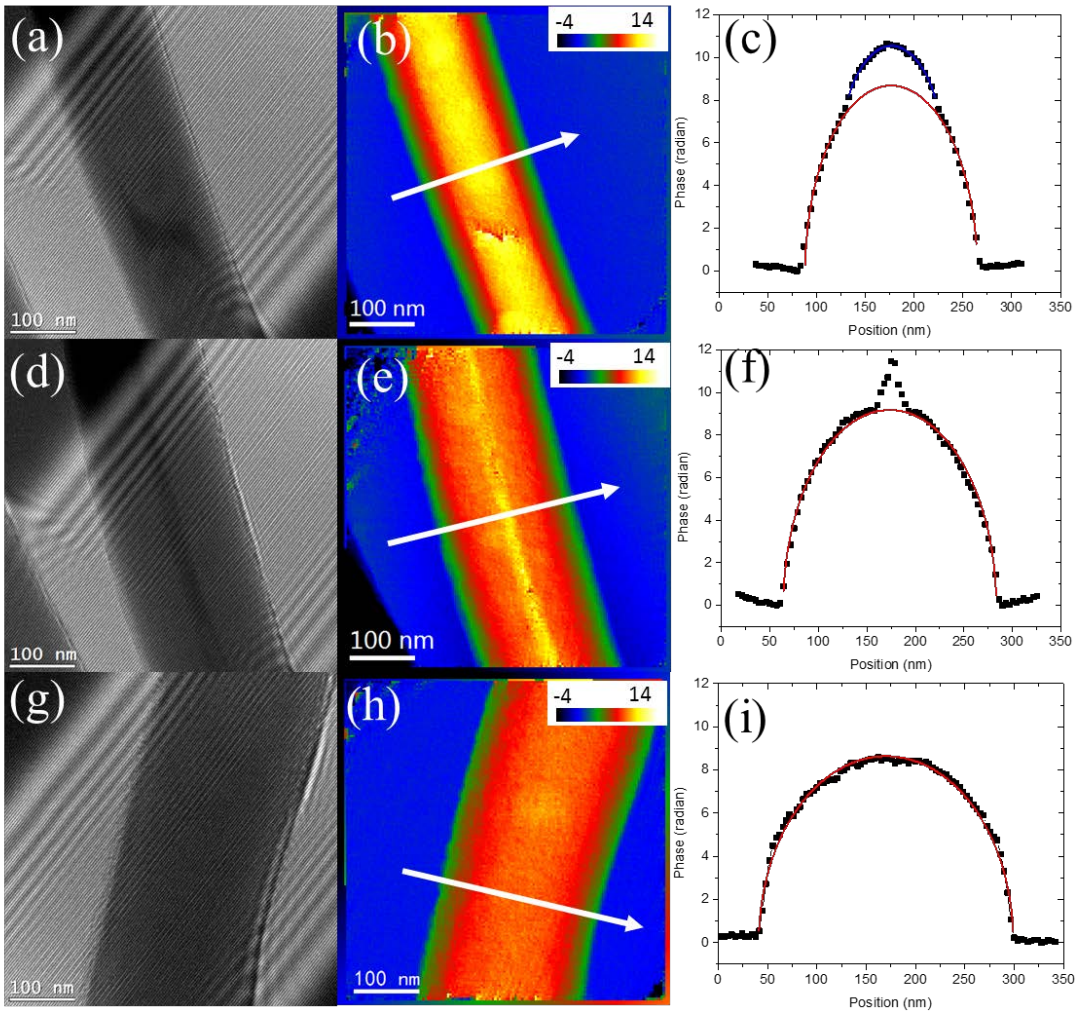

Figure 6.4 Electron holography observations of Ge/Li_xGe core/shell NW during lithiation: (a), (d) and (g) Holograms of NW; (b), (e) and (h) Corresponding reconstructed phase images, shown in pseudo-color (scale bar shown at top right in units of radian); (c), (f) and (i) Phase profiles along the white arrows in (b), (e) and (h), respectively.

Electron holography observations were made during the lithiation process. Figures 6.4a, 6.4d and 6.4g show holograms taken at about the same time as Figures 6.2b, 6.2c and 6.2d, respectively. Figures 6.4b, 6.4e and 6.4h are the corresponding reconstructed phase images, using pseudo-color to show the change of phase. The color scale bars are shown

at top right. The center part of the NW has higher phase compared to the outer parts, which is due to the combination of greater thickness and higher mean inner potential of crystalline Ge, compared to Li_xGe. Phase profiles were extracted along the white arrows in the reconstructed phase images and shown at the right. The Ge core in Figure 6.4c is about half the diameter of the NW, and both the core and shell parts mimic a cylindrical NW shape. In Figure 6.4f, the Ge core has shrunk to a smaller size and it is apparently faceted, as shown by the triangular shape at the center. The Li_xGe shell part has a round cross section. In Figure 6.4h, the entire Ge NW has been lithiated, the Ge core has disappeared, and the lithiated Li_xGe ($x\sim3.75$) NW again mimics a cylindrical NW shape. During this process, the NW diameter has increased from 180nm in Figure 6.4c, to 250nm in Figure 6.4i.

The phase profiles across the NW will be caused by the mean inner potential of the materials as well as any built-in potential. To interpret the phase profiles, it is first assumed that there are initially no trapped charges in the NW and that the phase shift is due only to mean inner potential V_{shell} and change of thickness. A model including trapped charges is discussed further below. Assuming that the NW has a cylindrical shape, then the phase shift due to the shell part can be calculated and compared with the experimental results, as shown by the red curves in Figure 6.4c, 6.4f and 6.4i. From the fitting for the best fitted V_{shell}, it seems that a cylindrical NW shape fits reasonably well with the experimental results. The best fitted values of V_{shell} for these three stages of lithiation are shown in table 6.1. As the lithiation continued, the mean inner potential of V_{shell} decreased from 7.6V to 5.1V. This drop would indicate that the Li component in the shell has increased during lithiation, because Li is a lighter element and has smaller mean inner potential, compared to Ge. The bias applied to the NW should not affect this conclusion since the bias was kept

fixed at -2V. Similar fitting was applied for the core part in Figure 6.4c, as shown by the blue curve. This model also closely fits with the experimental data. However, the best fitted V_{core} is only 10.6 ± 0.1V, compared to the value of 14.3V for crystalline Ge in the literature [26]. This difference suggests the possibility that charges are trapped in the NW during the lithiation.

Table 6.1 Measured potential of the Li_xGe shell.

Number	V_{shell} (V)
1	7.6±0.1
2	6.4±0.1
3	5.1±0.1

In order to determine the amount of trapped charge in the NW, a variety of models were proposed, including (a) sheet electrons at the Ge core surface and sheet positive charges at the inner shell surface; (b) bulk electrons at the Ge core and sheet positive charges at the inner shell surface; (c) sheet electrons at the Ge core surface and sheet positive charges at the outer shell surface; (d) bulk electrons at the Ge core and sheet positive charges at the outer shell surface; (e) sheet electrons at the Ge core surface and bulk positive charges at the shell; (f) bulk electrons at the Ge core and bulk positive charges at the shell. The best fitting model is shown in Figure 6.5a. This model assumed that Li^+ ions had accumulated in the Li_2O layer on the NW surface, while electrons were uniformly trapped in the Ge core. Using this model, the built-in potential in the NW could then be calculated using the Poisson's equation. Because there is no information in the literature about the permittivity of Li_xGe, the value for Ge (16) was used in the calculation. The calculated phase shift φ_{cal} is due to the combination of built-in potential and mean inner potential, and can be calculated using Equation 6.1. The values of the electron density ρ in

the Ge core and V_{shell} were systematically varied until the average error $\overline{(\varphi_{cal} - \varphi_{exp})^2}$ reached a minimum, where φ_{exp} represents the experimental data. The mean inner potential for Ge was set to be constant at 14.3V during the fitting process. The final result of the fitting is shown by the red curve in Figure 6.5b. The best results are:

$$\rho = 3 \times 10^{18}\ \text{electrons/cm}^3\ ;\ V_{shell} = 8.4V \tag{6.2}$$

The RMS error for the fitting is 0.4 radian.

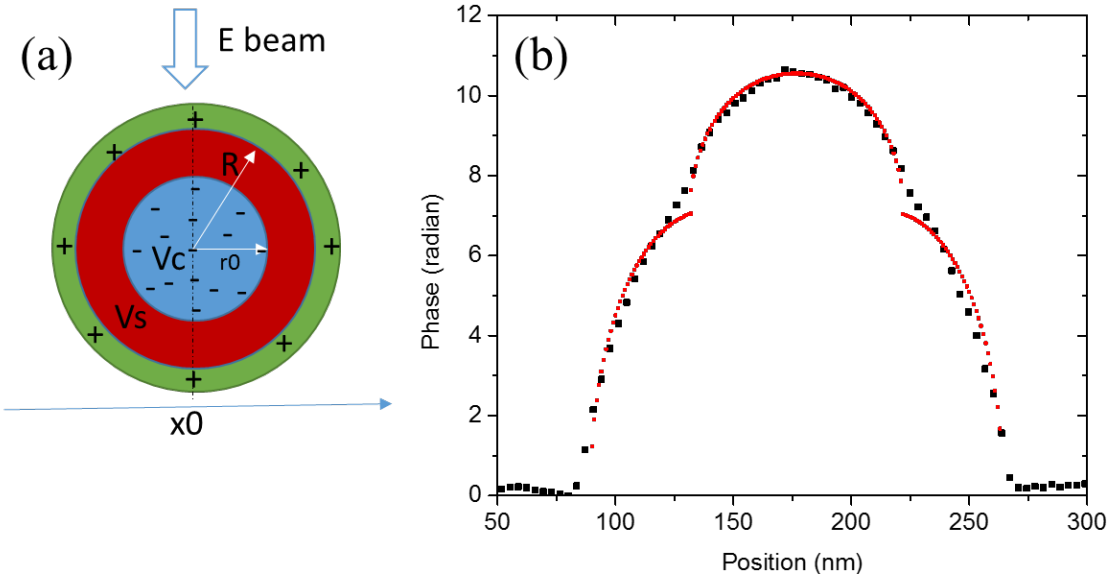

Figure 6.5 Model for trapped charges in Ge/Li_xGe core/shell structure: (a) Schematic diagram of the model; (b) Experimental data (black) and best fitted results (red).

Using the fitted charge density, the built-in potential distribution across the core/shell structure can be plotted, as shown in Figure 6.6a, using pseudo-color to show the change of potential. A potential profile is also extracted along the y=0 axis and shown in Figure 6.6b. This profile indicates that there is ~-2V potential difference between the shell and the surface of the core, which fits with the bias experiment conditions. Extra electrons are

accumulated at the Ge core and thus reduced the measured total potential. The apparent lower value of the mean inner potential described earlier can therefore be explained.

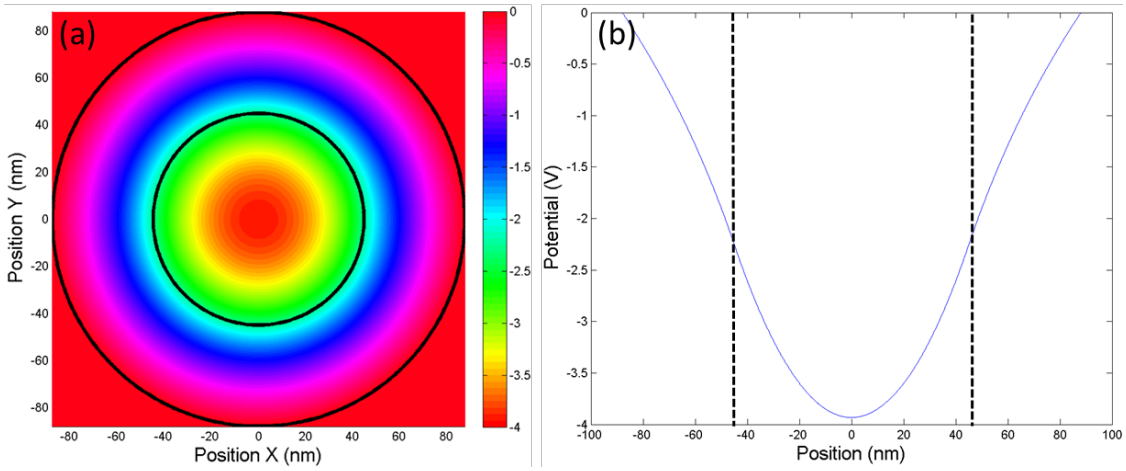

Figure 6.6 Simulation of potential distribution in Ge/Li_xGe core/shell NW: (a) Potential distribution in NW cross section, shown in pseudo-color with scale bar on the right in units of V; (b) Potential profile along Y=0 in (a).

The amount of Li (x) in the Li_xGe shell can also be estimated by using the volume ratio and measured mean inner potential. The proposed equation is described below:

$$\frac{x \cdot V_{Li} + V_{Ge}}{V_{Ge}} \cdot \left(\frac{Vol_{Ge}}{Vol_{Li_xGe}} \right) = \frac{V_{Li_xGe}}{V_{Ge}} \tag{6.1}$$

where V_{Ge} and V_{LixGe} are the mean inner potentials for crystal Ge and Li_xGe, respectively, Vol_{Ge} and Vol_{LixGe} are the volumes for Ge and Li_xGe, respectively, and V_{Li} is the mean inner potential changed when one Li atom is added to Ge and the total volume is unchanged. This equation also assumes that the MIP for Ge does not change during phase change.

The measured radius for core and the whole NW are shown in table 6.2, where case A is before lithiation, case B, C and D are at the time corresponding to Figure 6.4a, 6.4d and 6.4g, respectively. The case D at Figure 6.4g is used for calibration, where x is

approximated to be 3.75 for the fully lithiated phase and the volume ratio $\frac{Vol_{Ge}}{Vol_{Li_xGe}}$ was calculated to be 0.13. The value for V_{Li} is then calculated to be 6.27V, using 14.3V MIP for crystal Ge [26] and Equation 6.1. Since the core disappeared, there should be no trapped charge in the NW structure, which might influence the result.

Table 6.2 Measured radius for NW core and whole NW.

Case	Core (nm)	Whole NW (nm)
A	-	66
B	45	88
C	-	110
D	-	129

After the calibration, the amount of Li x in Li_xGe can be calculated, again using Equation 6.1. For case B at Figure 6.4a, the x in the NW shell is calculated to be 2.4 for the measured MIP of 7.6V, where the effect of trapped charge was ignored, while x is calculated to be 2.9 for the measured MIP of 8.4V, where effect of trapped charge was included by using the best fitted model discussed above. These results indicate that the intermediate lithiated state for NW shell is Li_xGe, where x is significantly lower than 3.75. As the lithiation process continued, more Li might be diffused into the Li_xGe shell structure and thus x was increased until it reached 3.75 and the NW was fully lithiated. The case C cannot be calculated to confirm this result because the core is faceted and its cross section area cannot be calculated. Further experiments and other methods might be necessary for further investigation.

6.4 Conclusions

A Ge NW was lithiated *in situ* by applying 2V bias between its two ends, and TEM, STEM and EELS were used to characterize the changes in the Ge/Li_xGe core/shell structure. Electron holograms were taken during the lithiation process to determine the charge distribution inside the NW. The mean inner potential for Li_xGe decreased during the process, due to an increase of the Li content in the shell. Lower potential at the Ge core was also discovered, and attributed to accumulation of trapped charge. A model was proposed to explain the lower measured Ge potential, and the amount of trapped charge in the Ge core was calculated to be 3×10^{18} electrons/cm^3. The amount of Li during lithiation was calculated using MIP and volume ratio. It suggests that the Li amount in Li_xGe during lithiation might be lower than the fully lithiated phase and increased during the lithiation process.

References

[1] M. Armand and J. M. Tarascon, Nature **451** 652 (2008).

[2] A. S. Arico, P. Bruce, B. Scrosati, J.-M. Tarascon, and W. van Schalkwijk, Nature materials **4** 366 (2005).

[3] D. Larcher, S. Beattie, M. Morcrette, K. Edstrom, J.-C. Jumas, and J.-M. Tarascon, Journal of Materials Chemistry **17** 3759 (2007).

[4] Y.-M. Chiang, Science **330** 1485 (2010).

[5] M. N. Obrovac and L. Christensen, Electrochemical and Solid-State Letters **7** A93 (2004).

[6] M. N. Obrovac and L. J. Krause, Journal of The Electrochemical Society **154** A103 (2007).

[7] L. Baggetto and P. H. L. Notten, Journal of The Electrochemical Society **156** A169 (2009).

[8] S. M. Sze, Physics of semiconductor devices, 2nd ed. Wiley, New York, (1981).

[9] C. Fuller and J. Severiens, Physical Review **96** 21 (1954).

[10] J. Graetz, C. C. Ahn, R. Yazami, and B. Fultz, Journal of The Electrochemical Society **151** A698 (2004).

[11] X. H. Liu, Y. Liu, A. Kushima, S. Zhang, T. Zhu, J. Li, and J. Y. Huang, Advanced Energy Materials **2** 722 (2012).

[12] L. Y. Beaulieu, K. W. Eberman, R. L. Turner, L. J. Krause, and J. R. Dahn, Electrochemical and Solid-State Letters **4** A137 (2001).

[13] C. K. Chan, H. Peng, G. Liu, K. McIlwrath, X. F. Zhang, R. A. Huggins, and Y. Cui, Nat Nano **3** 31 (2008).

[14] X. H. Liu, H. Zheng, L. Zhong, S. Huang, K. Karki, L. Q. Zhang, Y. Liu, A. Kushima, W. T. Liang, J. W. Wang, J. H. Cho, E. Epstein, S. A. Dayeh, S. T. Picraux, T. Zhu, J. Li, J. P. Sullivan, J. Cumings, C. Wang, S. X. Mao, Z. Z. Ye, S. Zhang, and J. Y. Huang, Nano letters **11** 3312 (2011).

[15] B. Key, R. Bhattacharyya, M. Morcrette, V. Seznéc, J.-M. Tarascon, and C. P. Grey, J Am Chem Soc **131** 9239 (2009).

[16] P. G. Bruce, B. Scrosati, and J.-M. Tarascon, Angewandte Chemie International Edition **47** 2930 (2008).

[17] L. Ji, Z. Lin, M. Alcoutlabi, and X. Zhang, Energy & Environmental Science **4** 2682 (2011).

[18] H. Wu and Y. Cui, Nano Today **7** 414 (2012).

[19] X. H. Liu, J. W. Wang, S. Huang, F. Fan, X. Huang, Y. Liu, S. Krylyuk, J. Yoo, S. A. Dayeh, A. V. Davydov, S. X. Mao, S. T. Picraux, S. Zhang, J. Li, T. Zhu, and J. Y. Huang, Nature nanotechnology **7** 749 (2012).

[20] X. H. Liu, L. Q. Zhang, L. Zhong, Y. Liu, H. Zheng, J. W. Wang, J. H. Cho, S. A. Dayeh, S. T. Picraux, J. P. Sullivan, S. X. Mao, Z. Z. Ye, and J. Y. Huang, Nano letters **11** 2251 (2011).

[21] Y. Liu, X. H. Liu, B. M. Nguyen, J. Yoo, J. P. Sullivan, S. T. Picraux, J. Y. Huang, and S. A. Dayeh, Nano letters **13** 4876 (2013).

[22] X. H. Liu and J. Y. Huang, Energy & Environmental Science **4** 3844 (2011).

[23] X. H. Liu, S. Huang, S. T. Picraux, J. Li, T. Zhu, and J. Y. Huang, Nano letters **11** 3991 (2011).

[24] Y. Liu, S. Zhang, and T. Zhu, ChemElectroChem **1** 706 (2014).

[25] M. Gu, H. Yang, D. E. Perea, J. G. Zhang, S. Zhang, and C. M. Wang, Nano letters **14** 4622 (2014).

[26] J. Li, M. R. McCartney, R. E. Dunin-Borkowski, and D. J. Smith, Acta Crystallographica Section A **55** 652 (1999).

CHAPTER 7

SUMMARY AND FUTURE WORK

7.1 Summary

The research of this dissertation has involved quantitative analysis of electrostatic potential profiles and charge distributions in semiconductor nanostructures using off-axis electron holography.

ZnO nanowires (NWs) and thin films have been investigated. The mean inner potential (MIP) and inelastic mean free path (IMFP) of ZnO has been measured using ZnO NWs. The MIP at 200keV was measured to be 15.3V±0.2V and the IMFP was measured to be 55±3nm. The measured MIP agreed closely with the value reported in the literature. The MIP and IMFP values were then used to measure the thickness of a ZnO nano-sheet and gave consistent results for thicknesses in the range of 14nm-18nm.

ZnTe thin films have also been studied. The MIP was measured using intrinsic ZnTe thin films and convergent beam electron diffraction (CBED). The MIP at 200keV was measured to be 13.7±0.6V and the IMFP was measured to be 46±2nm. The MIP measurement matched the value obtained by calculations. The measured MIP and IMFP were then used to study a ZnTe thin film expected to have a *p-n* junction. However, no change in signal due to built-in potential was observed across a junction. Possible reasons might be: (a) the Al dopants were not activated; or (b) the junction was outside the field of view of the holography experiment. Dynamical effects were systematically studied using Bloch wave simulations. Thinner samples, avoiding low-index zone axes and careful sample tilting will all help to minimize these effects.

Si NWs with axial *p*-*n* junctions and Schottky junction were investigated [1]. The Schottky junctions were formed at the end of the NW due to the presence of Au catalyst particles. The electrostatic potential profile measured by electron holography showed that the built-in potentials across the *p*-*n* junction and the Schottky junction, had values of 1.0±0.3V and 0.5±0.3V, respectively. Simulations indicated that the dopant concentrations were ~10^{19}cm^{-3} for donors and ~10^{17} cm^{-3} for acceptors. The positively charged Au particle at the end of the grounded NW had to be considered in order to account for the lower work function in the simulation. The effects of a possible transition region forming an n^+-n^--*p* junction, and possible surface charge, were also systematically studied using simulations.

Doped Si-Ge heterojunction NWs were investigated using off-axis electron holography, while atom probe tomography (APT) measurements were made to extract the B, P and Ga dopant concentrations as well as the Si, Ge composition profiles [2]. The electrostatic potential profile measured by holography showed that the total potential offset across the Si-Ge heterojunction had the value of 1.8±0.2V, with the Si side lower, whereas the built-in potential offset had the value of 0.4±0.2V, with the Ge side lower because of the difference in MIP between Ge and Si. Comparisons with simulations indicated that the Ga dopant present in the Si was, at most, only partially activated and that its effect could be ignored. The P and B active dopants could not be determined accurately due to noise from the irregular NW surface and insensitivity in the depletion region length because of the *i*-Ge region. *In situ* biasing experiments combined with electron holography were also performed. With positive bias on Si, most voltage was distributed across the Si-Ge heterojunction and its built-in potential increased to the same amount as the applied bias, whereas most of the voltage was distributed on the contacts with negative bias on Si and

the built-in potential across the heterojunction was not much changed. Comparisons between EH biasing results and simulations indicated that the B dopant in Ge was mostly activated but not the P dopant in Si, possibly due to partial compensation by Ga in the Si region. The $I-V$ characteristic curve was measured and could also be explained using simulations.

Ge/Li_xGe core/shell structures were studied during lithiation using S/TEM, EELS and holography. The Ge NW was lithiated *in situ* by applying 2V bias between the two ends. Electron holograms were taken during the lithiation process to determine the charge distribution inside the NW. The MIP for Li_xGe decreased during the process, due to an increase of the Li content in the shell. Lower potential at the Ge core was also discovered, and attributed to accumulation of trapped charge. A model was proposed to explain the lower measured Ge potential, and the amount of trapped electrons in the Ge core was calculated to be 3×10^{18} electrons/cm^3. The amount of Li during lithiation was calculated using MIP values and the volume ratio. The results suggest that the amount of Li in Li_xGe during lithiation might be lower than the fully lithiated phase but increased during the lithiation process.

Overall, this dissertation research has reiterated that off-axis electron holography is an effective technique for quantitative characterization of nanostructure thickness and electrostatic potential profiles with nanoscale resolution. Combining electron holography and simulations provides information about electrically active dopant and trapped charge distributions in semiconductor nanostructures, which are important for understanding electrical mechanisms and for developing future semiconductor devices. Moreover, electron holography coupled with *in situ* biasing can be used to characterize devices under

working conditions and to extract information which is not shown under unbiased conditions.

7.2 Remarks on Possible Future Work

This dissertation research has clearly demonstrated that electron holography is an effective technique for quantitative characterization of built-in potential, and active dopants, as well as trapped charges, with nanoscale resolution. However, electron holography only gives two-dimensional projected-phase information about the sample. Uniform composition and built-in potential distributions in the sample along the electron beam direction were assumed in this dissertation research for calculations of active dopant concentration. For semiconductor devices, the built-in potential may vary along the beam direction due to surface effects or inhomogeneous dopant distributions. Therefore, it is important to obtain three-dimensional phase information and hence the built-in potential distribution in order to make accurate measurements of dopant amounts.

This problem can be solved by taking holograms at different tilt angles and using tomographic reconstruction [3]. 3-D holography characterization of Si thin films with *p*-*n* junctions has been reported [4], and it was found that the surface active dopant concentrations were lower, whereas the central ones were very close, compared to bulk material. NWs have a large surface-to-volume ratio and the surface may play an important role in overall dopant distributions. A preliminary tomography experiment has been performed on Si-Ge axial heterojunction NWs using HAADF STEM tilt image series, as shown in Figure 7.1. The tilt series were taken using FEI Titan G2 80-300 operated at 300kV. The sample was tilted from -70˚ to 70˚ and the HAADF images were taken every

2˚. Figure 7.1a shows a typical image that was taken at 0˚ tilt angle. The intensity from HAADF image is directly related to the atomic number and thickness of the sample, and therefore it satisfies the tomography reconstruction requirements. The data was reconstructed by INSPECT3D^{TM} using the simultaneous iterative reconstruction technique (SIRT) algorithm with 20 iterations. The result is shown in Figure 7.1b, using pseudo-color to show the change of intensity, and the cross section of the NW is shown in Figure 7.1c. From the HAADF image tomography reconstruction, the composition distribution is almost uniform in cross section and the NW grown along <111> direction has a hexagonal cross section. However, the HAADF image is not sensitive to the dopant concentrations nor the built-in potential. Further tomographic holography experiments are necessary so that the three-dimensional phase as well as the built-in potential distribution can be extracted. The active dopants in all three dimensions could thus be determined by comparison with simulations.

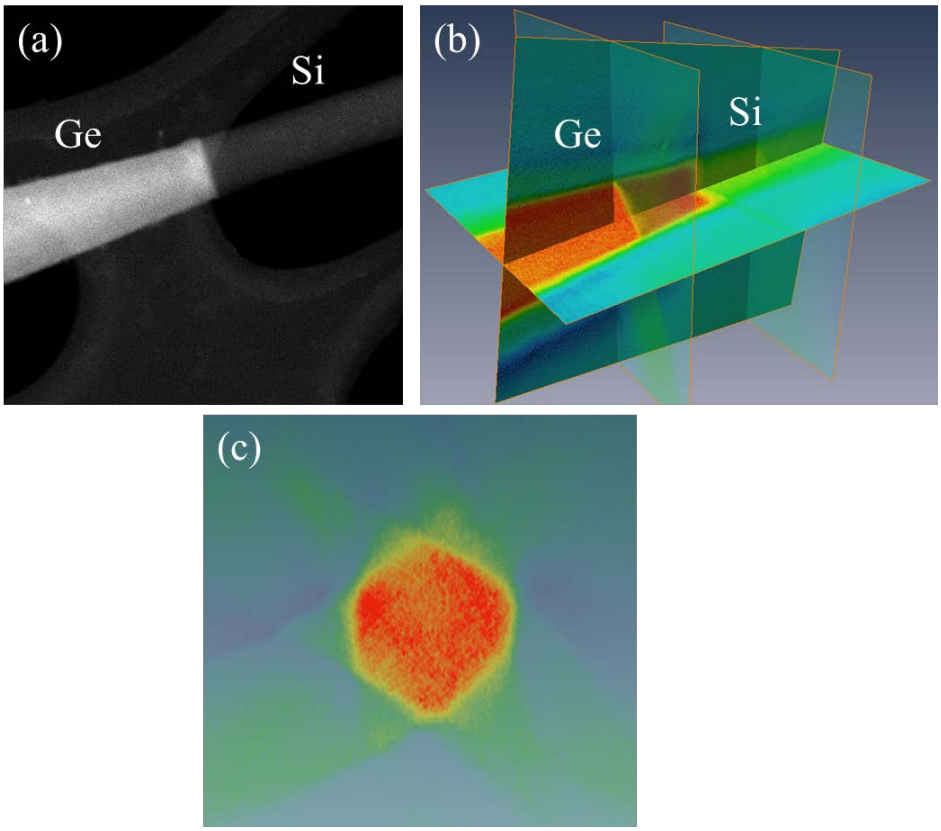

Figure 7.1 Tomography of Si-Ge NWs: (a) HAADF image at 0˚ tilt; (b) Tomography reconstruction result shown in pseudo color; (c) Cross section of NW.

References

[1] Z. Gan, D. E. Perea, J. Yoo, S. Tom Picraux, D. J. Smith, and M. R. McCartney, Applied Physics Letters **103** 153108 (2013).

[2] Z. Gan, D. Perea, J. Yoo, Y. He, R. Colby, B. Barker, M. Gu, S. Mao, C. Wang, S. Tom Picraux, D. J. Smith, and M. R. McCartney, submitted (2015).

[3] J. Frank, Electron tomography : three-dimensional imaging with the transmission electron microscope. Plenum Press, New York, (1992).

[4] A. C. Twitchett-Harrison, T. J. Yates, R. E. Dunin-Borkowski, and P. A. Midgley, Ultramicroscopy **108** 1401 (2008).

LIST OF REFERENCES

A. C. Twitchett-Harrison, T. J. Yates, R. E. Dunin-Borkowski, and P. A. Midgley, Ultramicroscopy **108** 1401 (2008).

A. C. Jones, M. L. Hitchman, and Knovel (Firm), Chemical vapour deposition precursors, processes and applications. Royal Society of Chemistry, Cambridge, UK, (2009).

A. Lubk, D. Wolf, and H. Lichte, Ultramicroscopy **110** 438 (2010).

A. S. Arico, P. Bruce, B. Scrosati, J.-M. Tarascon, and W. Van Schalkwijk, Nature materials **4** 366 (2005).

A. Sekar, S. H. Kim, A. Umar, and Y. B. Hahn, Journal of Crystal Growth **277** 471 (2005).

A. T. Heitsch, D. D. Fanfair, H.-Y. Tuan, and B. A. Korgel, J Am Chem Soc **130** 5436 (2008).

A. Tonomura, Reviews of Modern Physics **59** 639 (1987).

A. Umar and Y. B. Hahn, Nanotechnology **17** 2174 (2006).

A. Umar, S. H. Kim, Y. S. Lee, K. S. Nahm, and Y. B. Hahn, Journal of Crystal Growth **282** 131 (2005).

A. Umar, S. Lee, Y. S. Lee, K. S. Nahm, and Y. B. Hahn, Journal of Crystal Growth **277** 479 (2005).

A. V. Crewe and J. Wall, Journal of Molecular Biology **48** 375 (1970).

B. G. Yacobi, Semiconductor materials : an introduction to basic principles. Kluwer Academic/Plenum Publishers, New York, (2003).

B. Key, R. Bhattacharyya, M. Morcrette, V. Seznéc, J.-M. Tarascon, and C. P. Grey, J Am Chem Soc **131** 9239 (2009).

B. P. Zhang, N. T. Binh, K. Wakatsuki, Y. Segawa, Y. Yamada, N. Usami, M. Kawasaki, and H. Koinuma, Applied Physics Letters **84** 4098 (2004).

B. Pal and M. Sharon, Mater Chem Phys **76** 82 (2002).

C. C. Ahn, Transmission electron energy loss spectrometry in materials science and the EELS atlas, 2nd ed. Wiley, Weinheim, Germany, (2004).

C. Fuller and J. Severiens, Physical Review **96** 21 (1954).

C. J. Lee, T. J. Lee, S. C. Lyu, Y. Zhang, H. Ruh, and H. J. Lee, Applied Physics Letters **81** 3648 (2002).

C. K. Chan, H. Peng, G. Liu, K. McIlwrath, X. F. Zhang, R. A. Huggins, and Y. Cui, Nat Nano **3** 31 (2008).

C. Y. Wen, M. C. Reuter, J. Bruley, J. Tersoff, S. Kodambaka, E. A. Stach, and F. M. Ross, Science **326** 1247 (2009).

D. A. Neamen, Semiconductor physics and devices : basic principles, 2nd ed. Irwin, Chicago, (1997).

D. A. Neamen, Semiconductor physics and devices : basic principles, 3rd ed. McGraw-Hill Higher Education, London, (2003).

D. B. Williams and C. B. Carter, Transmission electron microscopy : a textbook for materials science, 2nd ed. Springer, New York, (2009).

D. C. Ghiglia and M. D. Pritt, Two-dimensional phase unwrapping : theory, algorithms, and software. Wiley, New York, (1998).

D. Cooper, C. Ailliot, J.-P. Barnes, J.-M. Hartmann, P. Salles, G. Benassayag, and R. E. Dunin-Borkowski, Ultramicroscopy **110** 383 (2010).

D. E. Perea, E. R. Hemesath, E. J. Schwalbach, J. L. Lensch-Falk, P. W. Voorhees, and L. J. Lauhon, Nature nanotechnology **4** 315 (2009).

D. E. Perea, E. Wijaya, J. L. Lensch-Falk, E. R. Hemesath, and L. J. Lauhon, Journal of Solid State Chemistry **181** 1642 (2008).

D. E. Perea, N. Li, R. M. Dickerson, A. Misra, and S. T. Picraux, Nano letters **11** 3117 (2011).

D. Gabor, Proceedings of the Royal Society of London. Series A. Mathematical and Physical Sciences **197** 454 (1949).

D. Larcher, S. Beattie, M. Morcrette, K. Edstrom, J.-C. Jumas, and J.-M. Tarascon, Journal of Materials Chemistry **17** 3759 (2007).

E. Koren, N. Berkovitch, O. Azriel, A. Boag, Y. Rosenwaks, E. R. Hemesath, and L. J. Lauhon, Applied Physics Letters **99** 223511 (2011).

E. Müller, P. Kruse, D. Gerthsen, M. Schowalter, A. Rosenauer, D. Lamoen, R. Kling, and A. Waag, Applied Physics Letters **86** 154108 (2005).

E. N. Leith and J. Upatnieks, J. Opt. Soc. Am. **52** 1123 (1962).

F. A. Trumbore, Bell System Technical Journal **39** 205 (1960).

F. M. Ross and W. M. Stobbs, Philosophical Magazine A **63** 37 (1991).

F. Qian, Y. Li, S. Gradecak, D. L. Wang, C. J. Barrelet, and C. M. Lieber, Nano letters **4** 1975 (2004).

G. E. Moore, Proceedings of the IEEE **86** 82 (1998).

G. Mandel, Physical Review **134** A1073 (1964).

G. Möllenstedt and H. Wahl, Naturwissenschaften **55** 340 (1968).

G. Radi, Acta Crystallographica Section A **26** 41 (1970).

G. Sberveglieri, S. Groppelli, P. Nelli, A. Tintinelli, and G. Giunta, Sensors and Actuators B: Chemical **25** 588 (1995).

G.-C. Yi, Semiconductor Nanostructures for Optoelectronic Devices Processing, Characterization and Applications, Springer, Heidelberg, (2012).

H. Bethe, Ann. Phys. **87** 55 (1928).

H. Kai, C. Jeong-Hyun, J. Yeonwoong, S. T. Picraux, and C. John, Nanotechnology **24** 115703 (2013).

H. Lichte, P. Formanek, A. Lenk, M. Linck, C. Matzeck, M. Lehmann, and P. Simon, Annual Review of Materials Research **37** 539 (2007).

H. Wu and Y. Cui, Nano Today **7** 414 (2012).

I. Kimukin, M. S. Islam, and R. S. Williams, Nanotechnology **17** S240 (2006).

I. W. Tao, M. Jurkovic, and W. I. Wang, Applied Physics Letters **64** 1848 (1994).

International Technology Roadmap for Semiconductors 2013, available online at http://www.itrs.net.

J. C. H. Spence and J. M. Zuo, Electron microdiffraction. Plenum Press, New York, (1992).

J. E. Allen, E. R. Hemesath, D. E. Perea, J. L. Lensch-Falk, Z. Y. Li, F. Yin, M. H. Gass, P. Wang, A. L. Bleloch, R. E. Palmer, and L. J. Lauhon, Nature nanotechnology **3** 168 (2008).

J. Frank, Electron tomography : three-dimensional imaging with the transmission electron microscope. Plenum Press, New York, (1992).

J. Goldberger, A. I. Hochbaum, R. Fan, and P. Yang, Nano letters **6** 973 (2006).

J. Graetz, C. C. Ahn, R. Yazami, and B. Fultz, Journal of The Electrochemical Society **151** A698 (2004).

J. Ibers, Acta Crystallographica **11** 178 (1958).

J. J. Lee, Y. B. Kim, and Y. S. Yoon, Applied Surface Science **244** 365 (2005).

J. Li, M. R. McCartney, and D. J. Smith, Ultramicroscopy **94** 149 (2003).

J. Li, M. R. McCartney, R. E. Dunin-Borkowski, and D. J. Smith, Acta Crystallographica Section A **55** 652 (1999).

J. M. Cowley, Ultramicroscopy **41** 335 (1992).

J. Q. Hu, Y. Bando, J. H. Zhan, Y. B. Li, and T. Sekiguchi, Applied Physics Letters **83** 4414 (2003).

J. Spence, Acta Crystallographica Section A **49** 231 (1993).

J. W. Dailey, J. Taraci, T. Clement, D. J. Smith, J. Drucker, and S. T. Picraux, J Appl Phys **96** 7556 (2004).

J. Xiang, W. Lu, Y. Hu, Y. Wu, H. Yan, and C. M. Lieber, Nature **441** 489 (2006).

J. Y. Tsao, Materials fundamentals of molecular beam epitaxy. Academic Press, Boston, (1993).

J.-J. Wu, S.-C. Liu, C.-T. Wu, K.-H. Chen, and L.-C. Chen, Applied Physics Letters **81** 1312 (2002).

K. B. Wolfstirn, Journal of Physics and Chemistry of Solids **16** 279 (1960).

K. Sato, M. Hanafusa, A. Noda, A. Arakawa, M. Uchida, T. Asahi, and O. Oda, Journal of Crystal Growth **214–215** 1080 (2000).

L. Baggetto and P. H. L. Notten, Journal of The Electrochemical Society **156** A169 (2009).

L. Chen, W. Y. Fung, and W. Lu, Nano letters **13** 5521 (2013).

L. J. Lauhon, M. S. Gudiksen, C. L. Wang, and C. M. Lieber, Nature **420** 57 (2002).

L. Ji, Z. Lin, M. Alcoutlabi, and X. Zhang, Energy & Environmental Science **4** 2682 (2011).

L. Li, D. J. Smith, E. Dailey, P. Madras, J. Drucker, and M. R. McCartney, Nano letters **11** 493 (2011).

L. Li, Z. Gan, M. R. McCartney, H. Liang, H. Yu, W. J. Yin, Y. Yan, Y. Gao, J. Wang, and D. J. Smith, Adv Mater **26** 1052 (2014).

L. Reimer, Transmission electron microscopy : physics of image formation and microanalysis, 4th ed. Springer, New York, (1997).

L. Y. Beaulieu, K. W. Eberman, R. L. Turner, L. J. Krause, and J. R. Dahn, Electrochemical and Solid-State Letters **4** A137 (2001).

MultiPrepTM operating manual of Allied High Tech Products, Inc.

M. A. Herman and H. Sitter, Molecular beam epitaxy : fundamentals and current status, 2nd, rev. and updated ed. Springer, New York, (1996).

M. Armand and J. M. Tarascon, Nature **451** 652 (2008).

M. Faraday, Experimental researches in electricity. R. and J.E. Taylor, London, (1839).

M. Gajdardziska-Josifovska and A. H. Carim, Chapter 12, Introduction to electron holography, Kluwer Academic/Plenum Publishers, New York, (1999).

M. Gajdardziska-Josifovska, M. R. McCartney, W. J. de Ruijter, D. J. Smith, J. K. Weiss, and J. M. Zuo, Ultramicroscopy **50** 285 (1993).

M. Gu, H. Yang, D. E. Perea, J. G. Zhang, S. Zhang, and C. M. Wang, Nano letters **14** 4622 (2014).

M. H. Huang, S. Mao, H. Feick, H. Yan, Y. Wu, H. Kind, E. Weber, R. Russo, and P. Yang, Science **292** 1897 (2001).

M. I. den Hertog, H. Schmid, D. Cooper, J. L. Rouviere, M. T. Bjork, H. Riel, P. Rivallin, S. Karg, and W. Riess, Nano letters **9** 3837 (2009).

M. J. Hytch, E. Snoeck, and R. Kilaas, Ultramicroscopy **74** 131 (1998).

M. Lehmann and H. Lichte, Microscopy and Microanalysis **8** 447 (2004).

M. Lehmann, Ultramicroscopy **100** 9 (2004).

M. N. Obrovac and L. Christensen, Electrochemical and Solid-State Letters **7** A93 (2004).

M. N. Obrovac and L. J. Krause, Journal of The Electrochemical Society **154** A103 (2007).

M. R. McCartney and D. J. Smith, Annual Review of Materials Research **37** 729 (2007).

M. R. McCartney and M. Gajdardziska-Josifovska, Ultramicroscopy **53** 283 (1994).

M. R. McCartney, N. Agarwal, S. Chung, D. A. Cullen, M.-G. Han, K. He, L. Li, H. Wang, L. Zhou, and D. J. Smith, Ultramicroscopy **110** 375 (2010).

M. S. Gudiksen, L. J. Lauhon, J. Wang, D. C. Smith, and C. M. Lieber, Nature **415** 617 (2002).

M. Schowalter, D. Lamoen, A. Rosenauer, P. Kruse, and D. Gerthsen, Applied Physics Letters **85** 4938 (2004).

M. Y. Kim, J. M. Zuo, and J. C. H. Spence, physica status solidi (a) **166** 445 (1998).

M.-S. Kim and Y.-M. Sung, Chem Mater **25** 4156 (2013).

N. Li, T. Y. Tan, and U. Gösele, Applied Physics A **90** 591 (2008).

N. Ohashi, K. Kataoka, T. Ohgaki, T. Miyagi, H. Haneda, and K. Morinaga, Applied Physics Letters **83** 4857 (2003).

N. Sclar, Electron Devices, IEEE Transactions on **24** 709 (1977).

O. Hayden, A. B. Greytak, and D. C. Bell, Advanced Materials **17** 701 (2005).

O. Hiroshi, I. Gheyas Syed, N. Hitoshi, N. Mitsuhiro, and Y. Akira, Japanese Journal of Applied Physics **33** L980 (1994).

P. A. Doyle and P. S. Turner, Acta Crystallographica Section A **24** 390 (1968).

P. A. Tipler, Modern physics. Worth Publishers, New York, (1978).

P. Becker and P. Coppens, Acta Crystallographica Section A **46** 254 (1990).

P. G. Bruce, B. Scrosati, and J.-M. Tarascon, Angewandte Chemie International Edition **47** 2930 (2008).

P. Hartel, H. Rose, and C. Dinges, Ultramicroscopy **63** 93 (1996).

P. M. Voyles, D. A. Muller, J. L. Grazul, P. H. Citrin, and H. J. Gossmann, Nature **416** 826 (2002).

R. Agarwal, Small **4** 1872 (2008).

R. F. Egerton, Electron energy-loss spectroscopy in the electron microscope, 2nd ed. Plenum Press, New York, (1996).

R. S. Wagner and W. C. Ellis, Applied Physics Letters **4** 89 (1964).

S. A. Dayeh, J. Wang, N. Li, J. Y. Huang, A. V. Gin, and S. T. Picraux, Nano letters **11** 4200 (2011).

S. A. Dayeh, N. H. Mack, J. Y. Huang, and S. T. Picraux, Applied Physics Letters **99** 023102 (2011).

S. Baosheng, Y. Akira, and K. Makoto, Japanese Journal of Applied Physics **37** L206 (1998).

S. Dimitrijev, Understanding semiconductor devices. Oxford University Press, New York, (2000).

S. Ingole, P. Manandhar, S. B. Chikkannanavar, E. A. Akhadov, and S. T. Picraux, Electron Devices, IEEE Transactions on **55** 2931 (2008).

S. J. Pennycook, P. D. Nellist, Scanning Transmission Electron Microscopy Imaging and Analysis. Springer, New York, NY, (2011).

S. M. Sze, Physics of semiconductor devices, 2nd ed. Wiley, New York, (1981).

S. M. Sze, Physics of semiconductor devices. Wiley-Interscience, New York, (1969).

S. M. Sze, Semiconductor devices, physics and technology, 2nd ed. Wiley, New York, (2002).

S. Miyake, Proc. Phys. Math. Soc. Japan **22** 666 (1940).

T. E. Clark, P. Nimmatoori, K.-K. Lew, L. Pan, J. M. Redwing, and E. C. Dickey, Nano letters **8** 1246 (2008).

T. Hoshikawa, X. Huang, K. Hoshikawa, and S. Uda, Japanese Journal of Applied Physics **47** 8691 (2008).

T. Tanaka, K. Hayashida, K. Saito, M. Nishio, Q. Guo, and H. Ogawa, physica status solidi (b) **243** 959 (2006).

T. Tanaka, N. Murata, K. Saito, M. Nishio, Q. Guo, and H. Ogawa, physica status solidi (b) **244** 1685 (2007).

T. Tanaka, Q. Guo, M. Nishio, and H. Ogawa, Journal of Physics: Conference Series **61** 1162 (2007).

T. Teiji, M. Toyosaka, and T. Kiyoshi, Japanese Journal of Applied Physics **11** 1024 (1972).

U. K. Mishra, J. Singh, Semiconductor device physics and design. Springer, Dordrecht, The Netherlands, (2008).

U. Özgür, Y. I. Alivov, C. Liu, A. Teke, M. A. Reshchikov, S. Doğan, V. Avrutin, S. J. Cho, and H. Morkoç, Journal of Applied Physics **98** 041301 (2005).

V. Schmidt, H. Riel, S. Senz, S. Karg, W. Riess, and U. Gosele, Small **2** 85 (2006).

V. Schmidt, J. V. Wittemann, S. Senz, and U. Gösele, Advanced Materials **21** 2681 (2009).

W. D. Callister, T. L. Larsen, C. F. Varotto, and D. A. Stevenson, Journal of Physics and Chemistry of Solids **33** 1433 (1972).

W. Lu, J. Xiang, B. P. Timko, Y. Wu, and C. M. Lieber, Proc. Nat. Acad. Sci. **102** 10046 (2005).

W. Lu, P. Xie, and C. M. Lieber, IEEE Transactions on Electron Devices **55** 2859 (2008).

X. H. Liu and J. Y. Huang, Energy & Environmental Science **4** 3844 (2011).

X. H. Liu, H. Zheng, L. Zhong, S. Huang, K. Karki, L. Q. Zhang, Y. Liu, A. Kushima, W. T. Liang, J. W. Wang, J. H. Cho, E. Epstein, S. A. Dayeh, S. T. Picraux, T. Zhu, J. Li, J. P. Sullivan, J. Cumings, C. Wang, S. X. Mao, Z. Z. Ye, S. Zhang, and J. Y. Huang, Nano letters **11** 3312 (2011).

X. H. Liu, J. W. Wang, S. Huang, F. Fan, X. Huang, Y. Liu, S. Krylyuk, J. Yoo, S. A. Dayeh, A. V. Davydov, S. X. Mao, S. T. Picraux, S. Zhang, J. Li, T. Zhu, and J. Y. Huang, Nature nanotechnology **7** 749 (2012).

X. H. Liu, L. Q. Zhang, L. Zhong, Y. Liu, H. Zheng, J. W. Wang, J. H. Cho, S. A. Dayeh, S. T. Picraux, J. P. Sullivan, S. X. Mao, Z. Z. Ye, and J. Y. Huang, Nano letters **11** 2251 (2011).

X. H. Liu, S. Huang, S. T. Picraux, J. Li, T. Zhu, and J. Y. Huang, Nano letters **11** 3991 (2011).

X. H. Liu, Y. Liu, A. Kushima, S. Zhang, T. Zhu, J. Li, and J. Y. Huang, Advanced Energy Materials **2** 722 (2012).

X. Y. Kong, Y. Ding, R. Yang, and Z. L. Wang, Science **303** 1348 (2004).

Y. C. Kong, D. P. Yu, B. Zhang, W. Fang, and S. Q. Feng, Applied Physics Letters **78** 407 (2001).

Y. Cui, Q. Wei, H. Park, and C. M. Lieber, Science **293** 1289 (2001).

Y. Hu, H. O. Churchill, D. J. Reilly, J. Xiang, C. M. Lieber, and C. M. Marcus, Nature nanotechnology **2** 622 (2007).

Y. Li, G. W. Meng, L. D. Zhang, and F. Phillipp, Applied Physics Letters **76** 2011 (2000).

Y. Liu, S. Zhang, and T. Zhu, ChemElectroChem **1** 706 (2014).

Y. Liu, X. H. Liu, B. M. Nguyen, J. Yoo, J. P. Sullivan, S. T. Picraux, J. Y. Huang, and S. A. Dayeh, Nano letters **13** 4876 (2013).

Y. Wu, Y. Cui, L. Huynh, C. J. Barrelet, D. C. Bell, and C. M. Lieber, Nano letters **4** 433 (2004).

Y.-C. Chou, C.-Y. Wen, M. C. Reuter, D. Su, E. A. Stach, and F. M. Ross, ACS Nano **6** 6407 (2012).

Y.-M. Chiang, Science **330** 1485 (2010).

Z. Gan, D. E. Perea, J. Yoo, S. Tom Picraux, D. J. Smith, and M. R. McCartney, Applied Physics Letters **103** 153108 (2013).

Z. Gan, D. Perea, J. Yoo, Y. He, R. Colby, B. Barker, M. Gu, S. Mao, C. Wang, S. Tom Picraux, D. Smith, and M. McCartney, Unpublished (2015).

Z. L. Wang, Journal of Physics: Condensed Matter **16** R829 (2004).

Z. W. Pan, Z. R. Dai, and Z. L. Wang, Science **291** 1947 (2001).